
ERNEST ORLANDO LAWRENCE
BERKELEY NATIONAL LABORATORY

# Three-Dimensional Numerical Modeling of the Influence of Faults on Groundwater Flow at Yucca Mountain, Nevada

Andrew J. B. Cohen
Ph.D. Thesis

**Earth Sciences Division**

June 1999

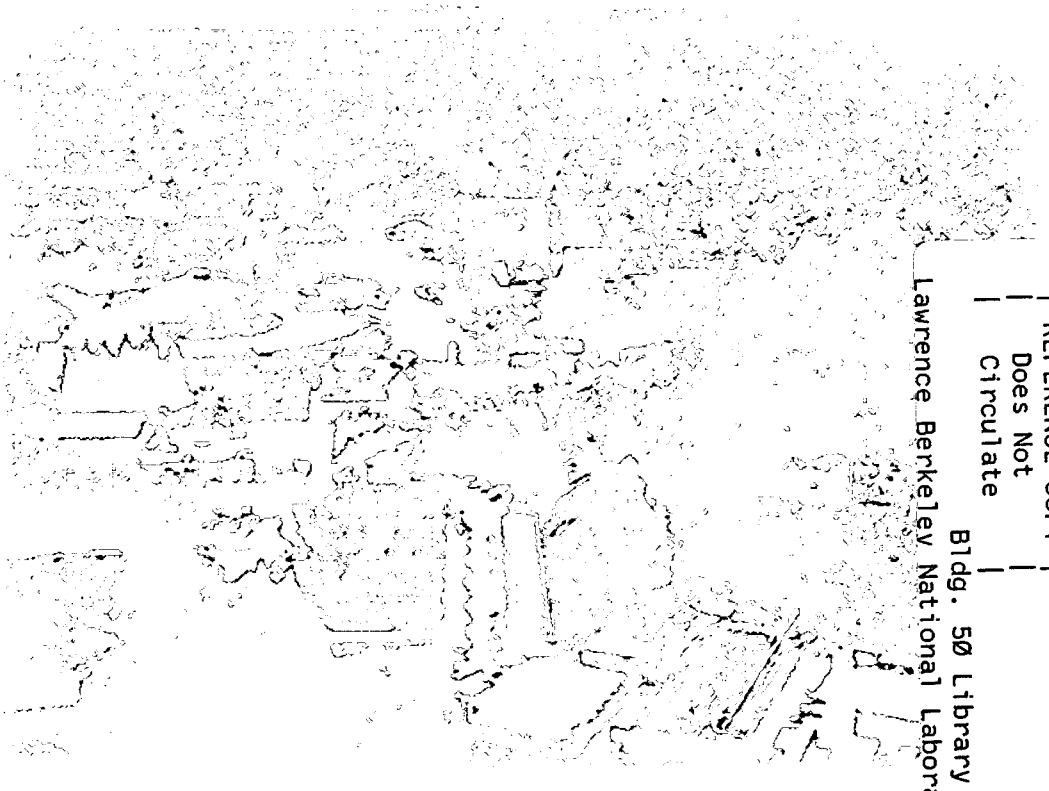

## DISCLAIMER

LBNL-43377

# Three-Dimensional Numerical Modeling of the Influence of Faults on Groundwater Flow at Yucca Mountain, Nevada

Andrew J. B. Cohen
Ph.D. Thesis

Department of Civil and Environmental Engineering
University of California, Berkeley

and

Earth Sciences Division
Ernest Orlando Lawrence Berkeley National Laboratory
Berkeley, CA

June 1999

This work was supported in part by the Director, Office of Civilian Radioactive Waste Management, U.S. Department of Energy under Contract No. DE-AC03-76SF00098.

# Three-Dimensional Numerical Modeling of the Influence of Faults on Groundwater Flow at Yucca Mountain, Nevada

by

Andrew Jay Buckminster Cohen

B.S. (State University of New York at Oneonta) 1991
M.S. (University of California, Berkeley) 1993

A dissertation submitted in partial satisfaction of the

requirements for the degree of

Doctor of Philosophy
in

Engineering-Civil and Environmental Engineering

in the

GRADUATE DIVISION

of the

UNIVERSITY OF CALIFORNIA, BERKELEY

Committee in charge:

Professor Nicholas Sitar, Chair
Professor Yoram N. Rubin
Professor Kent S. Udell

Spring 1999

Three-Dimensional Numerical Modeling of the Influence of Faults on Groundwater Flow at Yucca Mountain, Nevada



by

Andrew Jay Buckminster Cohen

Abstract

Three-Dimensional Numerical Modeling of the Influence of Faults on Groundwater Flow at Yucca Mountain, Nevada

by

Andrew Jay Buckminster Cohen

Doctor of Philosophy in Engineering-Civil and Environmental Engineering

University of California, Berkeley

Professor Nicholas Sitar, Chair

Numerical simulations of groundwater flow at Yucca Mountain, Nevada are used to investigate how the faulted hydrogeologic structure influences groundwater flow from a proposed high-level nuclear waste repository. Simulations are performed using a 3-D model that has a unique grid block discretization to accurately represent the faulted geologic units, which have variable thicknesses and orientations. Irregular grid blocks enable explicit representation of these features. Each hydrogeologic layer is discretized into a single layer of irregular and dipping grid blocks, and faults are discretized such that they are laterally continuous and displacement varies along strike. In addition, the presence of altered fault zones is explicitly modeled, as appropriate. The model has 23 layers and 11 faults, and approximately 57,000 grid blocks and 200,000 grid block connections. In the past, field measurement of upward vertical head gradients and high water table temperatures near faults were interpreted as indicators of upwelling from a deep carbonate aquifer. Simulations show, however, that these features can be readily

explained by the geometry of hydrogeologic layers, the variability of layer permeabilities and thermal conductivities, and by the presence of permeable fault zones or faults with displacement only. In addition, a moderate water table gradient can result from fault displacement or a laterally continuous low permeability fault zone, but not from a high permeability fault zone, as others postulated earlier. Large-scale macrodispersion results from the vertical and lateral diversion of flow near the contact of high and low permeability layers at faults, and from upward flow within high permeability fault zones. Conversely, large-scale channeling can occur due to groundwater flow into areas with minimal fault displacement. Contaminants originating at the water table can flow in a direction significantly different than that of the water table gradient, and isolated zones of contaminants will occur at the water table downgradient. This behavior is not predicted by traditional models of contaminant transport. In addition, the influence of a particular type of fault cannot be generalized; depending on the location where contaminants enter the saturated zone, faults may either enhance or inhibit vertical dispersion.

# TABLE OF CONTENTS


List of Figures vi
List of Tables x
Acknowledgments xi

**1. Introduction 1**
1.1 Background 1
1.2 Previous Work 2
1.3 Objectives 5

**2. Geology and Hydrology at Yucca Mountain 7**
2.1 Stratigraphy 7
2.2 Structure and Faulting 10
2.3 Hydraulic Gradients 12
2.3.1 Water Table 12
2.3.2 Large Hydraulic Gradient Zone 15
2.3.3 Moderate Hydraulic Gradient Zone 16
2.3.4 Small Hydraulic Gradient Zone 16
2.3.5 Vertical Hydraulic Gradients 17
2.4 Perched Water 18
2.5 Hydrogeologic Properties 20
2.6 Hydrochemistry 23
2.7 Geothermal Gradient 24
2.8 Conceptual Model of Groundwater Flow 26

**3. Modeling Approach 29**
3.1 Flow Simulator 29
3.1.1 Governing Equations 29
3.1.2 Discretization of the Governing Equation 31
3.2 Steady-State and Confined Flow 33
3.3 Transport Modeling for Flow Visualization 34

**4. Model Discretization 35**
4.1 General 35
4.2 Geologic Model 35
4.3 Dimensions and Boundaries 36
4.4 2-D Discretization 38
4.5 Definition of Hydrogeologic Layers 42
4.5.1 Lithic Ridge Tuff 45
4.5.2 Lava Flows and Breccias 46
4.5.3 Lower Volcanic Confining Unit 47
4.5.4 Crater Flat Group 48
4.5.4.1 Pre-Tram Bedded Tuff 49
4.5.4.2 Tram Tuff 49
4.5.4.3 Bullfrog Tuff 50

4.5.4.4 Prow Pass Tuff 51
4.5.5 Calico Hills Formation 51
4.5.6 Topopah Spring Tuff 52
4.6 Vertical Concatenation of Individual Layers 56
4.7 Selection and Representation of Faults 56
4.7.1 Fault Discretization 57
4.8 Comparison to Geologic Model 60

**5. Hydrogeologic and Thermal Properties 64**
5.1 Permeability 64
5.1.1 Upper Volcanic Aquifer 64
5.1.2 Upper Volcanic Confining Unit 65
5.1.3 Lower Volcanic Aquifer 65
5.1.4 Lower Volcanic Confining Unit 67
5.2 Porosity 67
5.3 Thermal Conductivity 67

**6. 2-D Simulations 69**
6.1 Introduction 69
6.2 2-D Model 69
6.3 Simulation Approach 70
6.3.1 General 70
6.3.2 Flow Visualization Tracer 70
6.4 Boundary Conditions 72
6.4.1 Hydraulic Head 72
6.4.2 Flux 72
6.5 Case 1: Displacement-Only Faults 74
6.5.1 Base Case 74
6.5.2 Effects of Unsaturated Zone Flow Pathway 79
6.5.3 Effects of Increased Percolation 80
6.6 Case 2: High Permeability Faults 81
6.6.1 Base Case 81
6.6.2 Effects of Unsaturated Zone Flow Pathway 85
6.7 Case 3: Low Permeability Faults 87
6.7.1 Base Case 87
6.8 Heat Flow 89
6.8.1 Boundary Conditions 89
6.8.2 Heat Conduction 90
6.8.3 Analysis of Temperature Data 91

**7. 3-D Simulations 93**
7.1 Introduction 93
7.2 3-D Sub-Model 93
7.3 Simulation Approach 94
7.4 Boundary Conditions 95
7.4.1 Hydraulic Head 95

7.4.2 Flux 95
7.5 Case 1: Displacement-Only Faults 95
7.6 Case 2: High Permeability Faults 104
7.7 Case 3: Low Permeability Faults 109
7.8 Sensitivity Analysis 110
7.8.1 Sensitivity to Model Boundaries 110
7.8.2 Sensitivity to Fault Permeability 112
7.9 Alternative Models 114
7.9.1 Hybrid 1 115
7.9.2 Hybrid 2 119

**8. Discussion and Recommendations 124**
8.1 Purpose and Development of the 3-D Saturated Zone Flow Model 124
8.2 Summary of Findings 126
8.3 Future Work 130
8.3.1 Stochastic Modeling 130
8.3.2 Calibration to Pumping Test Data 130
8.3.3 Particle Tracking 133

**REFERENCES 134**

**APPENDIX A: 2-D Particle Tracking for Irregular Meshes 141**

## LIST OF FIGURES


| | | |
|---|---|---|
| Figure 2.1 | Faults at Yucca Mountain, as defined by the ISM2.0 3-D Geologic Framework and Integrated Site Model of Yucca Mountain (Clayton *et al.*, 1997). The Exploratory Studies Facility (ESF) is a testing tunnel in the unsaturated zone. Coordinates are Nevada State Plane coordinates. Figure courtesy of Jennifer Hinds, Lawrence Berkeley National Laboratory. | 11 |
| Figure 2.2 | Water table surface at Yucca Mountain (modified from Tucci and Burkhardt, 1995). | 13 |
| Figure 2.3 | Boreholes in which perched water was observed. Figure courtesy of Jennifer Hinds, Lawrence Berkeley National Laboratory. | 20 |
| Figure 2.4 | Temperature distribution at the water table (from Sass *et al.*, 1995). | 25 |
| Figure 2.5 | Conceptual model of groundwater flow at Yucca Mountain. | 28 |
| Figure 3.1 | Space discretization and grid block specifications in the integral finite difference method (from Pruess *et al.*, 1996). | 31 |
| Figure 4.1 | Water table map used to define the top of the saturated zone model. | 38 |
| Figure 4.2 | Example irregular mesh composed of Voronoi grid blocks and the definitions of grid block connections used in TOUGH2. | 40 |
| Figure 4.3 | 2-D mesh of the saturated zone model. | 41 |
| Figure 4.4 | Isopach of the Lithic Ridge Tuff defined by Carr *et al.* (1986) within the model area. | 46 |
| Figure 4.5 | Isopach of lava flows and breccias. Control points for interpolation are data at H-1, H-6, G-1, G-2, and zero thicknesses assigned at boreholes H-3, H-4, b#1, and WT #6. | 47 |
| Figure 4.6 | Isopach of Lower Volcanic Confining Unit. | 48 |
| Figure 4.7 | Thickness of the Tram Tuff beneath the water table. | 53 |
| Figure 4.8 | Thickness of the Bullfrog Tuff beneath the water table. | 53 |
| Figure 4.9 | Thickness of the Prow Pass Tuff beneath the water table. | 54 |
| Figure 4.10 | Thickness of the Calico Hills Formation beneath the water table. | 54 |
| Figure 4.11 | Thickness of the vitric sub-zones and bedded tuff of the Topopah Spring Tuff beneath the water table. | 55 |

| | | |
|---|---|---|
| Figure 4.12 | Thickness of the densely welded Topopah Spring Tuff beneath the water table. | 55 |
| Figure 4.13 | Fault displacement in the saturated zone model (in meters). Positive values represent down-to-the-west displacement. Negative values represent down-to-the-east displacement. | 58 |
| Figure 4.14 | Vertical discretization of fault grid blocks. Dots are grid block nodes and dashed lines are grid block connections. | 59 |
| Figure 4.15 | Distribution of rock units at the top of the saturated zone model. | 61 |
| Figure 4.16 | Horizontal slice through ISM2.0: A 3D Geologic Framework and Integrated Site Model of Yucca Mountain (Clayton *et al.*, 1997). | 62 |
| Figure 4.17 | a) Cross-section along A-A' in the saturated zone model; b) geologic section along A-A' through ISM2.0: A 3D Geologic Framework and Integrated Site Model of Yucca Mountain (Clayton *et al.*, 1997). | 63 |
| Figure 6.1 | Example flow visualization tracer in a steady-state flow field. Vertical exaggeration = 4x. | 71 |
| Figure 6.2 | Infiltration distribution at Yucca Mountain, Nevada (from Flint *et al.*, 1996 (unpublished)). | 73 |
| Figure 6.3 | Percolation flux boundary and calibrated permeability distribution in the displacement-only faults model. | 74 |
| Figure 6.4 | Calibrated steady-state head distribution in the displacement-only faults model. Vertical exaggeration = 4x. | 76 |
| Figure 6.5 | Flow visualization tracer at 50 years in the displacement-only faults model with percolation to the water table beneath the repository. Vertical exaggeration = 4x. | 78 |
| Figure 6.6 | Flow visualization tracer at 50 years in the displacement-only faults model with tracer source at the Topopah Spring Tuff-water table contact. Vertical exaggeration = 4x. | 79 |
| Figure 6.7 | Flow visualization tracer at 667 years in the displacement-only faults model with tracer source at the Topopah Spring Tuff-water table contact. Vertical exaggeration = 4x. | 80 |
| Figure 6.8 | Calibrated steady-state head distribution in the high permeability faults model. Vertical exaggeration = 4x. | 82 |
| Figure 6.9 | Flow visualization tracer at 50 years in the high permeability faults model with percolation to the water table beneath the repository. Vertical exaggeration = 4x. | 83 |

| | | |
|---|---|---|
| Figure 6.10 | Flow visualization tracer at 50 years in the high permeability faults model with tracer source west of Solitario Canyon Fault. Vertical exaggeration = 4x. | 84 |
| Figure 6.11 | Flow visualization tracer at 50 years in the high permeability faults model with tracer source at the Topopah Spring Tuff-water table contact. Vertical exaggeration = 4x. | 86 |
| Figure 6.12 | Flow visualization tracer at 667 years in the high permeability faults model with tracer source at the Topopah Spring Tuff-water table contact. Vertical exaggeration = 4x. | 86 |
| Figure 6.13 | Steady-state head distribution in a low permeability faults model. Vertical exaggeration = 4x. | 88 |
| Figure 6.14 | Flow visualization tracer at 50 years in a low permeability faults model with percolation below the repository. Vertical exaggeration = 4x. | 88 |
| Figure 6.15 | Steady-state temperature distribution due to heat conduction in the displacement-only faults model. Vertical exaggeration = 4x. | 91 |
| Figure 6.16 | Temperature log for borehole H-5. Arrows mark discrete intervals where flow was produced during a borehole-flow survey. | 92 |
| Figure 7.1 | Boundary grid blocks of the 3-D sub-model. | 94 |
| Figure 7.2 | Steady-state water table in the displacement-only faults model. | 97 |
| Figure 7.3 | Steady-state head distribution in the central layer of the Bullfrog Tuff in the displacement-only faults model. | 98 |
| Figure 7.4 | Flow visualization tracer in the central layer of the Bullfrog Tuff after 50 years in the displacement-only faults model. | 101 |
| Figure 7.5 | Flow visualization tracer in the central layer of the Prow Pass Tuff after 50 years in the displacement-only faults model. | 102 |
| Figure 7.6 | Flow visualization tracer at the water table after 50 years in the displacement-only faults model. | 103 |
| Figure 7.7 | Steady-state water table in the high permeability faults model. | 105 |
| Figure 7.8 | Flow visualization tracer in the central layer of the Bullfrog Tuff after 50 years in the high permeability faults model. | 106 |
| Figure 7.9 | Flow visualization tracer in the central Prow Pass Tuff after 50 years in the high permeability faults model. | 107 |

| | | |
|---|---|---|
| Figure 7.10 | Flow visualization tracer at the water table after 50 years in the high permeability faults model. | 108 |
| Figure 7.11 | Steady-state water table in a low-permeability faults model with $k_{fault} = 10^{-14}$ m$^2$. | 109 |
| Figure 7.12 | Steady-state water table in a homogeneous model. | 111 |
| Figure 7.13 | Steady-state water table in a model with fault permeability $k_{fault} = 10^{-13}$ m$^2$. | 113 |
| Figure 7.14 | Steady-state water table in a model with fault permeability $k_{fault} = 10^{-11}$ m$^2$. | 114 |
| Figure 7.15 | Steady-state water table in the Hybrid 1 model. | 116 |
| Figure 7.16 | Flow visualization tracer in the central Bullfrog Tuff after 50 years in the Hybrid 1 model . | 117 |
| Figure 7.17 | Flow visualization tracer in the central Prow Pass Tuff after 50 years in the Hybrid 1 model. | 118 |
| Figure 7.18 | Flow visualization tracer at the water table after 50 years in the Hybrid 1 model. | 119 |
| Figure 7.19 | Steady-state water table in the Hybrid 2 model. | 120 |
| Figure 7.20 | Flow visualization tracer in the central Bullfrog Tuff after 50 years in the Hybrid 2 model. | 121 |
| Figure 7.21 | Flow visualization tracer in the central Prow Pass Tuff after 50 years in the Hybrid 2 model. | 122 |
| Figure 7.22 | Flow visualization tracer at the water table after 50 years in the Hybrid 2 model. | 123 |
| Figure 8.1 | Dimensionless drawdown for $k_f/k_b = 0.01$. | 132 |
| Figure 8.2 | Dimensionless drawdown for $k_f/k_b = 10$. | 132 |
| Figure 8.3 | Dimensionless drawdown vs. time for $k_f/k_b = 0.01$. | 132 |
| Figure 8.4 | Dimensionless drawdown vs. time for $k_f/k_b = 10$. | 132 |

# LIST OF TABLES


| | | |
|---|---|---|
| Table 2.1 | Stratigraphic and hydrogeologic units at and around Yucca Mountain (Luckey *et al.*, 1996). | 7 |
| Table 2.2 | Water levels and hydraulic heads in saturated zone boreholes at Yucca Mountain. Hydraulic head was measured in packed-off intervals in some boreholes. | 14 |
| Table 2.3 | Estimated permeability of hydrogeologic units. | 21 |
| Table 4.1 | Sources of borehole geophysical and hydrologic data used to discretize geologic units and assign hydrogeologic properties. | 43 |
| Table 5.1 | Ranges of hydrogeologic properties used in simulations. | 68 |
| Table 6.1 | Calibrated permeabilities for saturated zone model layers. | 75 |
| Table 7.1 | Calibration statistics for different 3-D sub-models. Asterisk indicates borehole is located at a boundary node. | 112 |

## ACKNOWLEDGMENTS

I must first thank those scientists in the Earth Sciences Division at Lawrence Berkeley National Laboratory who provided me the opportunity to pursue this degree. In addition, I appreciate the guidance of Professor Nick Sitar, my thesis advisor, who also responded to my ideas enthusiastically.

I am grateful to Kenzi Karasaki for encouraging me to pursue my doctorate. It was the work on his project that fueled my desire to further my education. Sally Benson also encouraged me and was essential in providing support. Bo Bodvarsson, Iraj Javandel, and Chin-Fu Tsang were very generous in providing the help I needed to complete this work. In addition, the guidance I received from Chin-Fu enabled me to push on through the final version of this dissertation.

The contributions from Charles Haukwa and Mark Feighner were essential to the development of the numerical model. Charles was generous in teaching me many of the steps required to discretize the model mesh, and only by working with Mark was I able to obtain the data necessary to define the geologic structure represented in the model. Thanks also to Curt Oldenburg; because of him I now have a greater understanding of and appreciation for numerical methods.

Mary Cook of the Department of Civil and Environmental Engineering made the long trail of required paperwork easy to walk, and she met my repeated questions with smiles.

Finally, I am most grateful to my wife, Lara, for supporting this endeavor. Thank you so much.

This work was supported in part by the Director, Office of Civilian Radioactive Waste Management, U.S. Department of Energy, through Memorandum Purchase Order EA9013MC5X between TRW Environmental Safety Systems Incorporated and Ernest Orlando Lawrence Berkeley National Laboratory, under Contract No. DE-AC03-76SF00098.

# 1. Introduction

## 1.1 Background

Yucca Mountain, Nevada, is the proposed site for a high-level nuclear waste repository for the United States. It is located in the Nevada Test Site, approximately 150 miles northwest of Las Vegas, Nevada. In 1987 the U.S. Congress designated Yucca Mountain as the sole site to be studied as a potential repository, in part because it is remote, and because the hydrologic and hydrogeologic features are expected to provide a natural barrier to potential radionuclide release (U.S. Department of Energy, 1988). The repository would be built in volcanic rocks 300-400 m below the surface and 200-400 m above the water table. The waste canisters would be placed in emplacement drifts, which would create capillary barriers to infiltrating water, and the waste form will be designed to inhibit dissolution. These engineered barriers are the primary barrier to potential radionuclide percolation to the water table. The primary natural barrier is the unsaturated zone. Due to the semi-arid climate, precipitation and infiltration are relatively low, which minimizes the potential fluid flow into and out of the proposed repository. The thick unsaturated zone beneath the repository would further minimize seepage to the water table because of sorption to zeolitized tuffs (Fridrich *et al.*, 1991). The underlying saturated zone is considered the secondary natural barrier because the concentrations of radionuclides are expected to be diluted in the groundwater (U.S. Department of Energy, 1988).

Yucca Mountain is underlain by a sequence of faulted and dipping stratigraphic units that have variable thicknesses and orientations. Since the early studies of the saturated zone

around Yucca Mountain in the 1970's, workers have hypothesized that the faults are important hydrogeologic features that may create flow barriers or conduits for groundwater flow. Few measurements of the hydraulic properties of faults have been made since the early studies, and most numerical models of groundwater flow and radionuclide transport have not considered faults downgradient from the repository. Hypotheses regarding the effects of faults on flow and transport have remained untested, and the properties of some faults in calibrated saturated zone flow models conflicts with field observations. For example, temperature anomalies at the water table, isotopic data, and the presence of vertical gradients seem to suggest that water upwells through a fault from a deep Carbonate Aquifer, but all existing hydrogeologic models require assignment of a low permeability to the fault in order to calibrate the model to the water table. The presence of such upwelling is important in that it could significantly affect the dispersion of potential contaminants. In addition, fault displacement creates discontinuities in hydrogeologic layers, which can also affect the travel path and dispersion of potential contaminants. Thus, in order to accurately model contaminant transport from the repository, it is important to develop a better understanding of the role of faults in controlling the saturated zone flow regime. Indeed, the evaluation of hydraulic properties of faults was rated the most important issue concerning saturated zone flow at Yucca Mountain (TRW Environmental Safety Systems Incorporated, 1998).

## 1.2 Previous Work

Numerous numerical models of the saturated zone at and around Yucca Mountain have been developed since site characterization began in the 1970's. Luckey *et al.* (1996) give

a bibliography of 17 numerical models that were developed as of 1995. Most of the models are regional scale models which are not discretized to account for faults.

Sub-site-scale models of Yucca Mountain simulate flow and/or transport near the repository, typically encompassing features immediately north and west of the site, and extending approximately 5 km downgradient from the Mountain. Most of the models do not represent faults explicitly. All models are too shallow to consider upwelling, do not examine vertical head gradients, and all require the presence of two low permeability faults where relatively large lateral head gradients are located. This implies that these faults are dominant features controlling flow.

Barr and others (Chapter 11 of Wilson *et al.*, 1994) present a 3-D saturated zone model which extends approximately 200 m below the water table. Fault zones north and west of the mountain are assigned low permeabilities in order to account for the relatively large hydraulic gradients there, but faults are not modeled explicitly, as there are no lithologic changes across them. Zyvoloski *et al.* (1997) performed transport simulations using a 3-D saturated zone model which extends 250 m below the water table. It is unclear if their mesh incorporates fault offset, as no mention is made regarding discretization of faults. They needed to assign low permeabilities to regions around faults north and west of the mountain in order to calibrate the model to the water table. Arnold and McKenna (1998) developed a 3-D saturated zone model which extends 380 m below the water table. The model accounts for fault displacement and is used for prediction of groundwater transport from the repository. Faults north and west of the repository were

again modeled as low permeability zones in order to calibrate the model to the water table. They considered the effects of intra-unit permeability heterogeneity on transport, but high or low permeability fault zones were not considered. Instead, vertically continuous zones of high permeability were positioned randomly throughout the domain in order to consider the existence of undetected structural zones.

Faunt (1997) integrated structural geologic data, crustal stress data, and fault-trace mapping to infer the effects of faults on regional ground water flow in a 100,000 $km^2$ region extending from Death Valley, California, northward beyond Yucca Mountain. She showed, for example, that springs occur where large rock blocks are displaced against lower permeability rocks, suggesting that faults are flow barriers or that the fault zones have significant permeability. Finally, a 3-D numerical model of the unsaturated zone at Yucca Mountain shows that faults can channel surface water vertically to the water table (Bodvarsson *et al.*, 1997).

Most of the literature describing fault effects on groundwater flow in general is presented in the context of geothermal heating and the convection that occurs within faults of relatively high permeability. Forster and Smith (1989) examined how faults influence groundwater flow and heat transfer, and how they control the temperatures of springs on a regional scale. They used a 2-D numerical model, wherein the fault was represented as a one-dimensional feature. López and Smith (1995, 1996) used a 3-D model of a dipping fault to examine the interaction of thermally driven groundwater in the fault and the surrounding country rock. None of these models considered a heterogeneous

permeability in the country rock, whereas this heterogeneity is present at Yucca Mountain.

Overall, field observations and numerical models of groundwater flow at Yucca Mountain suggest that faults may be one of the primary features that control flow. However, their effects on flow and transport remain unknown. Given the scope of the problem, numerical modeling serves as the most effective tool to investigate the potential effects of faults on saturated zone flow.

### 1.3 Objectives

As described above, previous saturated zone models of Yucca Mountain do not incorporate the features necessary to test hypotheses regarding the properties of faults and their potential effects on flow and transport. The models either lack the detail of the geologic structure, or they do not incorporate the features and/or processes that are hypothesized to exist. Furthermore, all models suggest that the relatively large gradients are due to low-permeability fault zones. The aim of this work was to investigate the potential effects of the faulted geologic structure on saturated zone flow at Yucca Mountain using a numerical model. In this context, the model was used as an exploratory tool, not for prediction of flow and transport. More generally, this study provides new understanding of flow and transport behavior in faulted formations.

The objectives of this work were to

- Develop a new 3-D model of the saturated zone that accurately replicates the complex hydrogeologic structure. This includes explicit representation of the hydrogeologic layers, which have variable thicknesses and orientations, and which are displaced by numerous faults. The model must also be laterally and vertically extensive such that current hypotheses can be tested, and discretization should enable simulation of pumping tests.

- Discretize faults such that fault displacement varies along fault strike, and so that they can be modeled as discrete planar structures or finite-width zones of altered rock.

- Examine the causes and effects of vertical head gradients.

- Test the upwelling-through-faults hypothesis.

- Examine the effects of vertical flow on vertical dispersion.

- Examine the effects of increased infiltration on groundwater flow.

- Examine the effects of unsaturated zone transport pathway on contaminant flow in the saturated zone.

- Seek alternative mechanisms that produce thermal anomalies at the water table.

- Show how different fault types control flow channeling and macrodispersion of potential contaminants from the repository.

# 2. Geology and Hydrology at Yucca Mountain

## 2.1 Stratigraphy

The stratigraphic section at and in the vicinity of Yucca Mountain consists of Paleozoic sedimentary and possibly igneous rocks overlain by Tertiary tuffaceous rock that formed from ash flow deposits approximately 11 to 15 million years ago (Carr *et al.*, 1986; Snyder and Carr, 1982). The tuffs at Yucca Mountain are more than 2000 m thick. Table 2.1 shows the stratigraphic and hydrogeologic units at Yucca Mountain.

Table 2.1. Stratigraphic and hydrogeologic units at and around Yucca Mountain (Luckey *et al.*, 1996).

<table>
<tr><th>Period</th><th colspan="2">Stratigraphic Unit</th><th>Hydrogeologic Unit</th></tr>
<tr><td>Quaternary</td><td colspan="2">Alluvium</td><td rowspan="3"></td></tr>
<tr><td rowspan="6">Tertiary</td><td>Timber Mountain Group</td><td>Ranier Mesa Tuff</td></tr>
<tr><td rowspan="2">Paintbrush Group</td><td>Tiva Canyon Tuff<br>Yucca Mountain Tuff<br>Pah Canyon Tuff</td></tr>
<tr><td>Topopah Spring Tuff</td><td>Upper Volcanic Aquifer</td></tr>
<tr><td colspan="2">Calico Hills Formation</td><td>Upper Volcanic Confining Unit</td></tr>
<tr><td>Crater Flat Group</td><td>Prow Pass Tuff<br>Bullfrog Tuff<br>Tram Tuff</td><td>Lower Volcanic Aquifer</td></tr>
<tr><td colspan="2">Lithic Ridge Tuff</td><td rowspan="2">Lower Volcanic Confining Unit</td></tr>
<tr><td colspan="2">Older tuffs, lavas, and breccias</td></tr>
<tr><td>Early Permian and Pennsylvanian</td><td colspan="2">Tippipah Limestone</td><td>Upper Carbonate Aquifer</td></tr>
<tr><td>Mississippian and Late Devonian</td><td colspan="2">Eleana Formation</td><td>Upper Clastic Confining Unit</td></tr>
<tr><td>Devonian to Cambrian</td><td colspan="2">Undifferentiated, primarily carbonate rocks</td><td>Lower Carbonate Aquifer</td></tr>
<tr><td>Cambrian</td><td colspan="2">Undifferentiated, primarily clastic rocks</td><td>Lower Clastic Confining Unit</td></tr>
</table>

The oldest rocks in the sequence are undifferentiated clastic sedimentary rocks, which are overlain by a sequence of undifferentiated carbonate rock that is approximately 5 km thick. This unit defines the Lower Carbonate Aquifer. The Eleana formation is a 2.5 km confining unit, and the Tippipah Limestone is approximately 1 km thick and defines the Upper Carbonate Aquifer (Carr *et al.*, 1986; Fridrich *et al.*, 1994). All four formations are referred to as the Carbonate Aquifer in this report.

The older tuffs are present in only one borehole at the site and are at least 550 m thick (Carr *et al.*, 1986). Most of these rocks are altered, low permeability clays and zeolites. The older lava flows and breccias occur in a section northwest of the proposed repository and are up to 200 m thick where present. Cores of the lava have little primary fracturing and are among the least permeable rocks at the mountain (Fridrich *et al.*, 1994).

The Lithic Ridge Tuff, 0-350 m thick, is a relatively homogeneous and nonwelded tuff with very fine grained precipitates of clays and silica. The Lithic Ridge Tuff, older tuffs, and lava flows and breccias define the Lower Volcanic Confining Unit.

The Crater Flat Group is approximately 550 m thick and consists of the Tram, Bullfrog, and Prow Pass Tuff. Each unit is variably welded with depth and most often has a densely welded zone near the center, which is surrounded by non- or partially to moderately welded intervals. Densely welded tuff has distinct columnar fractures and low porosity. Nonwelded tuff has a lower permeability and larger porosity. The Crater

Flat Group defines the Lower Volcanic Aquifer and is present at the water table near the proposed repository.

The Calico Hills Formation is approximately 30-400 m thick and is mainly nonwelded and zeolitized beneath the water table. This unit defines the Upper Volcanic Confining Unit.

The Paintbrush Group is approximately 430 m thick and consists of the Topopah Spring Tuff, Pah Canyon Tuff, Yucca Mountain Tuff, and Tiva Canyon Tuff. The Topopah Spring Tuff is the thickest and most laterally extensive unit within the Paintbrush Group. It is densely welded throughout and has numerous lithophysal horizons, which have high porosity due to the entrapment of vapor during cooling. The Topopah Spring Tuff is very permeable because it has the most primary and secondary fracturing. It defines the Upper Volcanic Aquifer, although it is mostly present in the unsaturated zone at Yucca Mountain. The base of the Topopah Spring Tuff consists of a low permeability vitric zone called the basal vitrophyre. This layer is also part of the Upper Volcanic Confining unit.

The Pah Canyon and Yucca Mountain Tuff are not laterally extensive. They are present northwest of the proposed repository and have a maximum cumulative thickness of approximately 150 m. The Tiva Canyon Tuff is approximately 15 m thick and is extensive over the site. It consists of an upper moderately welded zone underlain by a low permeability basal vitrophyre. The Rainer Mesa Tuff is present in isolated wedges

between faults. Finally, little alluvium covers the mountain, except in local valleys where it is as much as 180 m thick.

## 2.2 Structure and Faulting

Faulting began approximately 18 million years ago and ended 11.4 million years ago, after emplacement of most of the volcanic units and well after deposition of units that are now beneath the water table. Figure 2.1 is an aerial view of mapped and inferred faults at Yucca Mountain. Day *et al.* (1996) divide the faults into three main groups. The dominant set is composed of north-trending normal faults that have steep down-to-the-west displacement over most of their length. These faults generally have vertical offsets ranging from tens to hundreds of meters and are laterally continuous for tens of kilometers. They define the boundaries of the relatively intact blocks of east-dipping volcanic strata and have therefore been termed block-bounding faults. They dip between 70° to 80°, except for the Paintbrush Canyon Fault, which dips approximately 60° (Clayton *et al.*, 1997). The strata between the normal faults dip 5° to 10° to the east. The second fault set is composed of northwesterly striking strike-slip faults located north of the proposed repository. These faults have vertical offsets on the order of meters to tens of meters and are laterally continuous for tens of meters to a few kilometers. Intrablock faults define the third set. They are continuous on scales less than the defined fault blocks and are not connected with other faults. In addition, they probably do not persist to the water table (Day *et al.*, 1996).

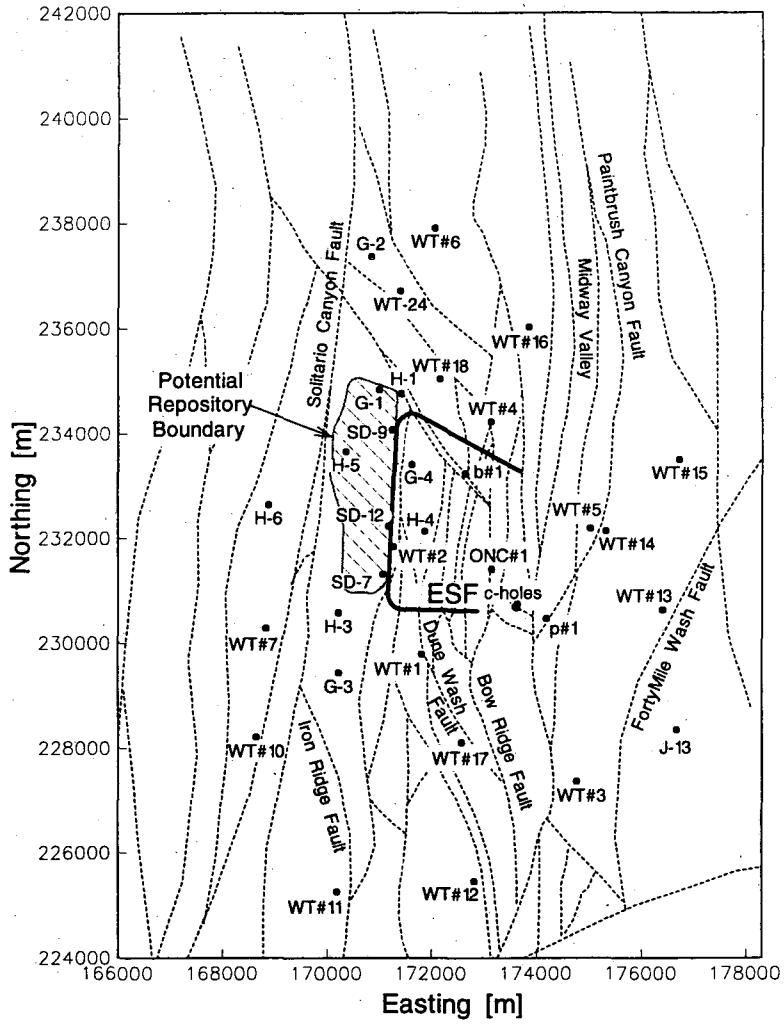


Figure 2.1. Faults at Yucca Mountain, as defined by the ISM2.0 3-D Geologic Framework and Integrated Site Model of Yucca Mountain (Clayton *et al.*, 1997). The Exploratory Studies Facility (ESF) is a testing tunnel in the unsaturated zone. Coordinates are Nevada State Plane coordinates. Figure courtesy of Jennifer Hinds, Lawrence Berkeley National Laboratory.

Both brecciated and non-brecciated faults are observed in boreholes and at the surface. Dickerson and Spengler (1994) mapped 8 km of the Paintbrush Canyon Fault scarp exposed north of Yucca Wash (north of WT #16, Figure 2.1). At several locations the fault is only a 1 m wide zone and is composed of polished planes and cemented breccia layers. However, a 50 m wide brecciated zone is present at the Paintbrush Canyon Fault

exposure west of Busted Butte (near WT #3, Figure 2.1) (R. Dickerson, U.S. Geological Survey, pers. comm., 1996).

## 2.3 Hydraulic Gradients

### 2.3.1 Water Table

Figure 2.2 shows the water table at Yucca Mountain. The contours are based on measurements in 1993. Several measurements were made earlier and are described below. The contours indicate groundwater migrates east and southeast from the proposed repository. In general, there is a small, moderate, and large hydraulic gradient zone. The large gradient zone is northwest of the proposed repository and the gradient is approximately 0.125. The moderate gradient zone is west of the site along the Solitario Canyon Fault, across which the head drop is approximately 45 m and the gradient is 0.05. Groundwater beneath and downgradient from the repository flows under a small gradient between 0.0001 and 0.0003 (Luckey *et al.*, 1996). Table 3.1 lists the water levels and hydraulic heads measured in saturated zone boreholes. The full name of each borehole has a three to four character prefix, but these are omitted here for brevity.

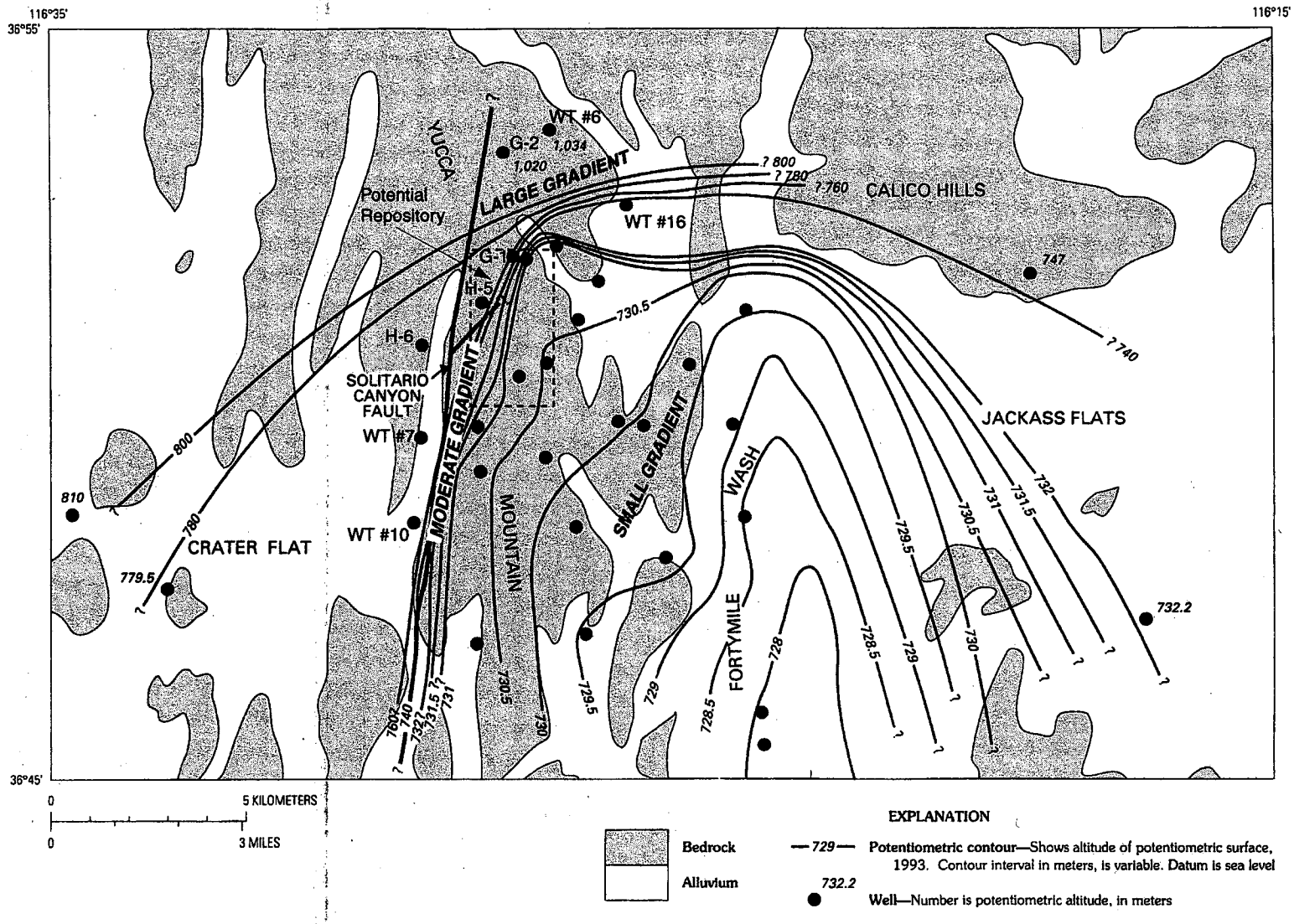


Figure 2.2. Water table surface at Yucca Mountain (modified from Tucci and Burkhardt, 1995).

Table 2.2. Water levels and hydraulic heads in saturated zone boreholes at Yucca Mountain. Geologic units within packed-off intervals are also shown.

| Borehole | Potentiometric Altitude [masl] | | Depth Interval [m] | Geologic Unit |
|---|---|---|---|---|
| WT #1 | 730.35 | (3) | | |
| WT #2 | 730.65 | (3) | | |
| WT #3 | 729.64 | (3) | | |
| WT #4 | 730.78 | (3) | | |
| WT #6 | 1034.6 | (3) | | |
| WT #7 | 775.83 | (3) | | |
| WT #10 | 776.00 | (3) | | |
| WT #11 | 730.66 | (3) | | |
| WT #12 | 729.47 | (3) | | |
| WT #13 | 729.11 | (3) | | |
| WT #14 | 729.68 | (3) | | |
| WT #15 | 729.22 | (3) | | |
| WT #16 | 738.27 | (3) | | |
| WT #17 | 729.70 | (3) | | |
| WT #18 | 730.75 | (3) | | |
| H-1, tube 4 | 730.85 | (3) | 573-673 | Prow Pass Tuff |
| H-1, tube 3 | 730.60 | (3) | 716-765 | Bullfrog Tuff |
| H-1, tube 2 | 735.97 | (3) | 1097-1123 | Tram Tuff |
| H-1, tube 1 | 785.49 | (3) | 1783-1814 | Older tuffs |
| H-3, upper | 731.52 | (3) | 753-1061 | Tram Tuff |
| H-3, lower | 755.91 | (3) | 1061-1219 | Tram and Lithic Ridge Tuff |
| H-4, upper | 730.40 | (3) | 518-1181 | Prow Pass to Lithic Ridge Tuff |
| H-4, lower | 730.51 | (3) | 1181-1219 | Lithic Ridge Tuff |
| H-5, upper | 775.46 | (3) | 704-1091 | Bullfrog and Tram Tuff |
| H-5, lower | 775.62 | (3) | 1091-1219 | Lavas |
| H-6, upper | 776.02 | (3) | 526-752 | Prow Pass to Tram Tuff |
| H-6, lower | 775.94 | (3) | 752-1220 | Tram and Lithic Ridge Tuff |
| G-1 | *753.8 | (4) | | |
| G-2 | 1020.28 | (1) | | |
| G-3 | 730.50 | (3) | | |
| G-4 | *730.1 | (4) | | |
| b#1, upper | 730.65 | (3) | 471-1199 | Calico Hills Formation to Tram Tuff |
| b#1, lower | 729.67 | (3) | 1199-1220 | Tram and Lithic Ridge Tuff |
| c-holes | 730.03 | (2) | | |
| p#1 | 752.44 | (3) | 1297-1805 | Older tuffs and Paleozoic units |
| J-13 | 728.44 | (3) | | |

References: 1. Craig, 1995; 2. Ervin *et al.*, 1994; 3. Graves *et al.*, 1997; 4. Robison, 1984

Notation: * only 1 measurement in 1983

### 2.3.2 Large Hydraulic Gradient Zone

The large gradient zone was originally defined by water levels in boreholes G-1, G-2, WT #6, and WT #16 (Robison, 1984). Large gradients are often present in southern Nevada and are easily explained, since they occur near large structural features such as at the edges of thick confining units, at faults with major offset, at caldera boundaries, or at mountain range fronts (Luckey *et al.*, 1996). However, such a structure is not observed near the large gradient zone at Yucca Mountain. Fridrich *et al.* (1994) proposed two possible mechanisms. They argue that an aeromagnetic high, a geothermal heat flux low near the large hydraulic gradient zone, and isotopic data suggest that a buried graben and associated fault zone underlie the area of the large hydraulic gradient zone. One model assumes the buried fault zone acts as a high permeability conduit that allows fluid to migrate downward, thereby resulting in a sudden decline in the water table. The second model suggests that a rapid increase in thickness of the Crater Flat Group acts essentially as a spillway resulting is a rapid decline in the water level. Other workers suggest that flow through a thick confining unit causes the gradient, or that the Lower Volcanic Aquifer has a low permeability in that zone due to lithostatic pressure and hydrothermal alteration (Luckey *et al.*, 1994). Ervin *et al.* (1994) suggest that a perched water body produces the large gradient. Previous sub-site-scale saturated zone flow models of Yucca Mountain assume that a linear and vertically continuous low permeability feature is present here (Arnold *et al.*, 1998; Wilson *et al.*, 1994; Zyvoloski *et al.*, 1997), although there is no field evidence indicating that such a structure exists.

### 2.3.3 Moderate Hydraulic Gradient Zone

The moderate hydraulic gradient zone is thought to be associated with the Solitario Canyon Fault, and it is defined by water levels in boreholes WT #10, WT #7, H-6, and by water levels on the eastern side of the fault. The water levels in these boreholes are approximately 45 m higher than those on the eastern side of the fault. An exception is the 775 m elevation observed in H-5. This elevation may result from a local hydraulic connection to the western side of the fault by a splay of the Solitario Canyon Fault, which was observed at the surface and interpolated to intersect the well (Ervin *et al.*, 1994). The fault may function as a barrier to flow because strata are offset by as much as 250 m, which would result in termination of the lower volcanic aquifer against the lower volcanic confining unit. The fault may also function as a barrier because of low permeability gouge. Fault gouge and siliceous infilling are present at the surface along the fault and have measured low matrix porosities. If the gouge persists beneath the water table, it could have lower permeability than the surrounding rock and create a moderate gradient (Luckey *et al.*, 1996). Sub-site-scale saturated zone flow models of Yucca Mountain assume that a linear and vertically continuous low permeability feature produces the moderate gradient (Arnold *et al.*, 1998; Wilson *et al.*, 1994; Zyvoloski *et al.*, 1997). Fridrich *et al.* (1994) suggest that the moderate gradient could result from upwelling of water along the fault from the Carbonate Aquifer.

### 2.3.4 Small Hydraulic Gradient Zone

The small hydraulic gradient zone extends eastward from the proposed repository. It is defined by water table elevations ranging from 731 to 728 m, and the gradient ranges

from 0.0001 to 0.0003. Potential radionuclides percolating from the repository will be transported in the small gradient zone. The small gradient may be due to flow in high permeable rocks or to minimal flux due to restriction of flow from the west and northwest (Luckey *et al.*, 1996).

### 2.3.5 Vertical Hydraulic Gradients

Upward flow in the lower volcanic aquifer and possibly upwelling of water from the Carbonate Aquifer is suggested by the presence of upward vertical hydraulic gradients. Borehole p#1 is located next the Paintbrush Canyon Fault (Figure 2.1) and is the only borehole that penetrates the Carbonate Aquifer, where the head is approximately 21 m greater than the water table elevation (Table 2.2). The increased head was encountered in the lowermost section of the older unnamed tuffs beneath the Lithic Ridge Tuff. It is unclear weather or not the Carbonate Aquifer and Lower Volcanic Aquifer are hydraulically connected, however, since water levels in p#1 did not change during pumping at the nearby c-hole complex (Luckey *et al.*, 1996). Hydraulic heads in packed-off intervals in boreholes H-1 and H-3 also indicate large upward, vertical gradients. In H-1 the head in the older unnamed tuffs is approximately 55 m greater than in the Bullfrog Tuff. In H-3 the head difference between the upper and lower section of the borehole is approximately 24 m upward. Upward head gradients were also observed in boreholes H-4, H-5, and b#1, and a downward vertical gradient is present in a section of borehole H-1 and H-6. The vertical head differences are less than 26 cm in boreholes H-1, H-4, H-5, and H-6 , and less than 1 m in borehole b#1.

Twenty-six water level measurements in G-4 were made at different depths during and after drilling, and sometimes during pumping tests. The difference in measured levels is less than the measurement accuracy (+/- 0.5 m) (Bentley, 1984). Therefore, a vertical gradient cannot be defined, as in Luckey *et al.*, 1996. The water level in April, 1983 was 730.1 m (Robison, 1984). This is considered the best estimate of the water table elevation in G-4.

## 2.4 Perched Water

Ervin *et al.* (1994) propose that the large hydraulic gradient is an apparent feature that results from using elevations of perched water bodies to define the water table. Indeed, Winograd and Thordarson (1975) reported that perched water is not uncommon at and in the vicinity of the Nevada Test Site, and recent work in the unsaturated zone at Yucca Mountain strongly supports a perched water model. Perched water was observed in 5 unsaturated zone boreholes in the area of the large hydraulic gradient. Figure 2.3 shows the boreholes in which perched water was observed, as well as the saturated zone boreholes that define the large gradient. All of the perched water was encountered at the contact of the low permeability basal vitrophyre of the Topopah Spring Formation and the zeolitic horizon in the Calico Hills Formation. Both units act as confining layers. Data from the saturated zone boreholes also support a perched water model. For example, the water elevations in G-2 have declined slowly from 1032 m in 1981 (Czarnecki *et al.*, 1994) to approximately 1020 m as of 1995 (Craig, 1995). Recent pumping tests by O'Brien (1998) show a drawdown transient that indicates the presence of nearby boundaries, which would result because perched water bodies are not laterally

continuous. Also, neutron logging in G-2 shows that the Calico Hills formation immediately beneath the perching horizon in less than 100% saturated, whereas the Prow Pass Tuff is completely saturated at approximately 730 m (Wu *et al.*, 1996). This is approximately equal to the water table elevations in the small gradient zone. Finally, the water levels in WT #6 and WT #16 are also near the contact of the Topopah Spring basal vitrophyre and underlying Calico Hills formation. Figure 4.10 in Chapter 4.5 shows that the apparent water table elevations in the northwestern boreholes are in the Calico Hills formation. If perched water is the cause of the apparent large hydraulic gradient, the northern boundary of the small gradient zone may extend further to the northwest. Groundwater originating beneath the repository would therefore flow eastward, rather than to the southeast as implied by the water table map of Ervin *et al.* (1994).

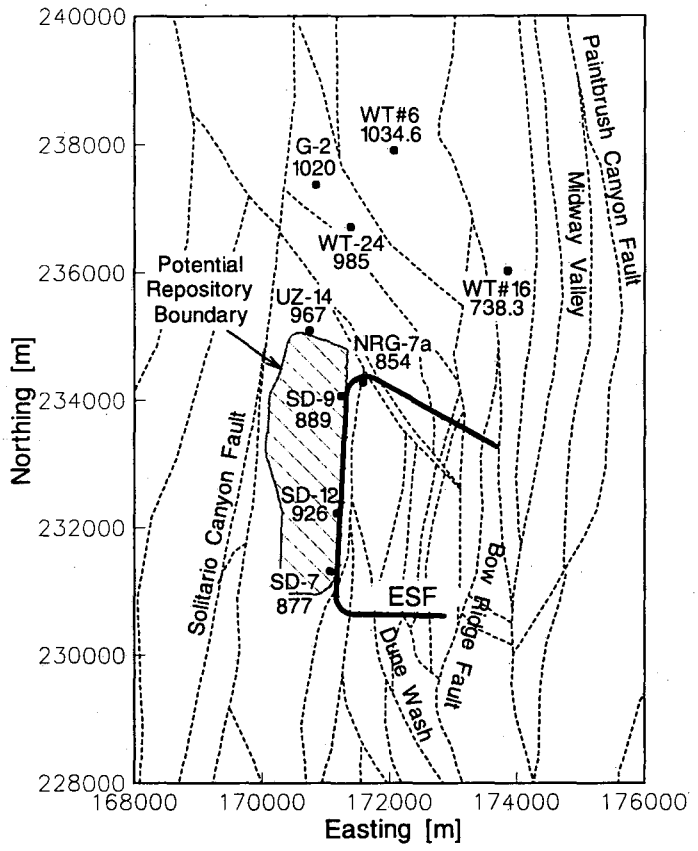


Figure 2.3. Boreholes in which perched water was observed. Figure courtesy of Jennifer Hinds, Lawrence Berkeley National Laboratory.

## 2.5 Hydrogeologic Properties

Borehole flow surveys show that fractured zones are the dominant pathways for groundwater in the lower volcanic aquifer. More than 90% of water pumped from the tuffs in the Crater Flat Group commonly emanates from the densely welded and fractured intervals, which are typically located in the central section of a particular unit. In addition, permeability measurements from pumping tests are several orders of magnitude larger than matrix permeability (Anderson, 1991; Anderson, 1994; Geldon, 1993; Lahoud *et al.*, 1984; Rush *et al.*, 1984), indicating that flow is primarily through fractures.

However, estimates of ground water travel time are poorly constrained because fracture porosity has not been measured sufficiently in the saturated zone. The lower volcanic confining unit is not significantly fractured and estimates of permeability from pumping tests are approximately equal to core tests, indicating a matrix dominated flow system.

Permeabilities of the different hydrogeologic sections are not well defined. Most estimates were determined from pumping and injection tests in the 1980's, shortly after the deep boreholes were drilled (Luckey *et al.*, 1996). These tests were single-hole tests, and with the exception of several tests, the data are not reliable and are poorly matched by analytic solutions. The c-holes are the only boreholes at which multi-well pumping tests were performed (Geldon, 1993, 1996). These tests provide the most reliable estimates of transmissivity of the Crater Flat Group.

Permeability estimates of the different hydrogeologic units are listed in Table 2.3. The sources of these estimates are described in Chapter 5 in the context of assigning model properties.

Table 2.3. Estimated permeability of hydrogeologic units.

| Hydrogeologic unit | Permeability [$m^2$] |
|---|---|
| Upper Volcanic Aquifer | $10^{-12}$ |
| Upper Confining Unit | $10^{-15}$ |
| Lower Volcanic Aquifer | $10^{-11}$-$10^{-15}$ |
| Lower Volcanic Confining unit | $10^{-17}$ |
| Carbonate Aquifer | $10^{-13}$ |

Fault zone permeability is also poorly defined. For example, a non-pumping heat-pulse flowmeter survey in borehole UE25 c#3 showed that nearly 4 gpm emanated from a 6 m brecciated fault interval (Geldon, 1996). Conversely, some faults in the saturated zone are not significantly brecciated and do not show signatures of high permeability (Craig and Robison, 1984). Fault zone permeability has only been measured in an unsaturated section of the Bow Ridge Fault (LeCain, 1998). The average fault zone permeability is $2.6 \times 10^{-11}$ $m^2$, based on air injection tests . In addition, using pneumatic diffusivity and fracture frequency measurements, fracture permeability for fault zones of normal faults in the Topopah Spring Tuff and younger units was estimated to range from $3 \times 10^{-13}$ to $10^{-11}$ $m^2$ (Bodvarsson *et al.*, 1997).

Ahlers (1996) suggests that fault permeability may vary vertically in accordance with the surrounding formation. Faulting may produce more fracturing in the densely welded, brittle formations and less fracturing in the non- to partially welded units. He suggests this may be one explanation for the different pneumatic diffusivities calculated for areas where the faults penetrate welded rock, as compared to less welded units.

Contaminant travel time in both volcanic aquifers will be defined by the fracture porosity because fractured zones are the most permeable pathways. Erickson and Waddell (1985) estimated fracture porosity beneath the water table. First, they used temperature logs to identify the discrete fractured intervals. Using the estimated transmissivity and the number of flow intervals where water entered the borehole during pumping, they calculated an aperture for each interval assuming a cubic law relationship. They then

summed the apertures and divided by the length of the tested section to calculate the fracture porosity. Their estimated fracture porosity is between $10^{-4}$ to $10^{-3}$. Other work yielded similar estimates. Calibration of an unsaturated zone model yielded a porosity of $2.8 \times 10^{-4}$ (Bodvarsson *et al.*, 1997). Sonnenthal *et al.* (1997) analyzed fracture frequency and fracture lengths in the Exploratory Studies Facility (ESF) tunnel in the unsaturated zone to calculate fracture porosity. Their estimates range from $10^{-5}$ to $10^{-4}$.

Matrix porosity beneath the water table was measured from core samples and generally ranges between 0.20 and 0.30 (Anderson, 1991; Anderson, 1994; Geldon, 1993; Lahoud *et al.*, 1984; Lobmeyer, 1986; Rush *et al.*, 1984; Thordarson, 1983).

## 2.6 Hydrochemistry

Geochemical data of saturated zone waters at and around Yucca Mountain has been used to describe regional flow paths and to infer the sources of groundwater and role of faults on groundwater flow beneath Yucca Mountain. Luckey *et al.* (1996) report all of the hydrochemical data collected at and around Yucca Mountain as of 1995. Data for the immediate Yucca Mountain area were reported by Benson and McKinley (1985) and Matuska (1989) and include activities of carbon-14 ($^{14}C$) and tritium ($^{3}H$), concentrations of major ions, and ratios of stable isotopes. Stuckless *et al.* (1991) used this carbon-isotope data and noted a southward increase in $\delta^{13}C$ in the tuff aquifer south of the large gradient. They suggested this increase may be the result of carbonate-rich waters upwelling from the Carbonate Aquifer. However, the data are questionable because the drilling fluid used was an air-water-detergent mixture, which was not completely

removed prior to sampling. Therefore, the groundwater appears older because the detergents are made from petroleum feedstocks. In addition, they show that $\delta^{13}C$ increases in directions opposite the hydraulic gradient. On a regional scale there is an increase of $\delta^{87}Sr$ from north to south, but the values are not suggestive of flow pathways in the immediate vicinity of Yucca Mountain (Luckey *et al.*, 1996).

Benson and McKinley (1985) also measured concentrations of the dissolved solids such as calcium and sodium. Their data shows that the Ca-Na ratio increases approximately 10 times from the west side to the east side of Yucca Mountain. An increase in calcium in the direction of groundwater flow could be due to ion-exchange with zeolites or upwelling of waters from the Carbonate Aquifer on the east side of Yucca Mountain, for example. However, these contributions may not exist, as corrected $^{14}C$ ages indicate groundwater west of Yucca Mountain is 11,000 to 12,000 years old (Kwicklis, 1997), whereas water beneath Forty Mile Wash to the east is 4,000 to 7,000 years old. The concentration of calcium in groundwater to the east could therefore be greater than to the west because of recent percolation through caliche beneath Forty Mile Wash. In general, while several distinctly different hypotheses can be made based on the hydrochemical data, the data are too scarce or of questionable quality to indicate any clear patterns of saturated zone flow at the sub-site-scale.

## 2.7 Geothermal Gradient

Temperature measurements in the saturated zone show that water table temperatures are higher than average parallel to and around the southern portion of the Solitario Canyon

Fault and, to a lesser degree, around the Paintbrush Canyon Fault near Midway Valley (Figure 2.4). Several authors have proposed that the anomalous temperatures result from warmer fluid upwelling from deeper units through permeable fault zones in the Solitario Canyon and Paintbrush Canyon Faults (Fridrich *et al.*, 1994; Szymanski, 1989). Fridrich *et al.* (1994) propose that upwelling from the Carbonate Aquifer is indicated at least along the Solitario Canyon Fault zone. Fluid upwelling is the only hypothesis that has been proposed to date to explain the temperature data.

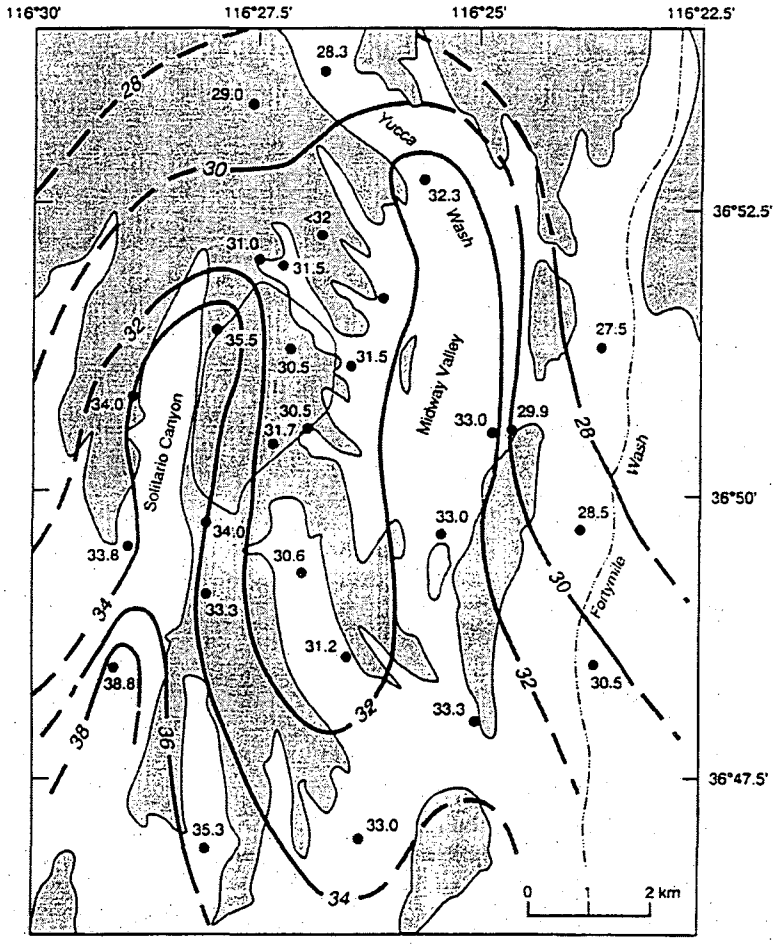


Figure 2.4. Temperature distribution at the water table (from Sass *et al.*, 1995).

## 2.8 Conceptual Model of Groundwater Flow

The hydrogeologic structure at Yucca Mountain is complex. Borehole flow logs show that most water is pumped from zones of densely welded and fractured sections of tuff, typically located in the central section of the Prow Pass, Bullfrog, and Tram Tuff of the Lower Volcanic Aquifer. This is the aquifer closest to the water table over most of the area within 5 km downgradient from the proposed repository. Nonwelded tuff has relatively few open fractures, and is therefore less permeable. The nonwelded tuff layers are present above and below the more densely welded intervals and are sub-parallel to dip, thereby creating a layered system. In addition, the permeability at the water table is heterogeneous because layers dip and are faulted (Figure 2.5).

Faults are pervasive at Yucca Mountain. The normal faults have vertical offsets on the order of tens to hundreds of meters and are laterally continuous for 10 kilometers or more. The normal displacement results in a contact between high permeability layers and low permeability layers across the fault. If brecciated fault zones exist, they could provide vertical pathways that link the displaced high permeability zones. Conversely, mineralization within a fault zone could create a flow barrier even if a high permeability unit is not discontinuous across a fault.

Alternatively, water between low permeability faults may be effectively isolated and have velocities orders of magnitude less than in surrounding regions. This phenomenon would enhance the storage capability of portions of the saturated zone. It is also possible that low permeability faults can act as laterally extensive flow barriers so that water could be

diverted along strike for several kilometers. In any case, fault displacement produces large-scale permeability heterogeneity and, therefore, large-scale channeling and/or mechanical dispersion.

The small gradient east of the repository may be the result of relatively low fluxes due to a flow barrier effect created by the Solitario Canyon Fault or because this region has a high permeability. Water elevations west of the Solitario Canyon Fault are approximately 45 m higher than those in the small gradient zone. This difference could be explained by the presence of low permeability fault gouge, for example. However, thermal anomalies at the water table and upward hydraulic gradients seem to suggest that water upwells through a permeable fault zone. In addition, a large gradient is present northwest of the proposed repository. Data from unsaturated zone boreholes strongly supports a perched water hypothesis; the large gradient is an apparent gradient that results from using perched water elevations to define water table elevations. If this is the case, the small gradient zone may extend to what is now considered the large gradient zone, which would suggest a more easterly, rather than southeasterly groundwater flow.

Due to their continuity and large offset, block bounding faults are considered the dominant large-scale features that control groundwater flow. Faults that do not have a significantly altered zone are termed "displacement-only faults" in this work, whereas faults with brecciated zones are termed "high permeability faults," or "low permeability faults," as appropriate.

In general, the layering of geologic units that have variable thickness and orientation, coupled with the variable displacement of these units by faults, is a primary feature that controls groundwater flow at Yucca Mountain. However, the ways in which groundwater flows in this system have only been hypothesized. Numerical modeling is one way to study the effects of this structure on groundwater flow so that the question of viability of the saturated zone as a "natural barrier" to radionuclide transport can be addressed more thoroughly.

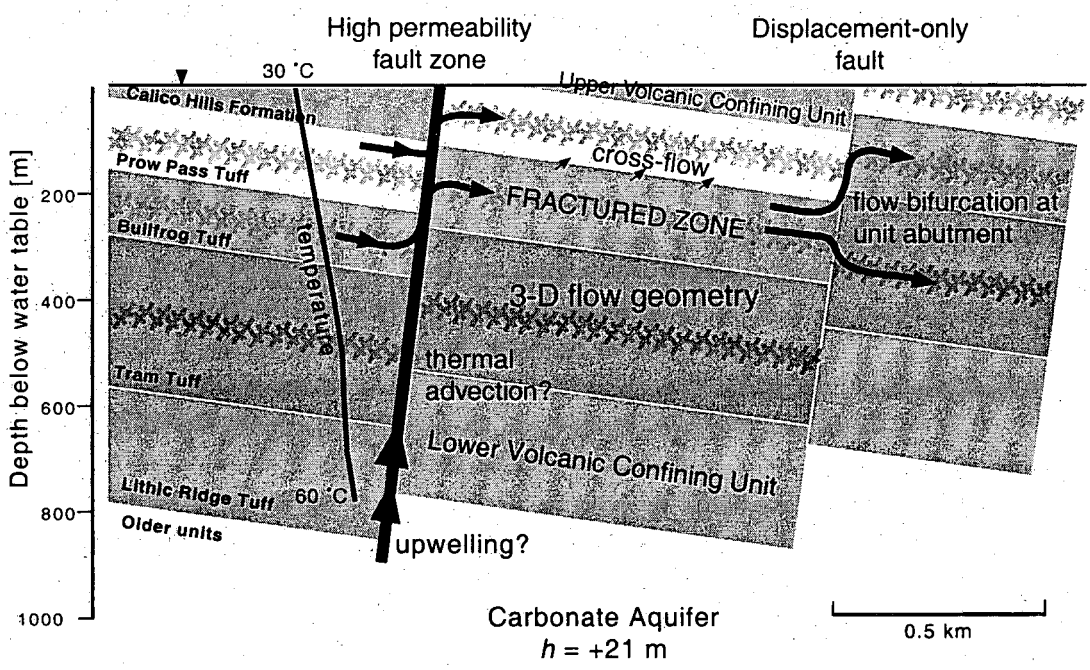


Figure 2.5. Conceptual model of groundwater flow at Yucca Mountain.

# 3. Modeling Approach

## 3.1 Flow Simulator

TOUGH2 (Pruess, 1987; Pruess, 1991a; Pruess *et al.*, 1996) is used to simulate flow. TOUGH2 is a numerical simulation code for multi-dimensional coupled fluid and heat flow of multi-phase, multi-component fluid mixtures in porous and fractured media. It is based on the integral finite difference method, which uses the mass and energy continuity equations in an integral form. Besides its capability to simulate numerous processes, a benefit of this formulation is that it applies to regular or irregular spatial discretization in one, two, or three dimensions (Pruess, 1991a). The model mesh can therefore be constructed of irregular polygons of varying geometries. This provides the means to accurately represent a detailed and complex geologic formation, such as the faulted rocks at Yucca Mountain. Traditional finite-difference models can be discretized with rectilinear volume elements only. The formulation needed to consider irregular grid blocks is summarized briefly below.

### 3.1.1 Governing Equations

Summarizing from Pruess (1991a), the basic mass- and energy-balance equation solved by TOUGH2 has the following form:

$$\frac{d}{dt}\int_{V_n} M^{(\kappa)} dV = \int_{\Gamma_n} \mathbf{F}^{(\kappa)} \cdot n \, d\Gamma + \int_{V_n} q^{(\kappa)} dV \, . \qquad (3.1)$$

Equation 3.1 describes flow in arbitrarily shaped subdomains of volume $V_n$ with a closed surface, $\Gamma_n$. The quantity $M^{(\kappa)}$ denotes mass or energy per unit volume of flow component $\kappa$. $\mathbf{F}^{(\kappa)}$ is the mass or energy flux of component $\kappa$ at the surface, where

$\kappa = 1,...NK$ (number of components), and $\kappa = NK+1$ is the heat component. $q^{(\kappa)}$ is the source/sink term.

The total mass of component $\kappa$ is the sum of masses from each phase, $\beta$:

$$M^{(\kappa)} = \phi \sum_{\beta=1}^{NPH} S_\beta \rho_\beta X_\beta^{(\kappa)}; \tag{3.2}$$

where $\phi$ is porosity, $S$ is saturation, $\rho$ is density, $X$ is mass fraction, and NPH is the number of phases. The mass flux term is a sum of the different phases:

$$\mathbf{F}^{(\kappa)} = \sum_{\beta=1}^{NPH} X_\beta^{(\kappa)} \mathbf{F}_\beta . \tag{3.3}$$

The individual fluxes are given by a multi-phase version of Darcy's law:

$$\mathbf{F}_\beta = -k \frac{k_{r\beta}}{\mu_\beta} \rho_\beta \left( \nabla P_\beta - \rho_\beta \mathbf{g} \right), \tag{3.4}$$

where $k$ is the absolute permeability, $k_{r\beta}$ is the relative permeability of phase $\beta$, $\mu_\beta$ is viscosity, and $\mathbf{g} = g \cos\theta$ is the gravity vector in the flow direction $\theta$. In addition,

$$P_\beta = P + P_{c,\beta}, \tag{3.5}$$

where $P_c$ is capillary pressure.

Heat conduction and convection are considered:

$$\mathbf{F}^{(NK+1)} = -K \nabla T + \sum_\beta h_\beta \mathbf{F}_\beta , \tag{3.6}$$

where $K$ is thermal conductivity, and $h_\beta$ is the specific enthalpy of phase $\beta$. The heat accumulation term is

$$M^{(NK+1)} = \phi \sum_{\beta=1}^{NPH} S_\beta \rho_\beta u_\beta + (1-\phi)\rho_R C_R T \,, \qquad (3.7)$$

where $u_\beta$ is the internal energy of fluid phase $\beta$, and $\rho_R$, $C_R$, and $T$ are the rock density, specific heat, and temperature, respectively.

Additional equations are needed to describe the dependence of the fluid parameters such as density, viscosity, enthalpy, vapor pressure, etc. on the primary thermodynamic variables such as pressure, temperature, saturation, and mass fraction. These equations are specified in a number of fluid property modules referred to as "equation-of-state" or "EOS" modules, which enable simulation of different flow processes.

### 3.1.2 Discretization of the Governing Equation

The model mesh is discretized into irregular volume elements (grid blocks) that have a finite number of surface segments and volume $V_n$ (Figure 3.1).

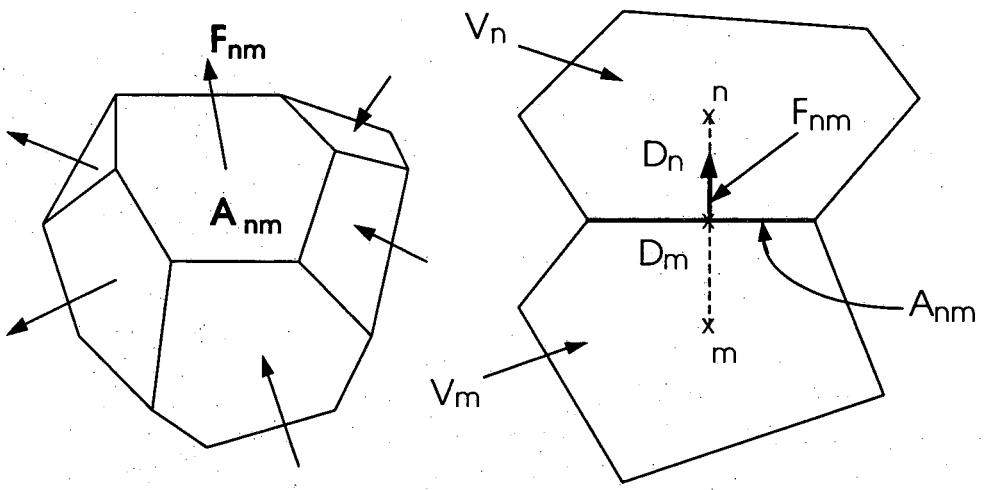


Figure 3.1. Space discretization and grid block specifications in the integral finite difference method (from Pruess *et al.*, 1996).

Using the integral finite difference method (Edwards, 1972; Narasimhan and Witherspoon, 1976), the components of (3.1) can be expressed as follows:

$$\int_{V_n} M dV = V_n M_n, \tag{3.8}$$

where $M_n$ is the average value of $M$ in volume $V_n$. The fluxes through the grid block can be approximated as a discrete sum of fluxes across each surface segment of the grid block, $A_{nm}$:

$$\int_{\Gamma_n} \mathbf{F} \cdot n \, d\Gamma = \sum_m A_{nm} \mathbf{F}_{nm} . \tag{3.9}$$

The flux across each interface is expressed as

$$\mathbf{F}_{\beta,nm} = -k_{nm} \left( \frac{k_{r\beta} \rho_\beta}{\mu_\beta} \right)_{nm} \left[ \frac{P_{\beta,n} - P_{\beta,m}}{D_n + D_m} - \rho_{\beta,nm} \mathbf{g} \right], \tag{3.10}$$

where the subscript *nm* denotes an average parameter value calculated by interpolation, harmonic weighting, or upstream weighting. Simulations in this work use upstream weighting. **g** is specified for every grid block-to-grid block connection in the mesh input file. It is based on the relative x, y, and z coordinates of the grid block nodes.

The source term is expressed as a single average value:

$$\int_{V_n} q^{(\kappa)} dV = q_n^{(\kappa)} . \tag{3.11}$$

Substituting equations (3.8) and (3.9) into (3.1) gives a set of first-order ordinary differential equations in time:

$$\frac{dM_n^{(\kappa)}}{dt} = \frac{1}{V_n}\sum_m A_{nm}\mathbf{F}_{nm}^{(\kappa)} + q_n^{(\kappa)} \tag{3.12}$$

Time is discretized as a first order finite difference, and the equations are solved by a fully implicit time-stepping scheme. For each grid block there are NEQ equations, where NEQ=NK+1 for non-isothermal flow. A model with NEL grid blocks has a total of NEL•NEQ coupled non-linear equations, which include the NEL•NEQ unknown primary variables. The equations are solved by Newton-Raphson iteration using a bi-conjugate gradient solver with incomplete LU decomposition as preconditioner. For a particular time step, iteration proceeds until the residuals are reduced below a predefined convergence criteria. The convergence criteria is $10^{-5}$ for the simulations described in this work. If convergence is not satisfied after 10 iterations, the time step is reduced by a factor of 4 and a new time step is begun. Conversely, the time step is doubled if convergence is achieved in fewer than 4 iterations.

### 3.2 Steady-State and Confined Flow

In this dissertation only steady-state flow is simulated, since only the effects of the hydrogeologic structure on steady-state flow pathways are being studied. The system as a whole is assumed to be steady-state. That is, infiltration and recharge rates, the water table configuration, hydrogeologic properties, and the geologic structure are assumed to remain constant in time. The formation is modeled as a confined aquifer because the water table is a no-flow boundary. Simulation of groundwater flow is performed with

EOS1 (Pruess, 1991a), which describes pure water in its liquid, vapor, and two-phase states. The module provides the option for simulating liquid water only.

### 3.3 Transport Modeling for Flow Visualization

Solute transport simulations are used for the purpose of illustrating groundwater flow pathways. The solute is referred to as a "flow visualization tracer" because it is used only as a visualization tool, not to represent an actual solute. Simulations are performed using the TOUGH2 module EOS7 (Pruess, 1991b), which is used to simulate flow of water and brine. Chapter 6.3.2 describes how EOS7 is used to visualize a flow field.

For the purpose of examining flow pathways, particle tracking is preferable over tracer simulations because the latter is subject to numerical dispersion. The flow visualization tracer is used in this work because particle tracking methods for irregular meshes in an integral finite-difference model were previously unavailable. A new technique to calculate streamlines in irregular meshes was developed during this study, and it can be used in future simulations instead of a flow visualization tracer. This technique is described in Appendix A.

# 4. Model Discretization

## 4.1 General

The 3-dimensional grid block discretization is based on the detailed 3-D geologic model of Yucca Mountain. The discretization was performed in a step-wise manner, beginning with the development of a 2-D aerial mesh which is common to all hydrogeologic layers in the 3-D model. Lithologic logs, drilling history data, and borehole flowmeter and tracejector surveys were analyzed to define permeability-rock type relations as a means to discretize geologic units into hydrogeologic model layers. Each model layer has a variable thickness and orientation, and was horizontally discretized using the 2-D mesh. The layers were then concatenated and grid block connections at faults were discretized to properly account for layer displacement. A variety of unpublished algorithms developed at Lawrence Berkeley National Laboratory were used to construct the model. Several new algorithms were developed to meet specific needs for discretizing the saturated zone model. The full model has 23 layers, and 11 faults are represented explicitly. The mesh has 57,153 grid blocks and 199,854 connections, which use 21.2 Mbytes of disk space.

## 4.2 Geologic Model

The 3-D Geologic Framework and Integrated Site Model of Yucca Mountain (Clayton *et al.*, 1997) was used as the basis for discretizing the saturated zone model. The geologic model represents the geologic structure from the land surface to geologic units beneath the water table, and it has 35 rock layers and 35 faults. It was constructed using data from surface geologic mapping and measured sections at outcrops, lithologic logs, and seismic,

gravity, and magnetic profiles. Firstly, aerial elevation contour and isochore maps of different geologic layers were constructed manually using lithologic logs. The layer elevation maps have discontinuities to account for faults and their offsets, as defined by surface fault traces and preliminary cross-sections and published sources. Contour maps of fault surfaces were then constructed, and geophysical data was used to define basement rocks that are not penetrated by boreholes. Finally, the maps were digitized and visualization software was used to visualize the 3-D geologic structure. The geometric data that defines the 3-D geologic model was used directly to spatially discretize the saturated zone flow model.

### 4.3 Dimensions and Boundaries

The model covers an area of approximately 108 $km^2$, encompassing the proposed repository location and the large, moderate, and small hydraulic gradient zones. The large gradient zone was included to enable future simulations of coupled unsaturated-saturated zone flow. The top of the model is defined by the water table surface of Bodvarsson *et al.* (1996) (Figure 4.1). The lower boundary is defined by the base of the Lower Volcanic Confining Unit, and the model thickness ranges between 400 m and 1.1 km. The minimum elevation is 322 meters below sea level.

The water table in the small gradient area in Figure 4.1 approximately matches the map of Ervin *et al.* (1994), but the contours on the west side of the model do not agree with more recent mapping by Tucci and Burkhardt (1995) (Figure 2.2). Their 800 m isoline trends to the southwest, approximately along the 900 m contour in Figure 4.1. Their

interpolation is based on two water table elevations 6.4 and 8.8 km west of H-6 and on an estimated water level of 779 m in borehole UZ-14, located northwest of borehole H-1. The estimated water table elevation is based on a 1994 altitude of 755 m and a projected static water level once the borehole has equilibrated after drilling. Therefore, the interpolation by Tucci and Burkhardt (1995) has considerable uncertainty, so the water table contours in the large gradient zone in Figure 4.1 are used for the saturated zone model. The elevation of the top of the model in the small gradient area is centimeters to several meters different than the water table surface in Figure 2.2. This difference is considered negligible given the total thickness of the model. Water table calibrations for the small gradient zone were made using the small gradient defined by Tucci and Burkhardt (1995).

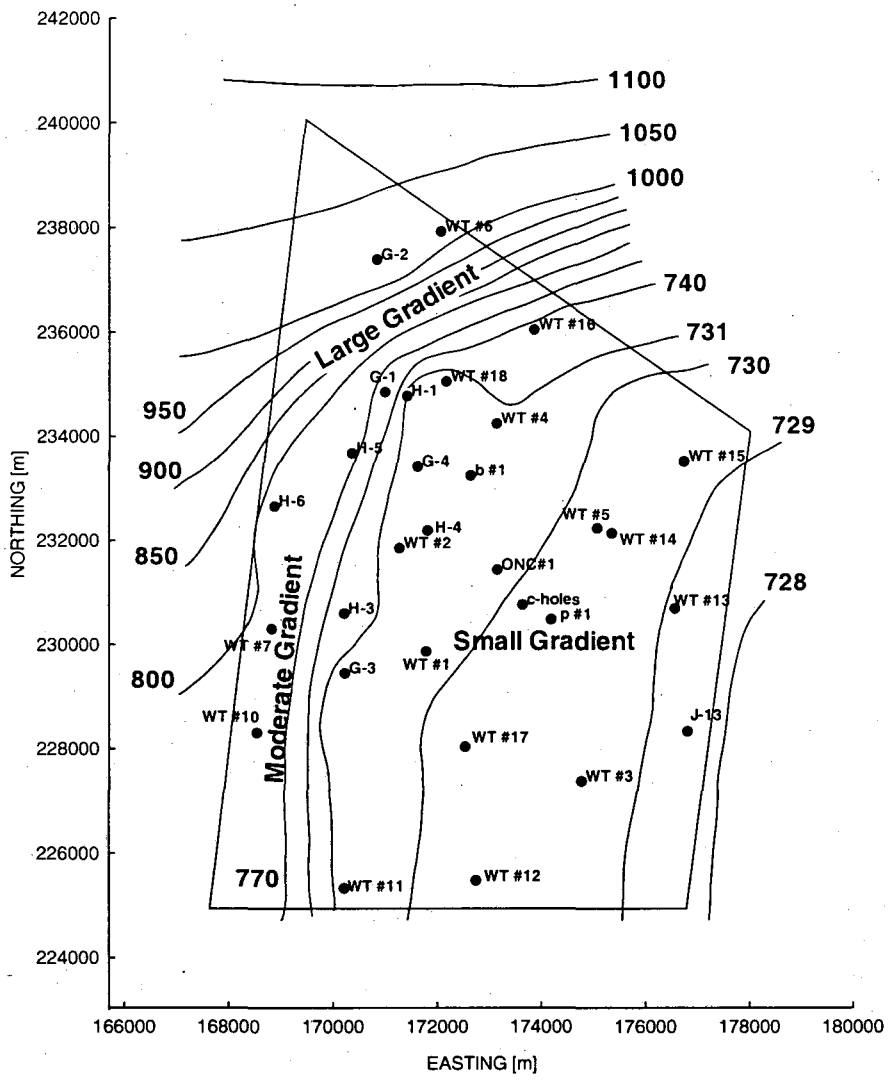


Figure 4.1. Water table map used to define the top of the saturated zone model.

## 4.4 2-D Discretization

As described earlier, the first step in constructing the model is discretization of a 2-D mesh which is common to all model layers. This mesh is composed of irregular polygonal grid blocks which are used to replicate the spatial distribution of faults and to create a locally refined sub-mesh. These grid blocks are created using a computer code that uses the Voronoi tessellation method to construct irregular grid blocks called

Voronoi polyhedra (Voronoi, 1908). The polyhedra are constructed around a set of points in the two-dimensional Euclidean plane. These points are called sites. Each polyhedra is constructed using a nearest-neighbor logic: every point within a Voronoi polyhedra is closest to its site than to any other site. The sides of a polyhedra are perpendicular to the linear connection to each nearest-neighbor site. Aurenhammer (1991) discusses the history and application of Voronoi polyhedra, and Palagi (1992) describes construction of Voronoi meshes for subsurface flow modeling. Pruess and Narasimhan (1985) describe the formulation of flow equations for arbitrary flow domains, which include Voronoi polyhedra. TOUGH2 is based on the same formulation.

Figure 4.2 is an example Voronoi mesh. The grid blocks are defined by the polyhedra sides (solid lines) and the dotted lines are the connections between grid block nodes (sites). The sides of every grid block in Figure 4.2 cross the corresponding perpendicular bisector, although this is not a requirement. TOUGH2 defines the grid block-to-grid block connection distance as the sum of the distances between each node and the connection interface, D1 and D2. For a unit thickness mesh, the interface area between two nodes is equal to the length of the corresponding side of the polyhedra. For variable thickness layers, the lateral interfaces for a grid block are different from one another. An irregular grid block can have any number of sides greater than two.

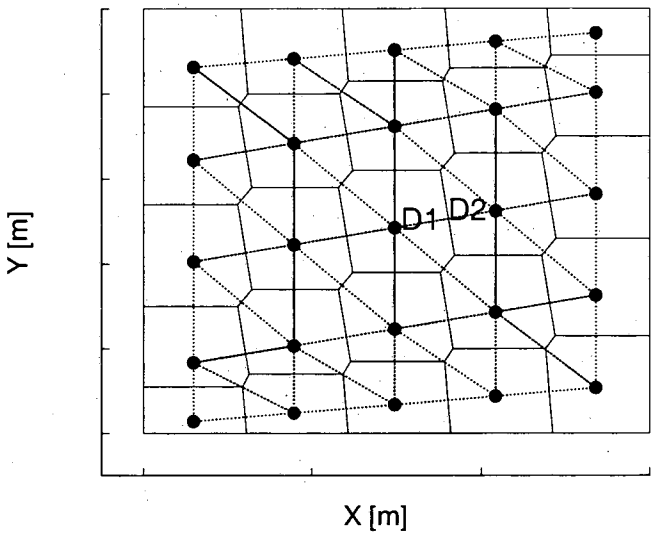


Figure 4.2. Example irregular mesh composed of Voronoi grid blocks and the definitions of grid block connections used in TOUGH2.

Figure 4.3 shows the 2-D model mesh, which has 1993 grid blocks. Most grid block dimensions are between 50 and 500 m, and several approach 1 km near the model boundaries. The finely discretized region near the center of the model corresponds to the area around the c-holes, which are used for multi-well pumping and tracer testing (Geldon, 1993; Geldon, 1996; Geldon *et al.*, 1997). Grid blocks are 50 x 50 m in this area in order to simulate pumping tests on the scale of hundreds of meters. Rectilinear grid blocks are used to define faults because they can represent a constant width and laterally continuous fault zone. The potential repository is located in the area of rectilinear grid blocks east of the Solitario Canyon Fault.

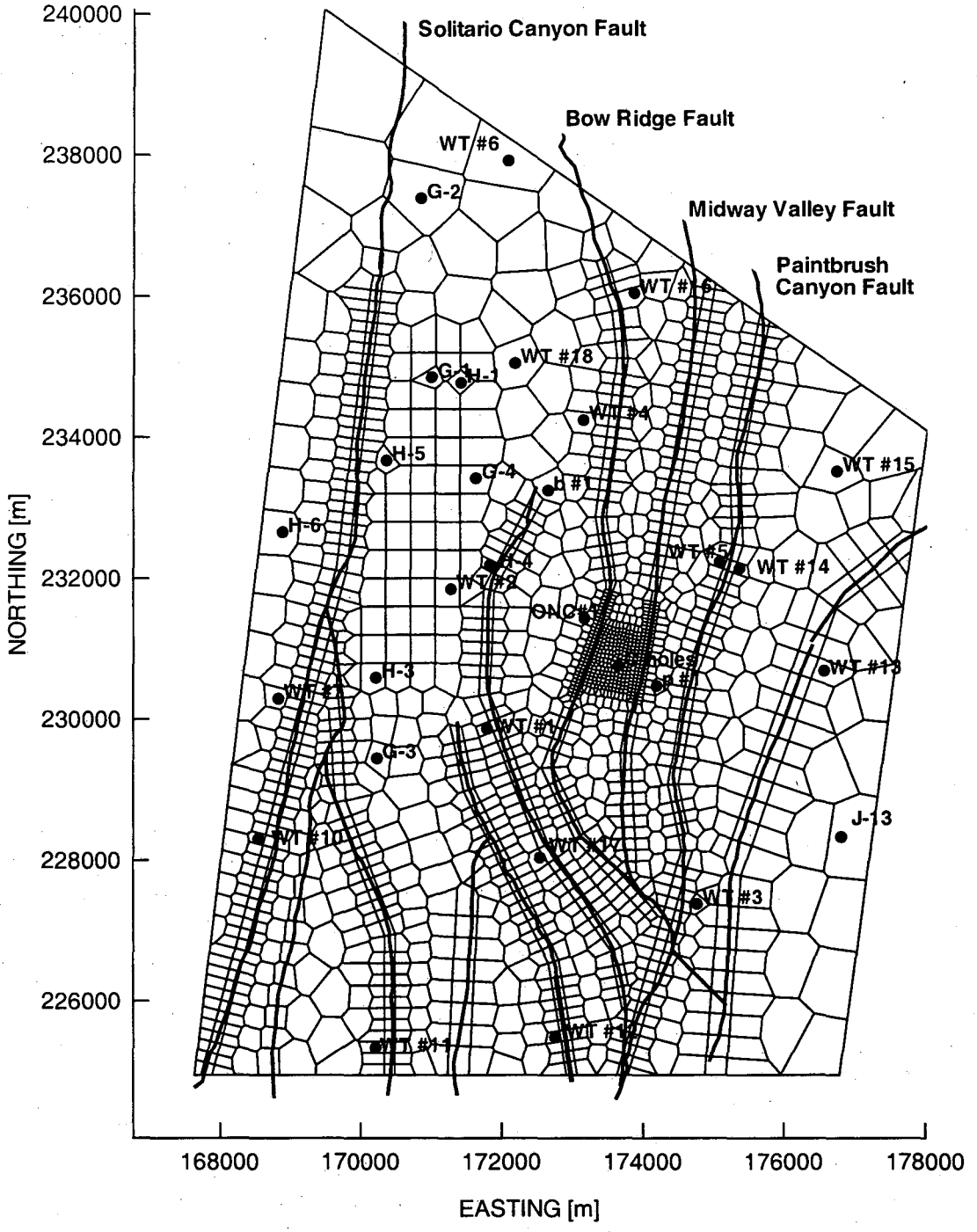


Figure 4.3. 2-D mesh of the saturated zone model.

## 4.5 Definition of Hydrogeologic Layers

The hydrogeologic model layers are subdivisions of geologic units. Elevation and isopach data for geologic units were taken from the 3-D geologic model of Clayton *et al.* (1997). The Lithic Ridge Tuff and lava flows and breccias are two geologic units included in the saturated zone model but not in the 3-D geologic model. Isopachs for these units were taken or created from other sources, as described below.

The geologic units were generally subdivided into three equal thickness layers to replicate vertical permeability variation within the units. In general, borehole flow surveys show that ambient and pumped water often flows from the more densely welded and fractured central intervals of the Crater Flat Group. Lithologic logs describe welding as ranging from nonwelded to densely welded. However, inspection of the flow and lithologic logs for boreholes that have both data sets shows that there are anomalies with regard to the flow zone/welding relationship. For example, flow is observed in the subsection of a particular unit in only one borehole. These anomalies may be real, due to local heterogeneities not representative of the entire unit, or due to misidentification of welding characteristics. In addition, not all permeable intervals will have signatures on a borehole flow log. The fraction of pumped water flowing from a permeable layer is proportional to the transmissivity of the layer relative to the composite transmissivity of the tested interval (Molz *et al.*, 1989). Therefore, most flow could be produced from a very high permeability layer even though other intervals have significant but lower permeabilities. Flow surveys were not performed in all boreholes. Given the above nuances, hydrogeologic layers were defined using a combination of lithologic and geophysical

logs, borehole flow surveys, some pumping and injection tests, and drilling history logs. Table 4.1 lists the sources of borehole and hydrogeologic data. Hydraulic tests are used sparingly because many results are poorly matched to analytic solutions.

Table 4.1 (following page). Sources of borehole geophysical and hydrologic data used to discretize geologic units and assign hydrogeologic properties.

| Bore-hole | Geologic units beneath WT | Lithology | Borehole flow logs | Temperature logs | Pumping tests | Injection tests | Matrix porosity | Matrix permeability | Fracture porosity |
|---|---|---|---|---|---|---|---|---|---|
| H-1 | Prow Pass Tuff - Older tuffs | 18 | 18 | 19 | 18 | 18 | 18 | 18 | na |
| H-3 | Tram Tuff - Lithic Ridge Tuff | 23 | 24 | 19 | 24 | 24 | na | na | na |
| H-4 | Prow Pass Tuff - Lithic Ridge Tuff | 9,25,26 | 26 | 19 | 26 | 9 | na | na | 9 |
| H-5 | Bullfrog Tuff - Lava | 4 | 4 | 19 | 17 | 17 | na | na | na |
| H-6 | Prow Pass Tuff - Lithic Ridge Tuff | 6,7 | 6 | 19 | 6 | 6 | na | na | na |
| G-1 | Topopah Spring Tuff - Older tuffs | 21 | na | 19 | na | na | na | na | na |
| G-2 | Topopah Spring Tuff - Lava and flow breccia | 16 | 27 | 19 | 15a | na | na | na | na |
| G-3 | Bullfrog Tuff- Older tuffs | 20 | na | 19 | na | na | 2 | 2 | na |
| G-4 | Prow Pass Tuff - Tram Tuff | 3 | 14 | 19 | 14 | 14 | 2,14 | 2 | na |
| b#1 | Calico Hills Formation - Lithic Ridge Tuff | 15 | 13 | 19 | 13 | 13 | 13 | 13 | na |
| c-holes | Calico Hills Formation - Tram Tuff | 10 | 11 | 11 | 11,12 | 11 | 10 | 10 | na |
| p#1 | Calico Hills Formation - Paleozoic carbonates | 5 | 8 | 19 | 8 | 8 | 1 | 1 | na |
| J-13 | Topopah Spring Tuff - Lithic Ridge Tuff | 22 | na | 19 | 22 | 22 | 22 | na | na |

references:

1. Anderson, 1991
2. Anderson, 1994
3. Bentley, 1984
4. Bentley *et al.*, 1983
5. Carr *et al.*, 1986
6. Craig and Reed, 1991
7. Craig *et al.*, 1983
8. Craig and Robison, 1984
9. Erickson and Waddell, 1985
10. Geldon, 1993
11. Geldon, 1996
12. Geldon *et al.*, 1997
13. Lahoud *et al.*, 1984
14. Lobmeyer, 1986
15. Lobmeyer *et al.*, 1983

15a. O'Brien, 1998

16. Maldonada and Koether, 1983
17. Robison and Craig, 1991
18. Rush *et al.*, 1984
19. Sass *et al.*, 1988
20. Scott and Castellanos, 1984
21. Spengler *et al.*, 1981
22. Thordarson, 1983
23. Thordarson *et al.*, 1984
24. Thordarson *et al.*, 1985
25. Whitfield *et al.*, 1984
26. Whitfield *et al.*, 1985
27. U.S. Geological Survey unpublished report, Heat-pulse flowmeter survey data from well use G-2, March 9, 1995.

### 4.5.1 Lithic Ridge Tuff

The Lithic Ridge Tuff is non- to partially welded with few fractures, and it has secondary alteration in the form of clay minerals and zeolites. The unit is present in borehole H-1, H-3, H-4, H-6, G-1, G-3, b#1, J-13, and p#1, and it has the same character in each borehole. This unit is the lower confining unit in the saturated zone model because of its low permeability and because the 21 m head increase in borehole p#1 was first observed in the older unnamed tuffs just beneath the Lithic Ridge Tuff (Craig and Robison, 1984).

The Lithic Ridge Tuff and its underlying bedded tuff (maximum thickness = 6 m) is fully penetrated in only five boreholes (G-1, G-2, G-3, H-1, and p#1), and the cumulative thickness in these holes is 297, 303, 204, 305, and 194 m, respectively. Carr *et al.* (1986) constructed an isopach using borehole data, outcrop measurements, and regional geologic relationships (Figure 4.4). Their isopach did not consider data from borehole p#1, but the map closely approximates the measured thickness.

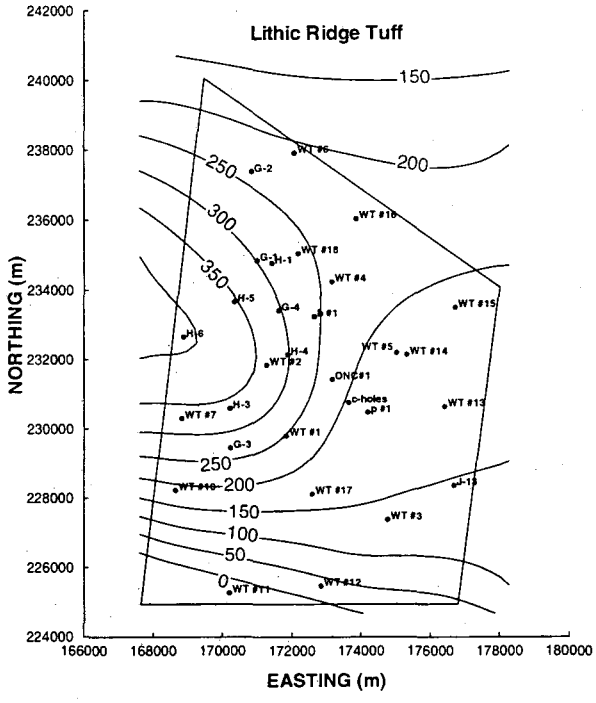


Figure 4.4. Isopach of the Lithic Ridge Tuff defined by Carr *et al.* (1986) within the model area.

### 4.5.2 Lava Flows and Breccias

A layer of lava flows and breccias were penetrated in boreholes H-1, H-6, G-1, G-2, and H-5. The observed thicknesses are 119, 253, 118, 24, and at least 176 m, respectively. The unit is present between the Lithic Ridge Tuff and Tram Tuff. Figure 4.5 is an isopach of the lava flows and breccias. The isopach is constructed using the measured thicknesses and a zero thickness constraint imposed by nearby boreholes H-3, H-4, b#1, and WT #6, in which the unit was not observed. The interpolated isopach honors the observation that the thickness in H-5 must be greater than 176 m, and it is also representative of a flow deposit in general. Most of the lava flows and breccias in each borehole are altered to clays and zeolites (Mattson, 1994). They therefore have low permeability.

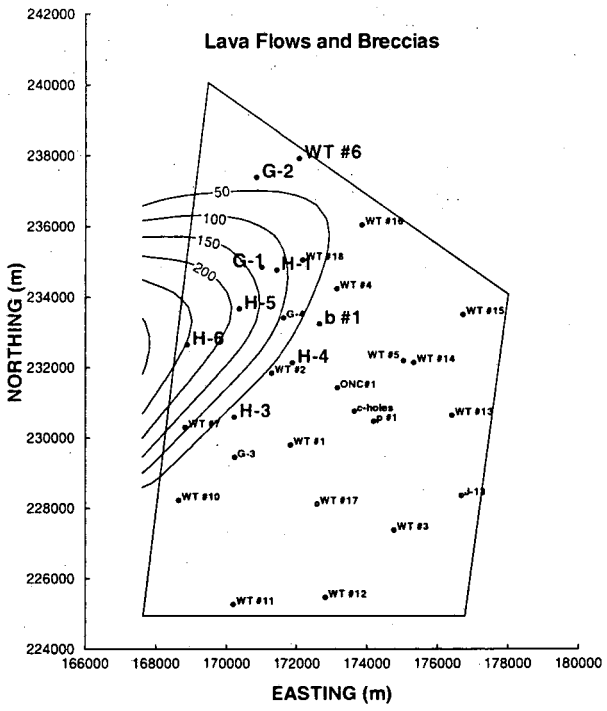


Figure 4.5. Isopach of lava flows and breccias. Control points for interpolation are data at H-1, H-6, G-1, G-2, and zero thicknesses assigned at boreholes H-3, H-4, b#1, and WT #6.

### 4.5.3 Lower Volcanic Confining Unit

The lava flows and breccias are low permeability layers like the Lithic Ridge Tuff. The two are therefore lumped into a single composite confining unit. The composite isopach is shown in Figure 4.6. The thinning of the unit to the east and south may be a significant hydrogeologic feature since the unit separates the lower volcanic aquifer and the Paleozoic units and older tuffs. The Lower Volcanic Confining Unit is modeled as a low permeability, homogeneous formation, but it is discretized into three model layers because it is thick.

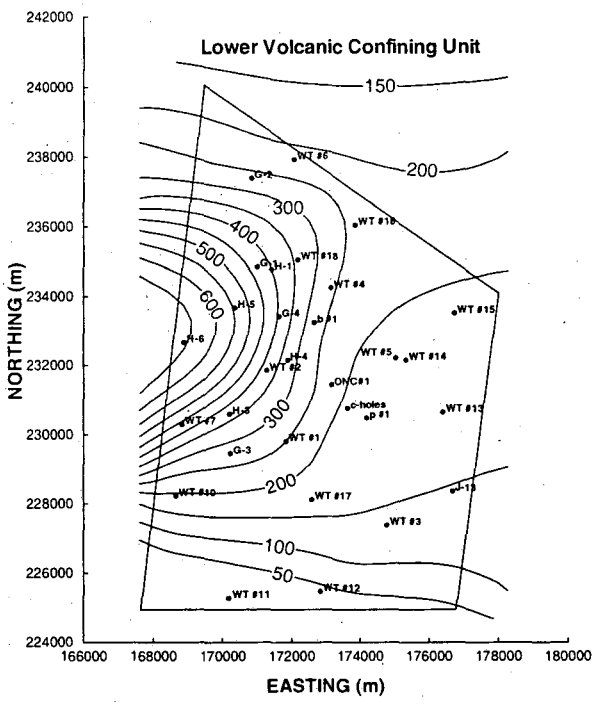


Figure 4.6. Isopach of Lower Volcanic Confining Unit.

The isopachs of the remaining units are taken from the ISM2.0 3-D geologic model. Figures 4.7 through 4.12 show the thicknesses of these units beneath the water table.

### 4.5.4 Crater Flat Group

Each unit in the Crater Flat Group is discretized into three layers to replicate the welding variation described earlier. A thin layer of bedded tuff underlies each of these units. These layers are considered part of the respective unit, except for the pre-Tram bedded tuff, which has distinctive properties compared to the Tram Tuff.

#### 4.5.4.1 Pre-Tram Bedded Tuff

The thickness of pre-Tram bedded tuff does not exceed 20 m in any of the saturated zone boreholes in the model except in G-2, where it is 50 m thick. Significant flow was observed at and near the pre-Tram bedded tuff and Lithic Ridge Tuff contact in boreholes H-3, H-4, and H-5. The contribution to total pumped flow was 30%, 12%, and 5%, respectively. In addition, a thin (2.5 m) densely welded sub-unit at the top of the Lithic Ridge Tuff was noted in G-2. The bedded tuff is represented by a single model layer.

#### 4.5.4.2 Tram Tuff

This unit is present in all of the deep saturated zone boreholes. A central, higher permeability layer is present in six boreholes. A different permeability structure is observed in five boreholes. The central portion of the Tram Tuff in H-6 produces 32% of pumped flow and has increased welding as compared to the surrounding layers. No flow survey was conducted in borehole G-1, but drilling history logs show that the maximum rate of penetration and mud loss in the Tram Tuff occurred near the central interval (MacDougall, date unknown). Furthermore, lithologic logs show that the greatest degree of welding is in the central portion of the unit. The lithologic log of G-2 only identifies two intervals, one as nonwelded and the other as partially welded. However, drilling history data shows that the maximum rate of penetration and mud loss occurred near the center (Maldonado and Koether, 1983). In G-3 the central interval is more densely welded and has a higher fracture density than the surrounding intervals. In borehole G-4 94% of pumped flow is produced from a 20 m interval near the center of the unit, where

there is increased fracturing. In borehole J-13 the upper and lower section of the Tram Tuff are zeolitized, whereas the central layer is partly welded and therefore more permeable. No borehole flow was observed in H-1 and welding is nearly constant throughout. The layering characteristics observed in other boreholes are different than those described above. In borehole H-5 the Tram Tuff is partially welded over most of the section and flow only occurs in the bedded tuff. In borehole H-3 the moderate to densely welded section is within the top half of the unit and 70% of the pumped water comes from this section. The moderate to densely welded section in H-4 is in the upper Tram Tuff, which is also where some of the pumped water originated. The Tram Tuff in borehole p#1 is mostly partially welded and no borehole flow was observed. The central Tram Tuff is not observable in the c-holes because a zone of tuff breccia intersects the unit. Geldon (1993) suggests that this altered zone is the Paintbrush Canyon Fault or a splay of the fault. The Tram Tuff is subdivided into three equal thickness layers to reflect the layered permeability structure.

#### 4.5.4.3 Bullfrog Tuff

The Bullfrog Tuff is present in all deep saturated zone boreholes except H-3. Lithologic and flow logs show that the central region of the Bullfrog Tuff is, in general, a moderate to densely welded interval from which most of the water is produced during pumping. Flow comes from the central interval in borehole H-1, H-6, b#1, and in the c-holes. No flow surveys were conducted in G-1, G-2, or G-3, but the unit in each borehole is more densely welded in the central section. In addition, fracture frequency in G-3 increases in the central Bullfrog Tuff. No flow was observed in p#1, but the central layer is more

densely welded than the surrounding layers. H-4 shows discrete flow in the upper quarter of the unit, but the upper and lower intervals are only partly welded, and caliper logs indicate more fracturing in the central interval. Borehole G-4 and J-13 do not show significant variations in welding within the unit. Finally, flow in H-5 occurs in the upper half of the unit, although it is only partially welded. In general, the central, higher permeability layer structure is present in most boreholes, and the unit is therefore subdivided into three hydrogeologic layers.

#### 4.5.4.4 Prow Pass Tuff

Lithologic and flow logs show that the central interval of the Prow Pass Tuff is, in general, more densely welded than the adjacent intervals and is the interval from which most of the water is produced during pumping. In borehole H-4, 19% of the total borehole flow comes from the central portion of the unit. The flow survey in p#1 shows that most of the total pumped water comes from the middle to upper portion of the unit. Flowing intervals generally occur near the center of the unit in other wells. The unit is therefore divided into three hydrologic layers.

### 4.5.5 Calico Hills Formation

The Calico Hills Formation is characterized as an upper confining unit that separates the high permeability Topopah Spring Formation and the Crater Flat Tuffs (Luckey *et al.*, 1996). In general, it has low permeability because the individual pyroclastic layers are generally nonwelded and zeolitized (Moyer and Geslin, 1995). The unit is present at the

water table in the northwestern section of the model where the large hydraulic gradient is observed (Figure 4.10). The formation is discretized into three layers.

### 4.5.6 Topopah Spring Tuff

The Topopah Spring Tuff defines the upper volcanic aquifer, except near its base where vitric sub-zones and bedded tuff are present. This layer is zeolitized and of low permeability, and it is modeled as a single layer. A relatively thin section of this unit is present on the eastern side of the model (Figure 4.11) The remaining sections of the unit are generally densely welded and have numerous lithophysal horizons, both of which make it a high permeability unit. It resides mainly in the unsaturated zone and dips below the water table only to the east. Here it is a productive aquifer where borehole J-13 is routinely pumped for the Nevada Test Site. The unit is subdivided into four layers, although it could have been represented by two layers given its relative absence in the model.

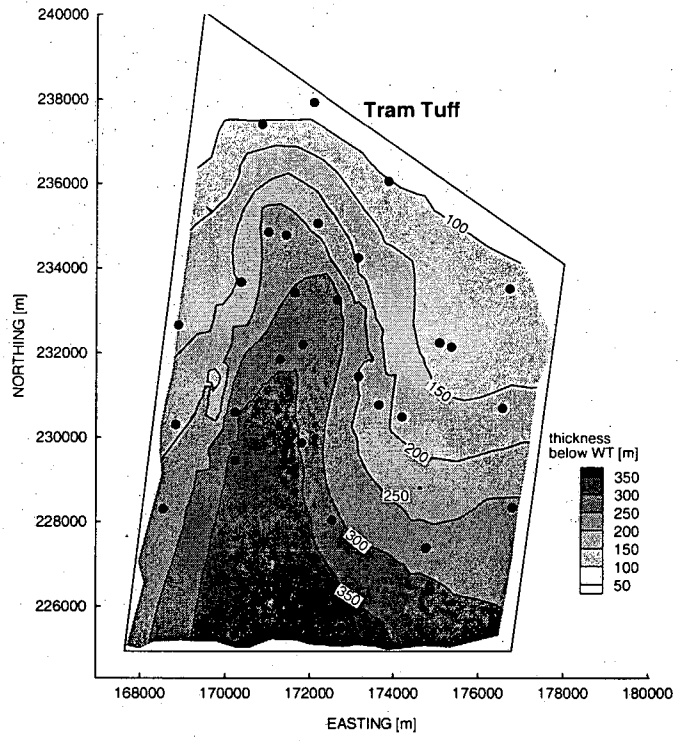


Figure 4.7. Thickness of the Tram Tuff beneath the water table.

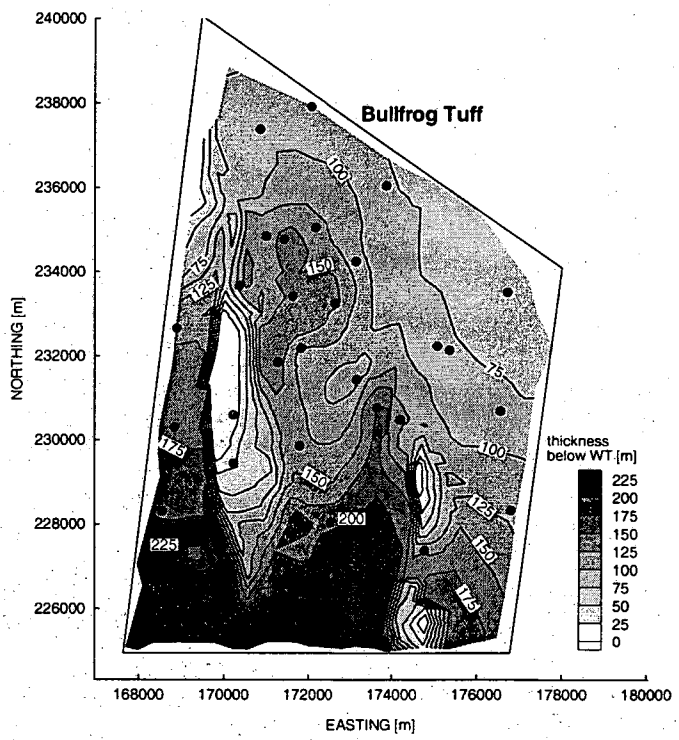


Figure 4.8. Thickness of the Bullfrog Tuff beneath the water table.

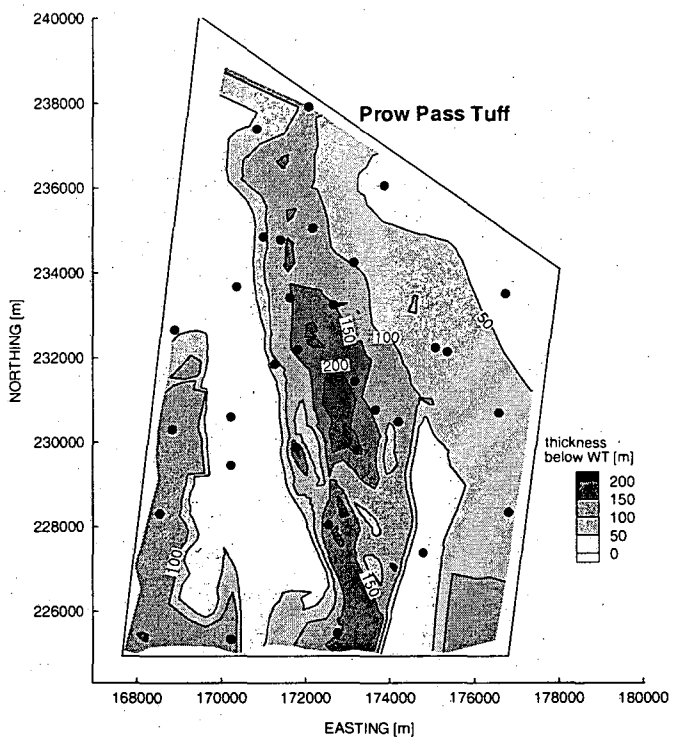


Figure 4.9. Thickness of the Prow Pass Tuff beneath the water table.

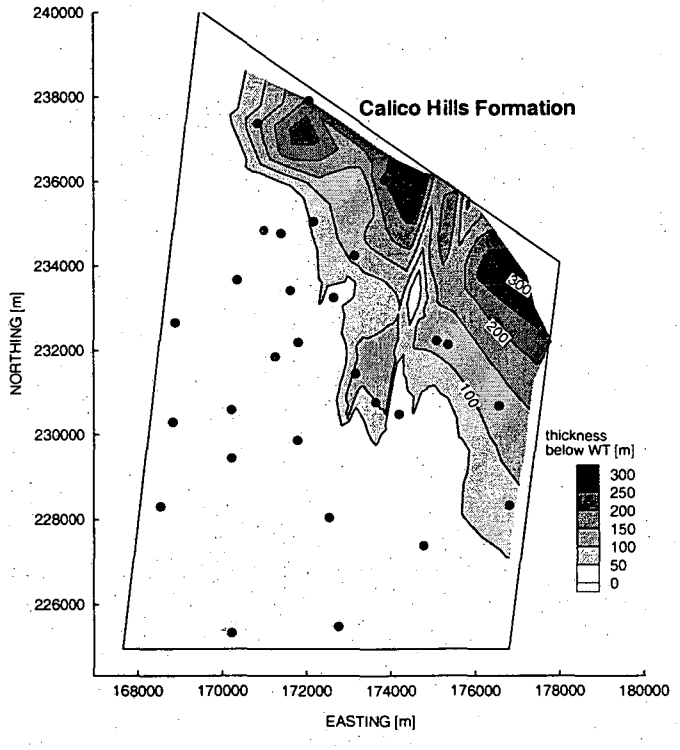


Figure 4.10. Thickness of the Calico Hills Formation beneath the water table.

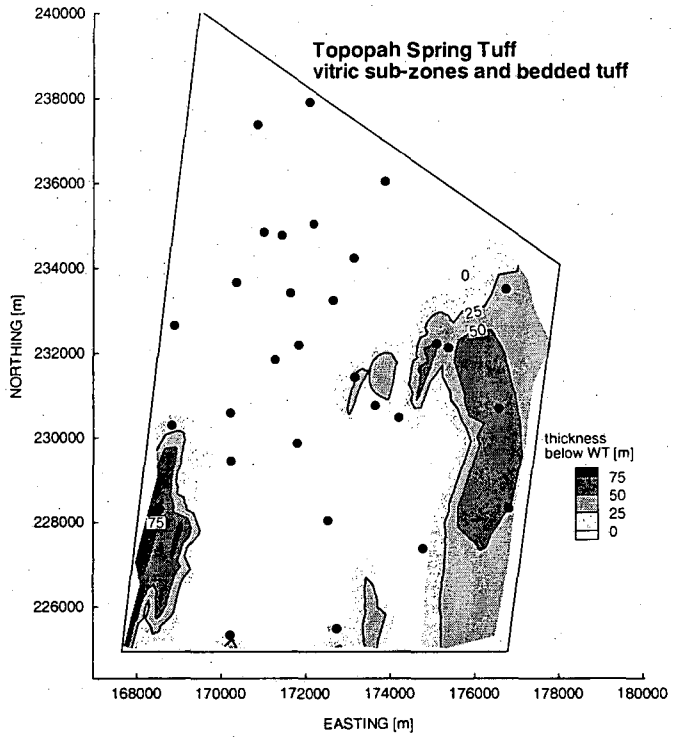


Figure 4.11. Thickness of the vitric sub-zones and bedded tuff of the Topopah Spring Tuff beneath the water table.

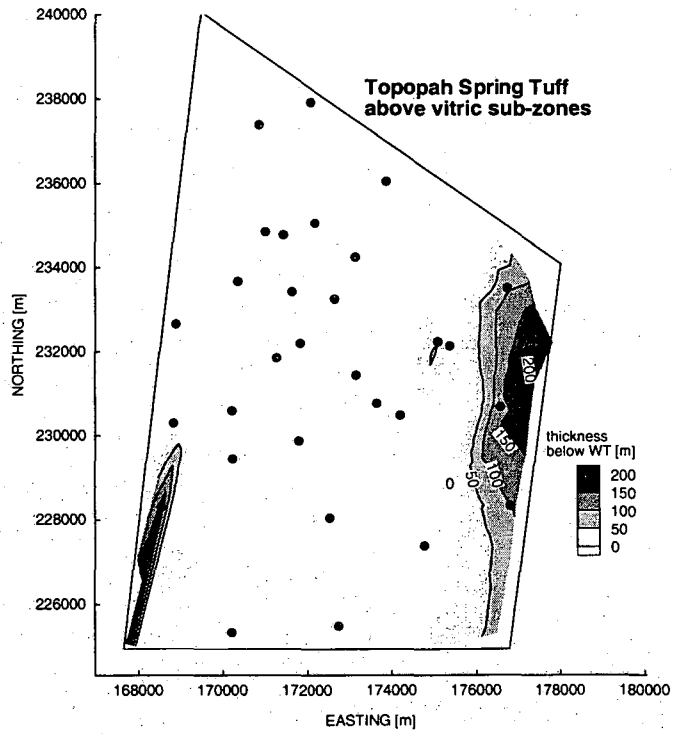


Figure 4.12. Thickness of the densely welded Topopah Spring Tuff beneath the water table.

## 4.6 Vertical Concatenation of Individual Layers

The 23 mesh layers were stacked and the vertical connections within a grid block column were computed based on the thicknesses of individual layers. The connection distances are formulated in the same manner as the 2-D connection scheme: each connection, D1 and D2, represents the distance from each node to the interface separating the layers. The vertical connection interface area within a grid block column is equal to the 2-D area of the grid block.

Due to the scheme used to facilitate discretization of faults (described below), there are 23 layers in every grid block column even though not all units are present beneath the water table everywhere. The grid blocks of hydrogeologic layers that are not beneath the water table have thicknesses ranging from 1 and 3 m, and these grid blocks are assigned the rock property of the unit that is present at the water table.

## 4.7 Selection and Representation of Faults

As described in Section 2.8, north-trending normal faults are the dominant faults because of their large displacement and laterally continuity. The strike-slip and intrablock faults are considered secondary features because of their scarcity and relatively small displacement. Therefore, only the block bounding faults are modeled explicitly. The 3-D geologic model of Clayton *et al.* (1997) defines block-bounding faults as those which have more than 30 m of vertical displacement and a 2 mile (3200 m) or longer surface trace (Clayton *et al.*, 1997). These include the Solitario Canyon Fault, Iron Ridge Fault, Dune Wash Fault, Bow Ridge Fault, Midway Valley Fault, Paintbrush Canyon Fault, and

Forty Mile Wash Fault. The model is discretized to account for these faults and four others located near the southern boundary of the model (Figure 4.3). The two parallel faults of the Solitario Canyon Fault are represented as a single fault which accounts for the total offset across the two faults. Faults are modeled as vertical features.

### 4.7.1 Fault Discretization

In the horizontal plane a fault is modeled with a continuous band of equal-width grid blocks (Figure 4.3). This scheme preserves the natural continuity of faults and enables modeling of a fault with no internal zone (displacement-only fault), or one that also has a fault zone. Fault grid blocks are located along their surface traces defined in the 3-D geologic model. Fault grid blocks are approximately 150 x 150 m, except along Forty Mile Wash Fault and the fault east of the Iron Ridge Fault, where they are approximately 300 x 300 m. The lateral dimensions of fault grid blocks do not represent the actual width of faults but rather the width over which fault properties are averaged. Fault displacement varies along strike and displacement is constant with depth. Figure 4.13 shows the displacement along modeled faults.

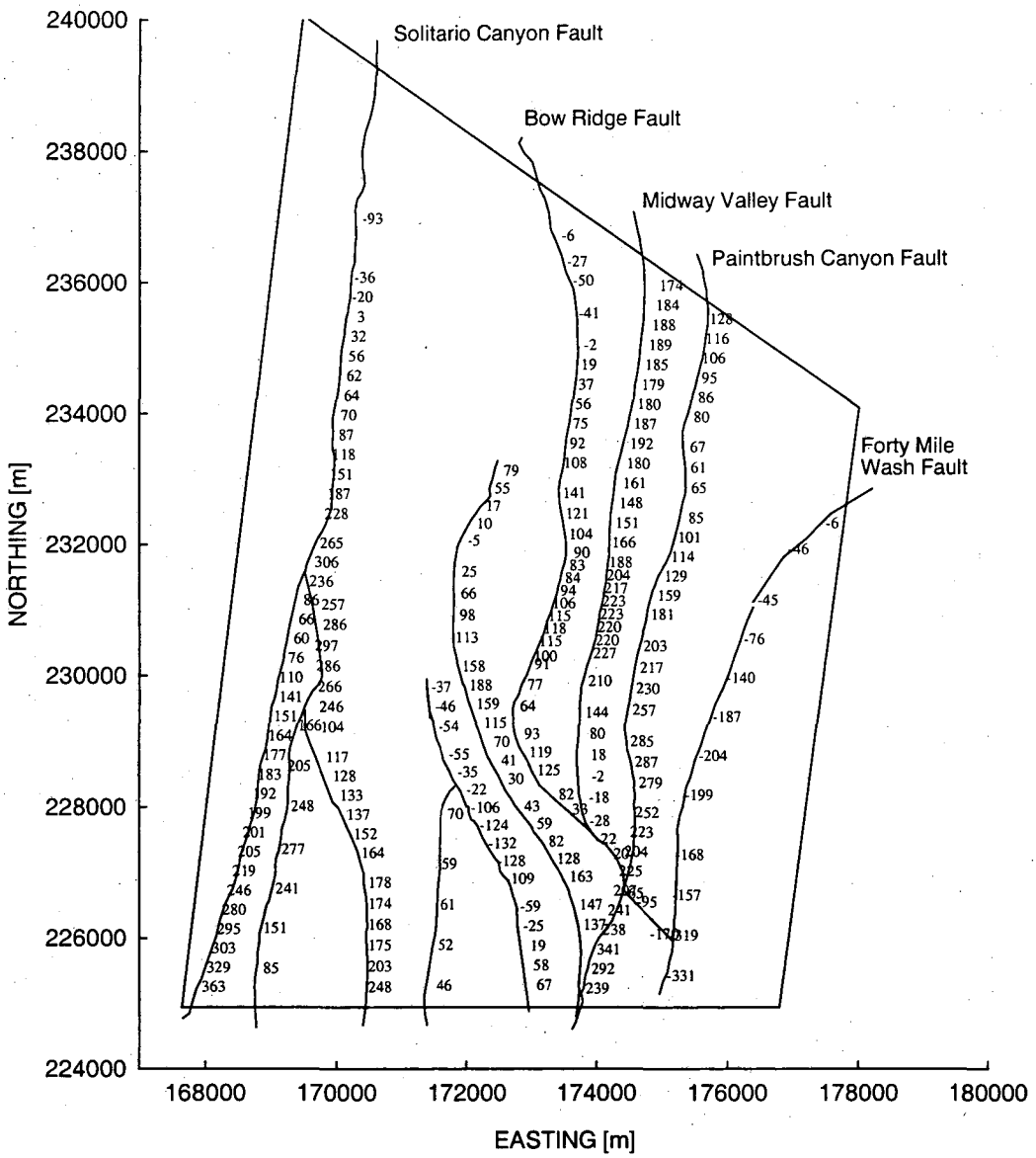


Figure 4.13. Fault displacement in the saturated zone model (in meters). Positive values represent down-to-the-west displacement. Negative values represent down-to-the-east displacement.

Figure 4.14 shows how grid blocks at faults are discretized to account for fault displacement. Fault grid blocks are positioned such that the lateral interface area between two grid block layers on either side of the fault is represented properly. The height of an individual fault grid block is equal to the vertical distance over which the adjacent layers are displaced, and the rock properties of that grid block correspond to the rock type on one side of the fault. A fault zone is represented by setting the permeability of the fault grid block to the desired value.

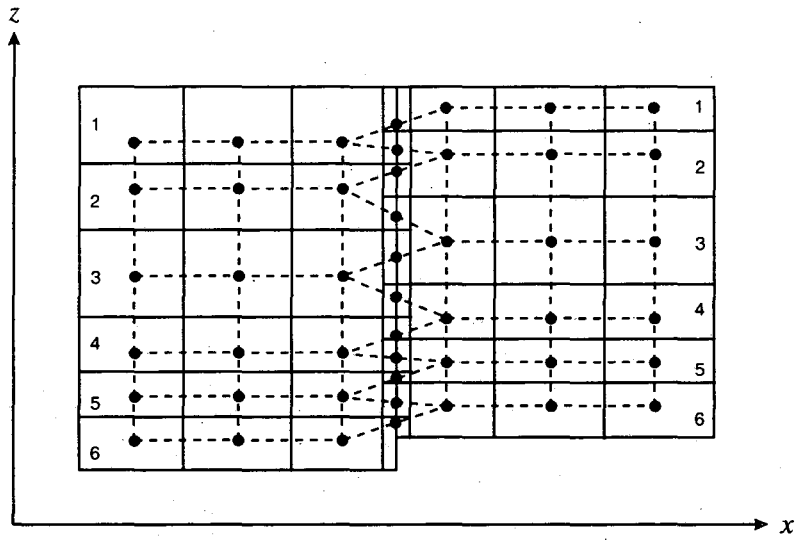


Figure 4.14. Vertical discretization of fault grid blocks. Dots are grid block nodes and dashed lines are grid block connections.

Besides the explicit representation of faults, a unique feature of the model is the representation of dipping layers with a single layer of grid blocks. This reduces the number of grid blocks needed to model a dipping layer, and it also accurately represents the continuity of a layer. A traditional finite-difference mesh oriented in the horizontal plane would require many more grid blocks to represent a dipping layer. In order to

model the dipping layers and fault displacement, grid block connections across faults and within layers in the horizontal plane are not orthogonal to the grid block interface area. Deviations are generally less than 10 degrees, which does not impart a noticeable error in the flow calculation.

## 4.8 Comparison to Geologic Model

The accurate representation of geologic structure in the saturated zone model is illustrated in Figures 4.15 through 4.17. Figure 4.15 shows the distribution of rock units at the top of the saturated zone model, and Figure 4.16 is a perspective view of the 3-D geologic model, for comparison. There are some discrepancies between the two figures because the surface shown for the geologic model is at a constant elevation of 706 m, whereas the water table in the flow model ranges from 728 m to more than a 1200 m in the northwest corner.

Figure 4.17a is a cross-section through the flow model along A-A', as shown in Figure 4.16, and Figure 4.17b is the same cross-section through the 3-D geologic model. The layer thicknesses, fault displacements, and intersection of different units at the water table are replicated. Although discrepancies exist, in particular due to assumption of vertical faults, the overall character of the faulted structure is replicated.

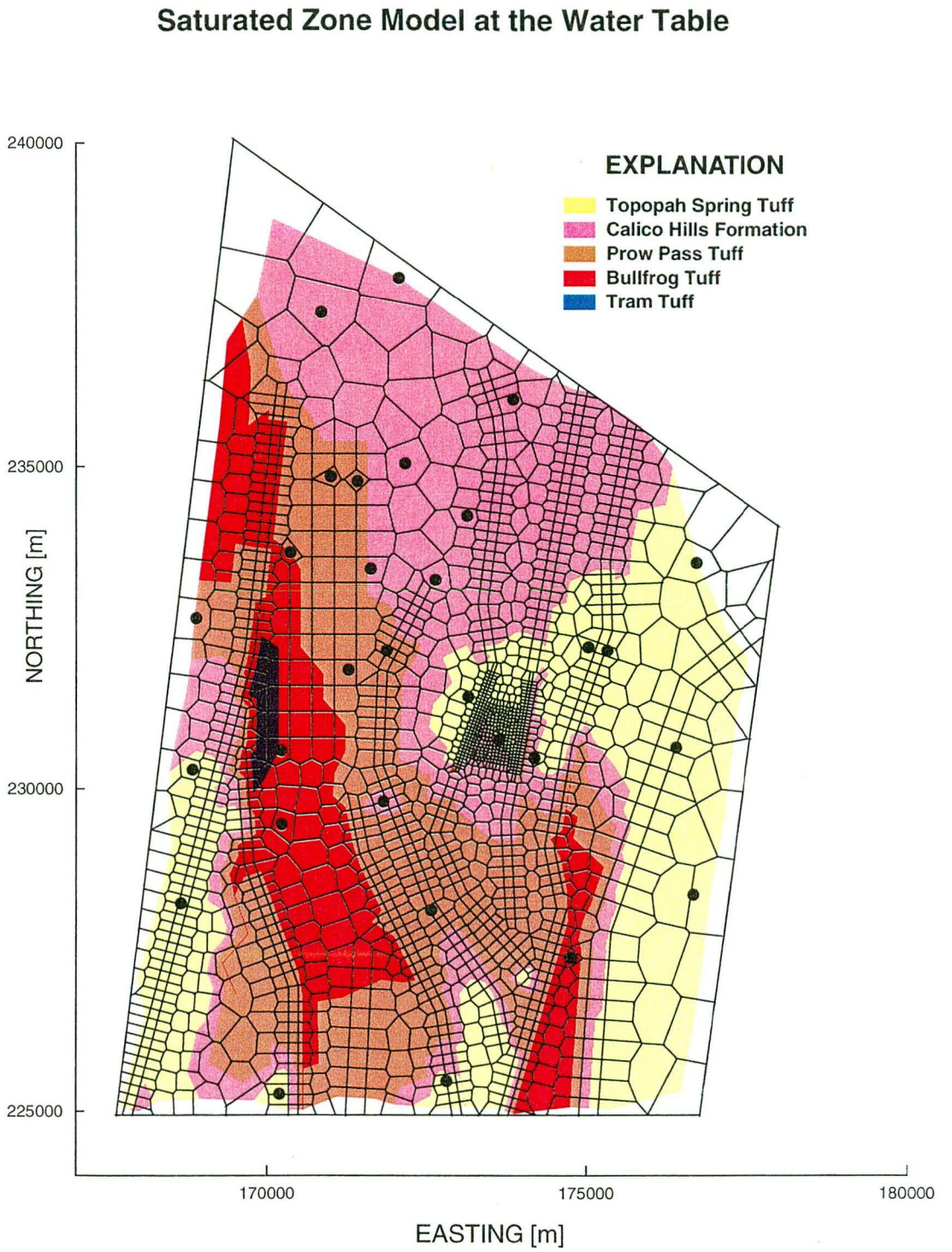


Figure 4.15. Distribution of rock units at the top of the saturated zone model.

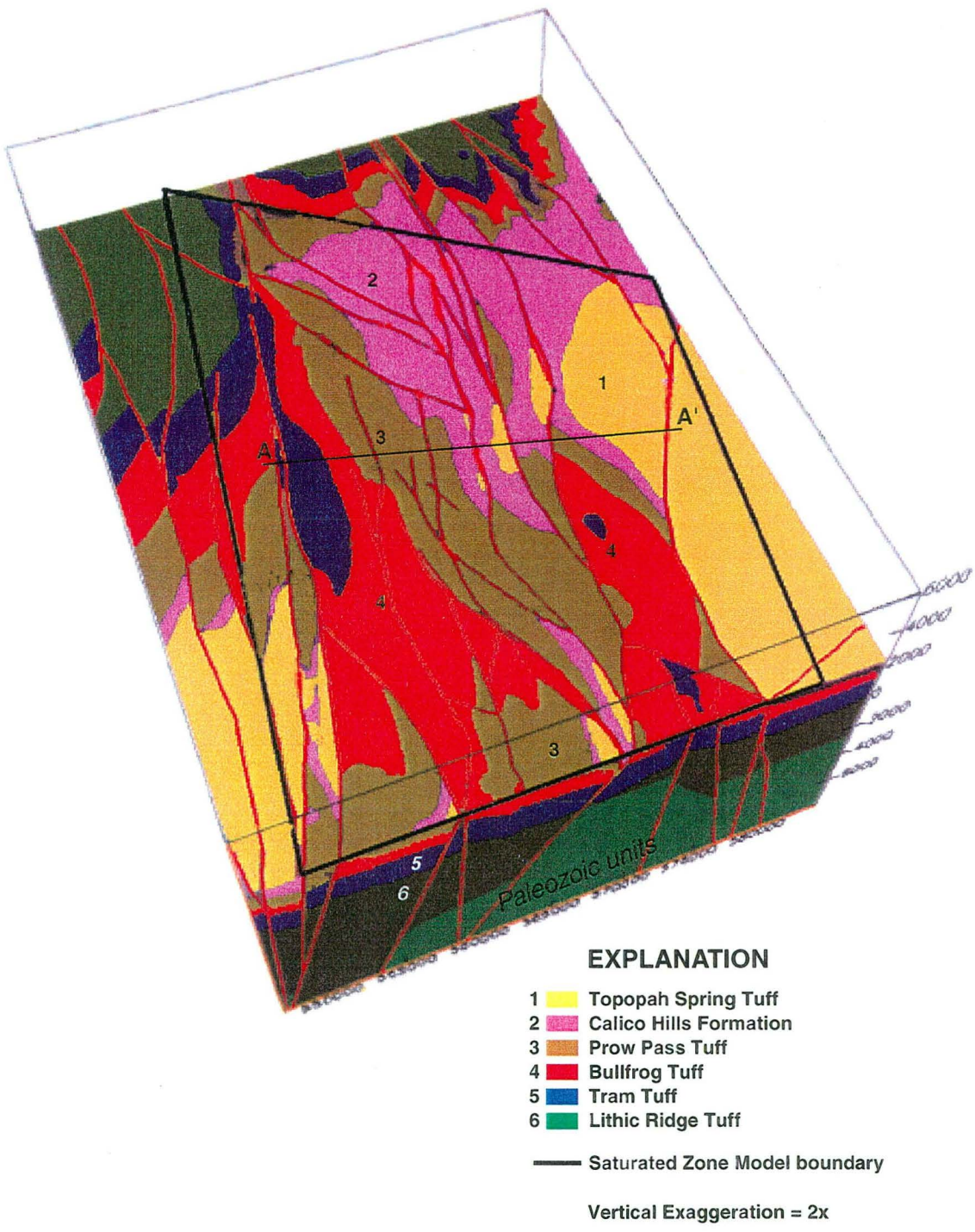


Figure 4.16. Horizontal slice through ISM2.0: A 3D Geologic Framework and Integrated Site Model of Yucca Mountain (Clayton *et al.*, 1997).

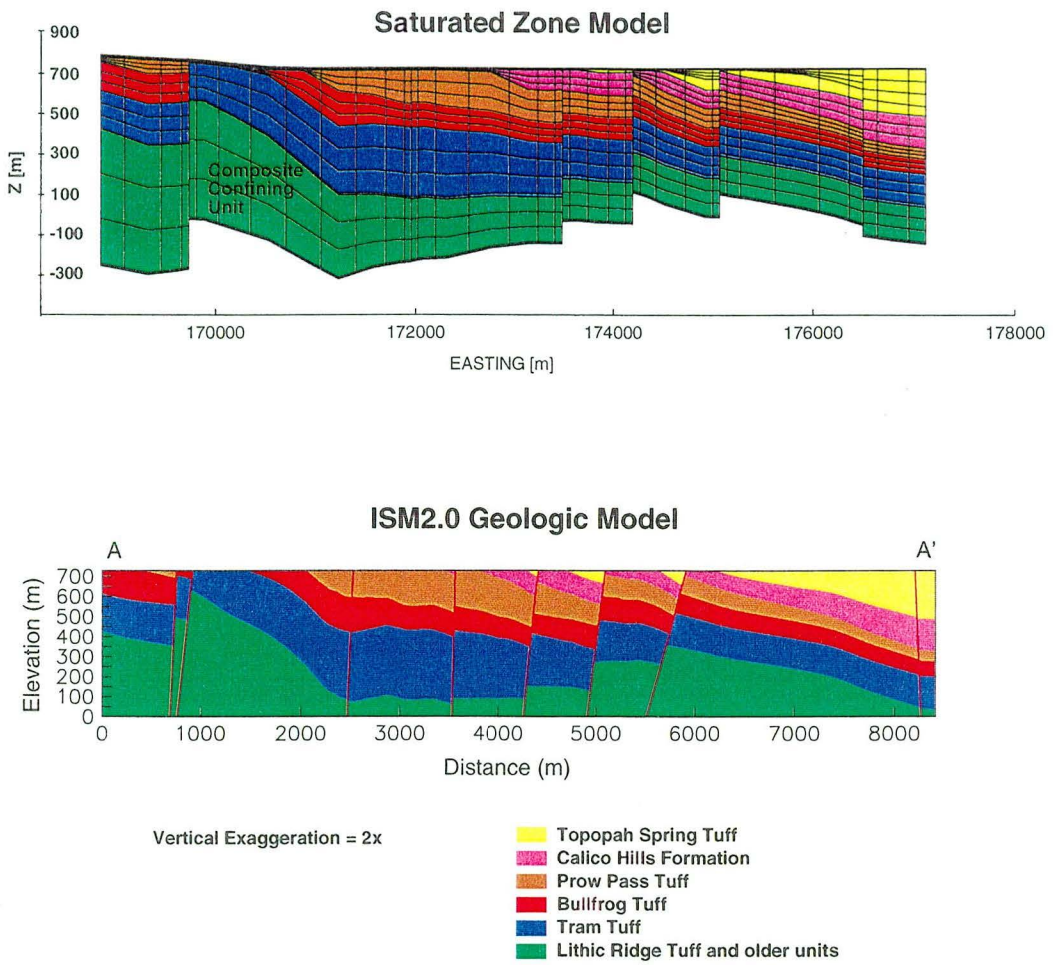


Figure 4.17. a) Cross-section along A-A' in the saturated zone model; b) geologic section along A-A' through ISM2.0: A 3D Geologic Framework and Integrated Site Model of Yucca Mountain (Clayton *et al.*, 1997).

# 5. Hydrogeologic and Thermal Properties

## 5.1 Permeability

As described in Section 2.5, the c-holes provide the most reliable permeability estimates of units in the Crater Flat Group. These units have been characterized in detail using borehole geophysical logs and pumping and injection tests. Pumping tests with multiple observation boreholes have been conducted as well (Geldon, 1993, 1996). In order to use the most data available, the hydraulic tests conducted in the 1980's were carefully reviewed to check the data quality and goodness-of-fit of analytic solutions. The permeabilities assigned to the units are either reported values or they were calculated using the reported transmissivity of the entire interval multiplied by the percent of flow from the unit in question, divided by the unit thickness.

In comparison to the saturated zone, hydraulic testing in the unsaturated zone has been extensive. Some of the unsaturated zone test results are therefore used to define permeability of rock layers and faults in the saturated zone, where appropriate.

### 5.1.1 Upper Volcanic Aquifer

Except for the basal vitric sub-zones, the Topopah Spring Tuff is a high permeability and relatively homogeneous unit. J-13 is the only borehole at the mountain where this unit is beneath the water table. The permeability determined from a pumping test is $10^{-12}$ $m^2$ (Thordarson, 1983). This value agrees with permeabilities determined by calibration of an unsaturated zone model to liquid saturation profiles (Bodvarsson *et al.*, 1997). The calibrated values for six different horizons in the upper lithophysal zones range from

$1.2x10^{-12}$ to $8.5x10^{-13}$ $m^2$. The mean fracture permeability determined from air injection tests in 4 unsaturated zone boreholes is $1.3x10^{-12}$ $m^2$, with a standard deviation less than 1 order of magnitude (LeCain, 1997). This unit is therefore modeled with a constant and homogeneous permeability of $10^{-12}$ $m^2$.

### 5.1.2 Upper Volcanic Confining Unit

The Upper Volcanic Confining Unit consists of the basal vitric sub-zones of the Topopah Spring Tuff and the Calico Hills Formation. Calibration of an unsaturated zone model to liquid saturation profiles yielded a minimum permeability of $2.5x10^{-15}$ $m^2$ for the Calico Hills Formation (Bodvarsson *et al.*, 1997), and the permeability calculated from a pumping test in G-2 is $4x10^{-14}$ $m^2$ (O'Brien, 1998). Tests at the c-holes yielded a permeability of $2x10^{-13}$ $m^2$, although most flow comes from a discrete fractured zone at the base of the Calico Hills Formation (Geldon, 1996). This value defined the maximum permeability considered for calibration. The minimum permeability considered for model calibration was $10^{-15}$ $m^2$.

### 5.1.3 Lower Volcanic Aquifer

Luckey *et al.* (1996) report a permeability between $5x10^{-13}$ and $10^{-12}$ $m^2$ for the Lower Volcanic Aquifer (Prow Pass, Bullfrog, and Tram Tuff). These values are representative of a composite permeability for this aquifer. Since Geldon (1996) reports that the permeability of the Bullfrog Tuff is $1.4x10^{-11}$ $m^2$, lower permeabilities must also be present. In addition, the nonwelded layers within each unit have a lower permeability

than the reported permeability for each individual unit because the densely welded zones are more permeable.

Pumping tests at the c-holes suggest that the high permeability layers of the Crater Flat Tuff are continuous at least to a scale of several kilometers, since drawdown transients in the c-holes and in boreholes UE-25 ONC-1, H-4, WT #3, and WT #14, located as far as 3.5 km from the c-holes, yielded transmissivities with the same order of magnitude (Geldon *et al.*, 1997). This suggests that assignment of a uniform permeability for these layers may be reasonable, at least on that scale.

The calculated permeability of the Prow Pass Tuff in H-1 and G-4 is approximately $10^{-12}$ $m^2$ (Lobmeyer, 1986; Rush *et al.*, 1984). Tests in the c-holes yielded a permeability of $4x10^{-12}$ $m^2$ (Geldon, 1996). This value is representative of the central welded zone where most flow is pumped. Therefore, the range of permeabilities of the Prow Pass Tuff considered in the model was $10^{-14}$ to $10^{-12}$ $m^2$.

The permeability of the Bullfrog Tuff in borehole H-5 and H-6 is $2x10^{-13}$ $m^2$ (Craig and Reed, 1991; Robison and Craig, 1991) and $4x10^{-11}$ $m^2$ in the c-holes (Geldon, 1996). Therefore, a permeability range from $10^{-13}$ to $10^{-11}$ $m^2$ was considered for this unit.

The permeability of the Tram Tuff in borehole H-3, H-5, H-6, and p#1 ranges from $2x10^{-15}$ to $7x10^{-13}$ $m^2$ (Craig and Reed, 1991; Craig and Robison, 1984; Robison and Craig, 1991; Thordarson *et al.*, 1985). However, the permeability in H-1 is $3x10^{-17}$ $m^2$

(Rush *et al.*, 1984). This extreme value results from the absence of fractures in this borehole. Therefore, a permeability range from $10^{-15}$ to $10^{-13}$ $m^2$ was considered for this unit.

### 5.1.4 Lower Volcanic Confining Unit

Packer-injection test data that are matched well with analytic solutions yield permeabilities from less than $10^{-16}$ $m^2$ to $2x10^{-18}$ $m^2$ for the Lithic Ridge Tuff (Rush *et al.*, 1984; Thordarson *et al.*, 1985). Matrix permeability of a flow breccia core sample from borehole H-1 was $10^{-18}$ $m^2$, and a packer injection test yielded a permeability of $3x10^{-18}$ $m^2$ (Rush *et al.*, 1984). Thus, the composite confining unit was modeled as a homogeneous formation with a permeability of $10^{-17}$ $m^2$.

## 5.2 Porosity

Simulations described in this work are steady-state, and the flow visualization tracer is used to define flow paths, not a solute plume. Therefore, simulation results are independent of porosity. By using a homogeneous porosity, the flow visualization tracer is representative of flow paths.

## 5.3 Thermal Conductivity

The thermal conductivities assigned to the model layers are based on laboratory tests on rocks cores (Brodsky *et al.*, 1997; Sass *et al.*, 1988), and they range from 1.22 to 2.1 $J\,m^{-1}\,^{\circ}C^{-1}s^{-1}$ (Table 5.1).

Table 5.1. Ranges of hydrogeologic properties used in simulations.

| ISM2.O geologic unit (Clayton *et al*., 1997) | | SZ model layer | $k$ [$m^2$] | $K$ [$J\ m^{-1}\ ^oC^{-1}\ s^{-1}$] | porosity $\phi$ |
|---|---|---|---|---|---|
| | | top | | | |
| Topopah xl-rich nonlithophysal zone | Tptrn | | | | |
| Topopah xl-rich lithophysal zone | Tptrl | tptrn | $10^{-12}$ (1,6) | 1.8 (2,11) | $2.8 \times 10^{-4}$ |
| Topopah lithic rich member | Tptf | | | | (1) |
| Topopah upper lithophysal zone | Tptpul | | | | |
| Topopah middle nonlithophysal zone | Tptpmn | tpmn1 | $10^{-12}$ (1,6) | | |
| Topopah lower lithophysal zone | Tptpll | tpmn2 | $10^{-12}$ (1,6) | 2.1 (2,11) | $2.8 \times 10^{-4}$ |
| Topopah lower nonlithophysal zone | Tptpln | tpmn3 | $10^{-12}$ (1,6) | | (1) |
| Topopah lower densely welded vitric sub-zone | Tptpv3 | | | | |
| Topopah non-partly-welded vitric sub-zones | Tptpv1-2 | tptv3 | $2 \times 10^{-14}$ (1) | 2.1 (2,11) | $2.8 \times 10^{-4}$ |
| pre-Topopah Spring Tuff bedded tuff | Tpbt1 | | | | (1) |
| Calico Hills Formation undifferentiated | Tac | calc1 | | | |
| pre-Calico Hills Formation bedded tuff | Tacbt | calc2 | $10^{-15}$-$2 \times 10^{-13}$ | 1.22 (2,11) | $2.8 \times 10^{-4}$ |
| | Tacbt | calc3 | | | |
| Prow Pass Tuff upper nonwelded zone | Tcp [unw] | prow1 | | | |
| Prow Pass Tuff welded zone | Tcp [w] | prow2 | $10^{-14}$-$10^{-12}$ | 1.42 (2,11) | $2.8 \times 10^{-4}$ |
| Prow Pass Tuff lower nonwelded zone | Tcp [lnw] | prow3 | (5,7,8,10) | | |
| pre-Prow Pass Tuff bedded tuff | Tcp [bt] | | | | |
| Bullfrog Tuff upper nonwelded zone | Tcb [unw] | bull1 | | | |
| Bullfrog Tuff welded zone | Tcb [w] | bull2 | $10^{-13}$-$10^{-11}$ | 1.63 (2,11) | $2.8 \times 10^{-4}$ |
| Bullfrog Tuff lower nonwelded zone | Tcb [lnw] | bull3 | (3,5,8,9,10) | | |
| pre-Bullfrog Tuff bedded tuff | Tcb [bt] | | | | |
| | | tram1 | | | |
| Tram Tuff undifferentiated | Tct | tram2 | $10^{-15}$-$10^{-13}$ | 1.72 (2,11) | $2.8 \times 10^{-4}$ |
| | | tram3 | (3,9,10,12) | | |
| pre-Tram Tuff bedded tuff | Tct [bt] | tram4 | | | |
| Composite Confining Unit | | lith1 | $10^{-17}$ (10,12) | | |
| (defined in this report) | | lith2 | $10^{-17}$ (10,12) | 1.84 (2,11) | $2.8 \times 10^{-4}$ |
| | | lith3 | $10^{-17}$ (10,12) | | |
| | | bottom | | | |

References


1. Bodvarsson *et al*., 1997
2. Brodsky *et al*., 1997
3. Craig and Reed, 1991
4. Craig and Robison, 1984
5. Geldon, 1996
6. LeCain, 1997
7. Lobmeyer, 1986
8. Luckey *et al*., 1996
9. Robison and Craig, 1991
10. Rush *et al*., 1984
11. Sass *et al*., 1988
12. Thordarson *et al*., 1985

# 6. 2-D Simulations

## 6.1 Introduction

Simulations of steady-state flow in a cross-section of the full model were performed as an initial step to gain insight into the potential role of hydrogeologic features on fluid and heat flow. In particular, the 2-D simulations were used to examine the possible mechanisms that can produce fluid upwelling, the observed head gradients and water table temperatures. They are also used to elucidate the potential flow pathways and spreading of potential contaminants by mechanical dispersion. These simulations considered (1) displacement-only faults, (2) high permeability faults, and (3) low permeability faults. In addition, the effects of hydrogeologic structure on water table temperatures was examined. The calibrated model for each case revealed which fault and formation properties can account for the observed head data, thereby constraining the range of properties that needed to be considered for the 3-D simulations.

## 6.2 2-D Model

The 2-D model is a vertical cross-section oriented approximately perpendicular to the water table contours near the center of the 3-D model (Figure 4.17). A continuous band of grid blocks along A-A' does not exist. Therefore, the 2-D model cross-section is defined by a series of connected grid blocks that are close to A-A'. The vertical and horizontal connection areas, connection distances, and grid block volumes of these grid blocks as defined in the full 3-D model are recalculated such that they represent a 2-D model projection of A-A' onto the x-z plane. The projected model has a constant thickness of 150 m. Figure 4.17a shows the 2-D model.

## 6.3 Simulation Approach

### 6.3.1 General

Steady-state and isothermal flow was simulated. Simulations of the effects of all fault types followed the same approach: permeabilities of hydrogeologic layers and/or faults were modified by a trial-and-error process until a best-fit calibration to the measured heads in boreholes H-4 and WT #14, and to the water table gradient in general, was achieved. The total flux through the model was also compared to estimated fluxes as a second calibration check.

The calibrated formation properties are non-unique. Therefore, in comparing two different fault types, a different layer permeability distribution could be used in each case. In order to examine the effects of faults only, the approach taken was to first calibrate the displacement-only faults model to define layer permeabilities, and then to use these values for the initial distribution when calibrating the high- and low-permeability fault models.

### 6.3.2 Flow Visualization Tracer

The flow field was examined using the EOS7 module for TOUGH2 (Pruess, 1991b). The module is designed for simulation of single- or multi-phase flow of brine, water, and gas. It is used here to simulate single-phase transport of an isothermal water-brine mixture. The brine is assigned the same density and viscosity as water. As a result, the brine effectively acts as a conservative tracer, and since EOS7 does not include a description of diffusion, the simulated tracer distribution results from advection and numerical

dispersion only. The tracer is referred to as a flow visualization tracer in this work. For a particular simulation, a constant tracer mass fraction ($X_{tracer}$) of 1.0 is specified at a point(s) in a steady-state flow field and the tracer distribution after some time is used to infer flow pathways and the implied mechanical dispersion due to the flow heterogeneity. The flow visualization tracer does not represent a solute plume. Some of the tracer spreading is due to numerical dispersion. However, assuming the numerical dispersion is roughly the same for each simulation, the relative differences between different flow fields can be examined.

Figure 6.1 is an example flow visualization tracer distribution using a model that has a predictable flow field. The left and right sides are constant head boundaries and the permeability is homogeneous and isotropic. The flow visualization tracer shows the general flow pathway.

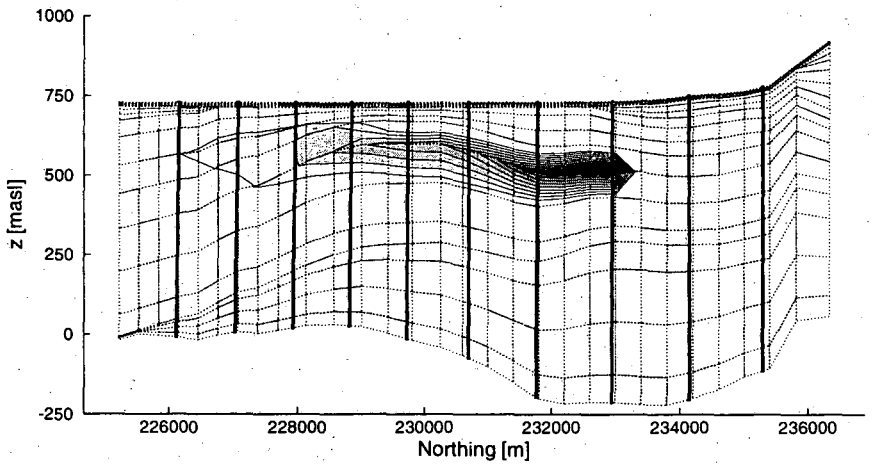


Figure 6.1. Example flow visualization tracer in a steady-state flow field. Vertical exaggeration = 4x.

## 6.4 Boundary Conditions

### 6.4.1 Hydraulic Head

The western and eastern sides of the model are constant head boundaries. The western-most column of grid blocks corresponds to well H-6 and was assigned a head of 776 m. The measured head in this well at the water table is 776.02 m and is 775.94 m 225 m beneath the water table (Table 2.2). This head difference is negligible with respect to down-gradient calibration since the head immediately east of the Solitario Canyon Fault is 45 m lower. A constant head of 729 m is assigned to the eastern column. This is an approximate head based on interpolation of measured heads near the eastern boundary.

### 6.4.2 Flux

Figure 6.2 shows the surface infiltration map for the Yucca Mountain area (Flint *et al.*, 1996 (unpublished)). Simulations of fluid flow in the unsaturated zone show that the percolation flux to the repository level is approximately the same as the surface infiltration. Some simulations show that flux to the water table in the area of the repository may be different, mainly because flow can be diverted eastward above the low permeability basal vitrophyre of the Topopah Spring Tuff. However, it is unclear how the Ghost Dance Fault may act to transmit water vertically to the water table beneath the repository (Ritcey *et al.*, 1997; Wu *et al.*, 1996). Given the uncertainty of percolation to the water table, and for the purposes of this modeling work, percolation to the water table is assumed to equal surface infiltration. Percolation flux is modeled by assigning a constant mass generation rate to the grid blocks on the top-most model layer. The base of the Lithic Ridge confining unit is a no-flow boundary.

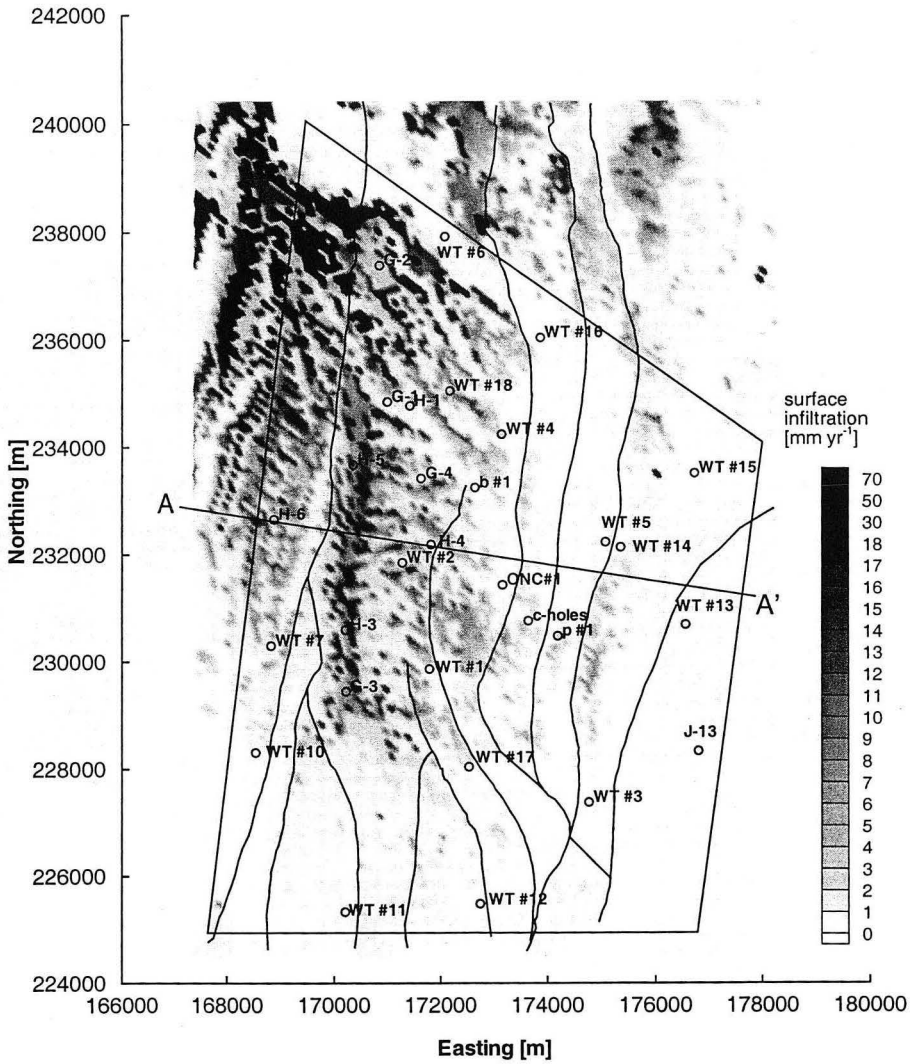


Figure 6.2. Infiltration distribution at Yucca Mountain, Nevada (from Flint *et al.*, 1996 (unpublished)).

## 6.5 Case 1: Displacement-Only Faults

### 6.5.1 Base Case

Figure 6.3 and Table 6.1 show the calibrated permeability distribution and Figure 6.4 shows the corresponding steady-state head distribution for the displacement-only faults model. The Prow Pass, Bullfrog, and Tram Tuff each have the characteristic higher-permeability central layer. The base of the Calico Hills Formation has a higher permeability than the upper layers, as observed by Geldon (1996).

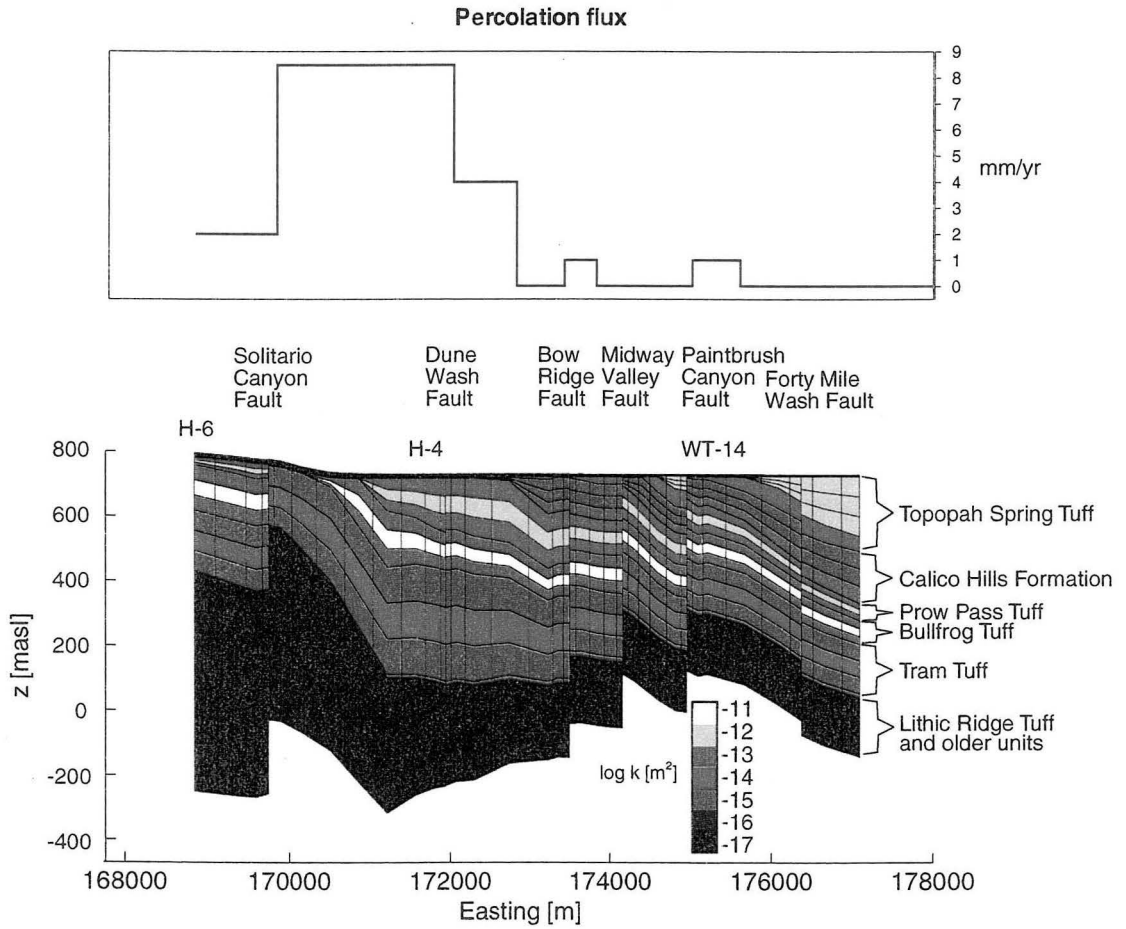


Figure 6.3. Percolation flux boundary and calibrated permeability distribution in the displacement-only faults model.

Table 6.1. Calibrated permeabilities for saturated zone model layers.

| ISM2.O geologic unit (Clayton *et al*., 1997) | SZ model layer | $k$ [$m^2$] |
|---|---|---|
| Topopah xl-rich nonlithophysal zone<br>Topopah xl-rich lithophysal zone<br>Topopah lithic rich member<br>Topopah upper lithophysal zone | tptrn | $2x10^{-12}$ |
| Topopah middle nonlithophysal zone | tpmn1 | $2x10^{-12}$ |
| Topopah lower lithophysal zone | tpmn2 | $2x10^{-12}$ |
| Topopah lower nonlithophysal zone | tpmn3 | $2x10^{-12}$ |
| Topopah lower densely welded vitric sub-zone<br>Topopah non-partly-welded vitric sub-zones<br>pre-Topopah Spring Tuff bedded tuff | tptv3 | $2x10^{-14}$ |
| Calico Hills Formation undifferentiated and | calc1 | $10^{-15}$ |
| pre-Calico Hills Formation bedded tuff | calc2 | $10^{-15}$ |
| " | calc3 | $10^{-13}$ |
| Prow Pass Tuff upper nonwelded zone | prow1 | $10^{-14}$ |
| Prow Pass Tuff welded zone | prow2 | $10^{-12}$ |
| Prow Pass Tuff lower nonwelded zone and<br>pre-Prow Pass Tuff bedded tuff | prow3 | $10^{-14}$ |
| Bullfrog Tuff upper nonwelded zone | bull1 | $10^{-13}$ |
| Bullfrog Tuff welded zone | bull2 | $10^{-11}$ |
| Bullfrog Tuff lower nonwelded zone and<br>pre-Bullfrog Tuff bedded tuff | bull3 | $10^{-13}$ |
| | tram1 | $5x10^{-16}$ |
| Tram Tuff undifferentiated | tram2 | $5.7x10^{-15}$ |
| | tram3 | $5x10^{-16}$ |
| pre-Tram Tuff bedded tuff | tram4 | $5x10^{-16}$ |
| | lith1 | $10^{-17}$ |
| Lithic Ridge Tuff and lava flows and breccia | lith2 | $10^{-17}$ |
| (defined in this report) | lith3 | $10^{-17}$ |

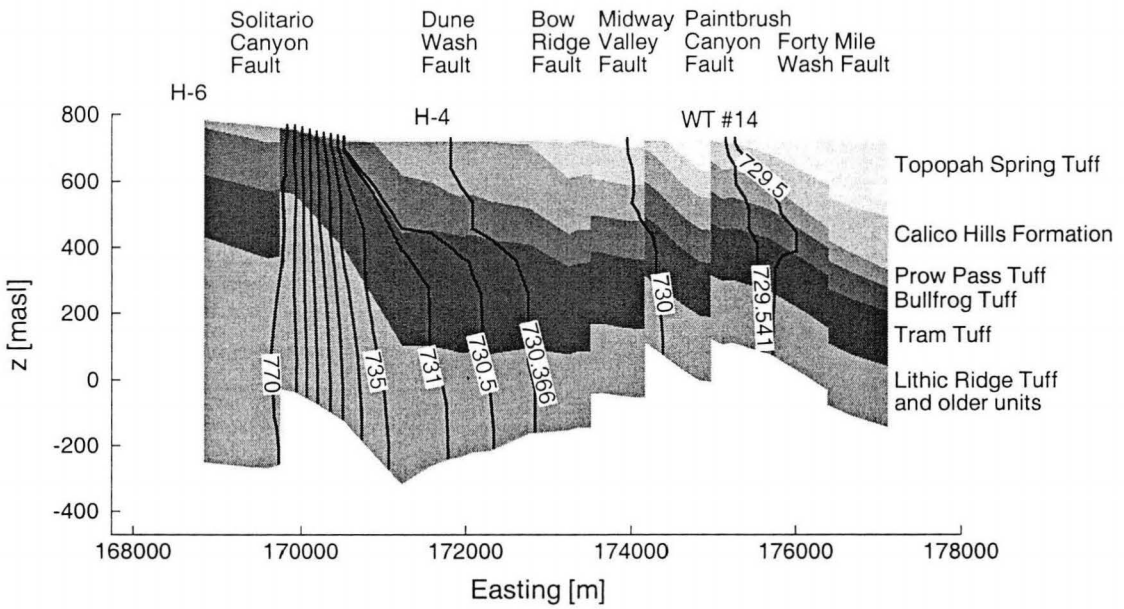


Figure 6.4. Calibrated steady-state head distribution in the displacement-only faults model. Vertical exaggeration = 4x.

The head contours in Figure 6.4 are spaced at 0.5 m intervals in the small-gradient zone and at 5 m intervals across the Solitario Canyon Fault. In addition, the head at borehole H-4 and WT #14 is shown. The residual head in borehole H-4 and WT #14 is +0.03 and -0.16 m, respectively, where residual head is the actual head minus the simulated head. The simulated gradient east of Solitario Canyon Fault is approximately 0.0002, which is within the observed range of 0.0001 to 0.0003 (Luckey *et al.*, 1996). The simulated specific discharge is 0.55 m/yr, which is of the same order as average estimates provided by the Saturated Zone Expect Elicitation Project (Geomatrix Consultants Incorporated, 1997). Specific discharge near the water table below the potential repository, located immediately west of Dune Wash Fault, is on the order of cm $yr^{-1}$ and at least 3.5 m $yr^{-1}$ in portions of the Lower Volcanic Aquifer.

The hydraulic head in the Lithic Ridge Tuff in borehole H-4 is 15 cm greater than the water table elevation (Table 2.2), and the resulting vertical gradient is one of several that are hypothesized to indicate vertical upwelling from the Carbonate Aquifer (Fridrich *et al.*, 1994; Luckey *et al.*, 1996). The simulated head in the Lithic Ridge Tuff in borehole H-4 is 40 cm greater than the water table elevation, which is of the same order as the observed difference. In addition, upward vertical head gradients are predicted over most of the model. This shows that upwelling from the Carbonate Aquifer is not necessarily the cause of the observed upward gradients. Rather, these gradients result from the geometry of the formation and the location of higher and lower permeability units. In this case, the higher-permeability Crater Flat Group overlies the Lower Volcanic Confining Unit. The upward flux through this confining unit is 10,000 times less than the horizontal flux in the Crater Flat Tuffs. Therefore, water that upwells through the deeper units will be diverted laterally immediately above the confining layer. The simulation also shows that the 45 m head difference observed across the Solitario Canyon Fault can result from the displacement of hydrogeologic layers only. Additional simulations showed that a high permeability fault zone cannot account for the moderate gradient.

A flow visualization tracer shows the downgradient flow pathways of repository-source waters that percolate vertically to the water table. Figure 6.5 shows the flow visualization tracer at 50 years due to a constant tracer mass fraction boundary located at the water table directly beneath the repository. The Prow Pass and Bullfrog Tuff are present at the water table here. The eastern column of grid blocks is a zero tracer mass fraction boundary, so the lateral extent of the tracer is only an apparent travel distance. Pore

velocity is a function of the specific discharge and porosity. Therefore, the simulation can describe the distribution for any porosity. For example, the porosity used for this simulation is $2.8 \times 10^{-4}$, so the simulation also describes flow after 500 yrs for $\phi = 2.8 \times 10^{-3}$. Travel time is not evaluated in this work, but the simulated time is noted so that the relative travel distance over time can be evaluated.

Figure 6.5 shows that water percolating to the water table will flow within the higher permeability layers of the Crater Flat Group. Abutment of higher to lower permeability units at faults causes water to flow upwards at faults and then back into the higher permeability layers displaced on the eastern sides of the faults, as shown at the Midway Valley and Paintbrush Canyon Fault. Hence, although there is displacement at faults, a contaminant would mostly remain within relatively thin layers more than 200 m beneath the water table.

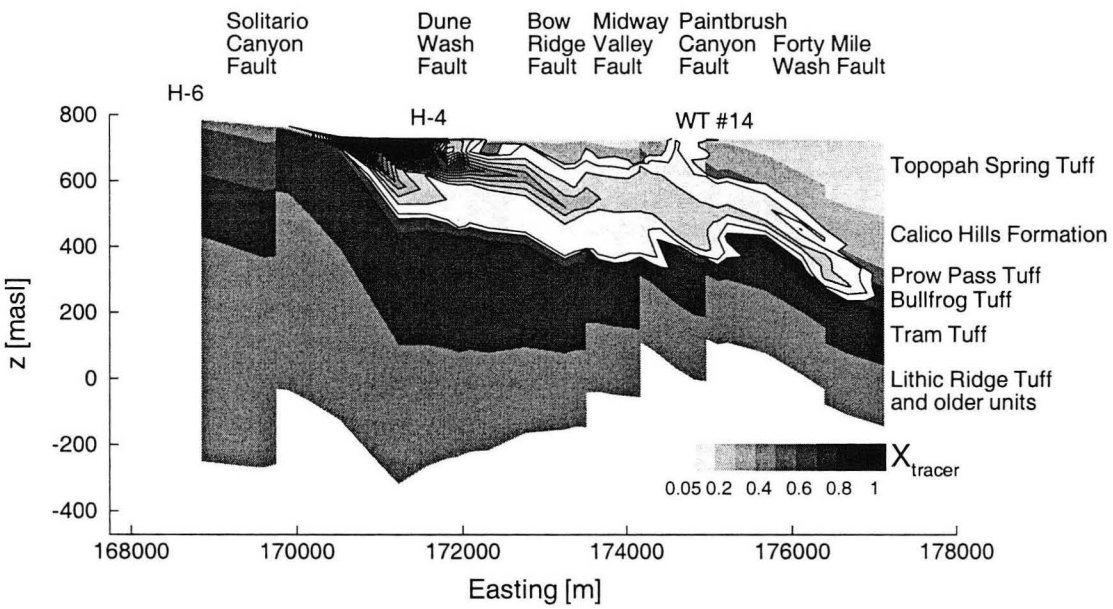


Figure 6.5. Flow visualization tracer at 50 years in the displacement-only faults model with percolation to the water table beneath the repository. Vertical exaggeration = 4x.

### 6.5.2 Effects of Unsaturated Zone Flow Pathway

Water percolating from the repository could be diverted to the east because of the presence of the easterly-dipping low permeability basal vitrophyre of the Topopah Spring Tuff. Under these conditions, the water would flow into the saturated zone where this unit intersects the water table, which is located immediately west of the Bow Ridge Fault. Figure 6.6 shows the flow visualization tracer at 50 years when the source is at this junction. The low permeability Calico Hills Formation beneath the vitrophyre restricts flow. For this case, the flow visualization tracer plume migrates only several hundred meters, compared to more than 7 km for upgradient source case, where the Bullfrog and Prow Pass Tuffs are present at the water table and provide a fast pathway for contaminants.

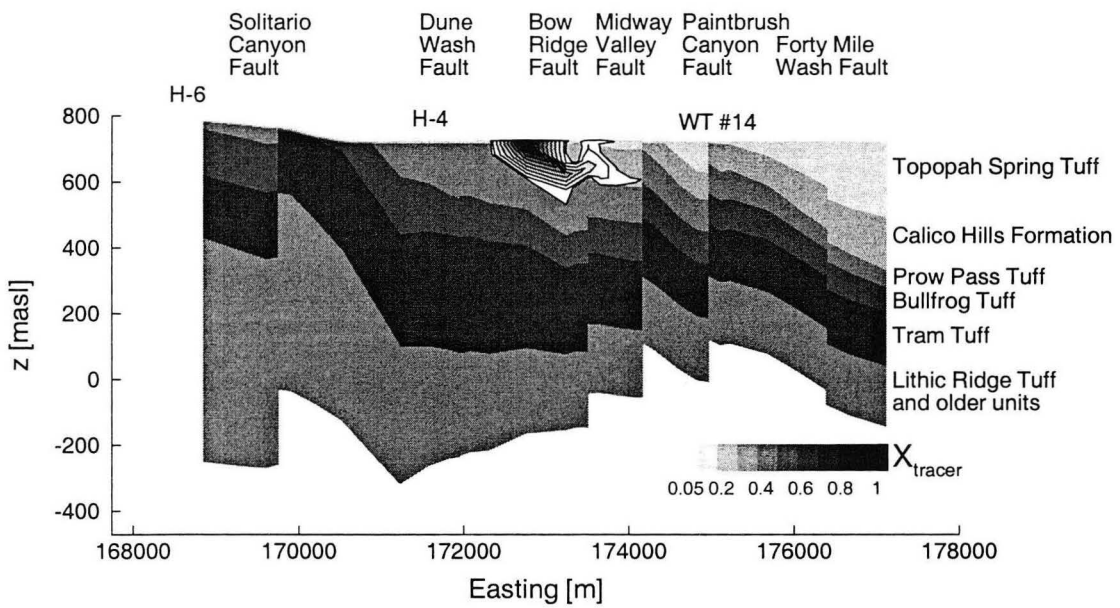


Figure 6.6. Flow visualization tracer at 50 years in the displacement-only faults model with tracer source at the Topopah Spring Tuff-water table contact. Vertical exaggeration = 4x.

Figure 6.7 shows the flow visualization tracer at 667 years. Due to the underlying Calico Hills Formation and the presence of the high permeability Topopah Spring Tuff at the water table immediately downgradient, most of the tracer flows close to the water table rather than downward within the dipping Crater Flat Tuffs.

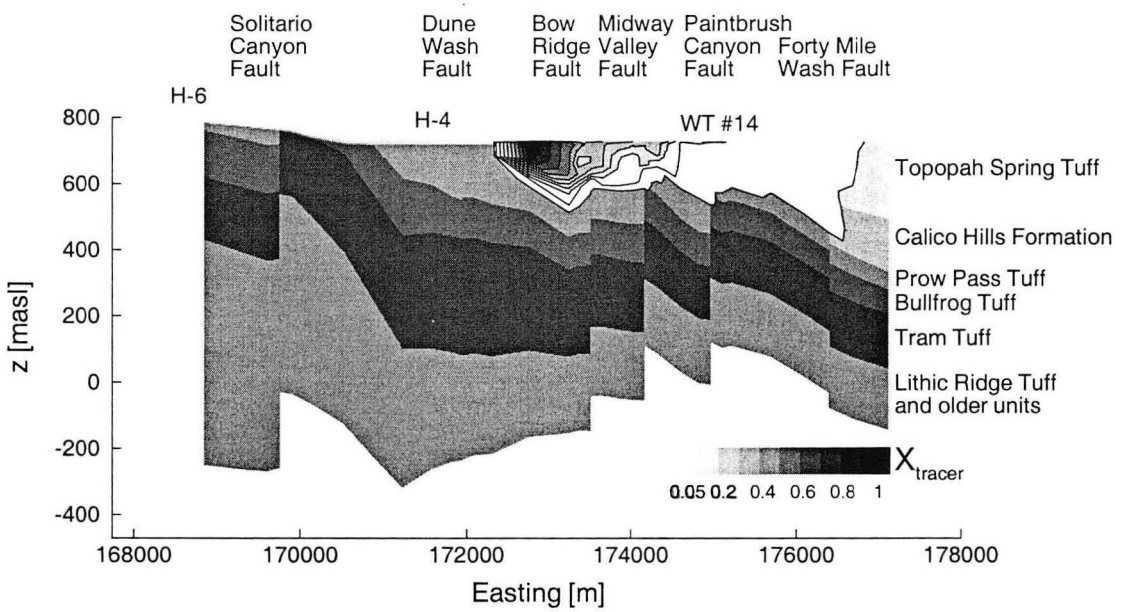


Figure 6.7. Flow visualization tracer at 667 years in the displacement-only faults model with tracer source at the Topopah Spring Tuff-water table contact. Vertical exaggeration = 4x.

### 6.5.3 Effects of Increased Percolation

Percolation rates in the future will be different than those today because of climatic changes, for example. A simulation was performed to examine the possible effects of this change by using a percolation rates 10 times larger than in the base case model. The simulated head and tracer distribution are not significantly different than the base case

simulation, which shows that the model is insensitive to these infiltration rates. Indeed, the maximum infiltration rate is 8 mm/yr compared to a specific discharge of 0.55 m/yr.

## 6.6 Case 2: High Permeability Faults

### 6.6.1 Base Case

The following simulations examine the effects of faults that have a high permeability fault zone. To calibrate this model, the layer permeabilities used in the displacement-only faults model were assumed and the fault permeabilities were adjusted until a best fit was found. A better fit was found, however, after a high permeability ($10^{-12}$ $m^2$) was assigned to the pre-Tram Tuff bedded tuff. This layer has a thickness between 10 and 50 meters over the cross section. The high permeability is suggested by borehole flow measurements in boreholes H-3, H-4, and H-5, which showed that 30%, 12%, and 5%, respectively, of the total flow originated from this layer.

The moderate gradient across the Solitario Canyon Fault could not be replicated using a high permeability fault zone. Rather, a permeability of $5x10^{-16}$ $m^2$ enabled calibration, as did a fault zone permeability of $10^{-12}$ $m^2$ for the Dune Wash, Bow Ridge, Midway Valley, and Paintbrush Canyon Fault. The latter permeability agrees well with available, albeit sparse data (Bodvarsson *et al.*, 1997; LeCain, 1998). The Forty Mile Wash Fault needed to be represented as a displacement-only fault to attain a reasonable fit to the observed head distribution. Figure 6.8 shows the steady-state head distribution for the high permeability faults model.

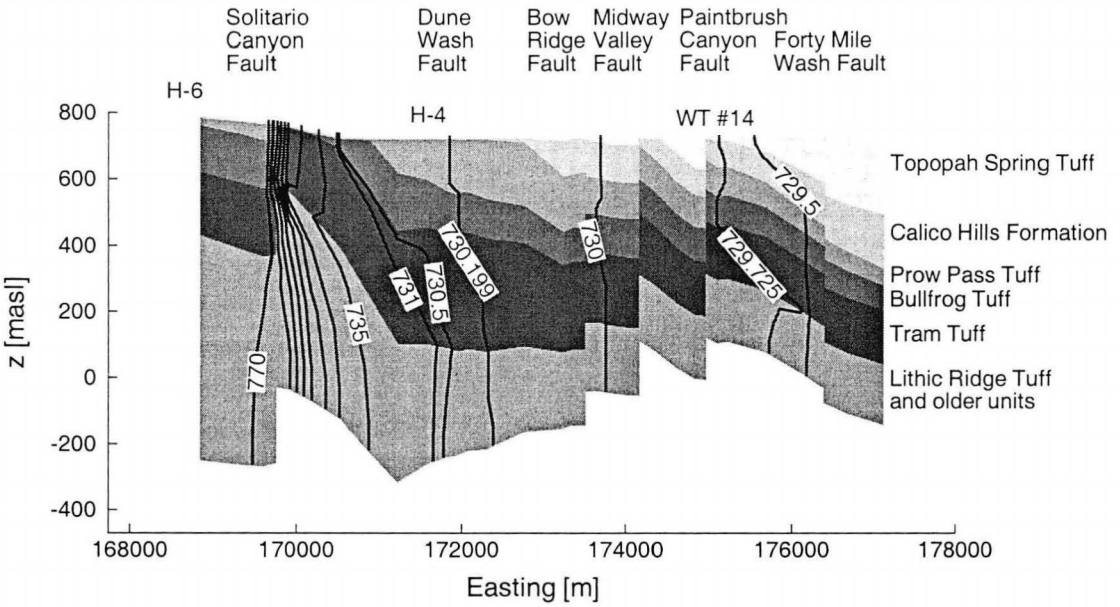


Figure 6.8. Calibrated steady-state head distribution in the high permeability faults model. Vertical exaggeration = 4x.

The residual head in boreholes H-4 and WT #14 is 0.2 and -0.03 m, respectively, and the vertical gradient at H-4 is reproduced. The simulated specific discharge is 0.57 m $yr^{-1}$, which is of the same order as average estimates provided by the Saturated Zone Expect Elicitation Project (Geomatrix Consultants Incorporated, 1997). Thirdly, the simulated small gradient is approximately 0.0002, which is consistent with field observations.

As in the displacement-only faults model, vertical gradients are present in the high permeability faults model. Figure 6.9 shows the flow visualization tracer at 50 years. The tracer distribution in general is similar to the displacement-only faults case in that water flows through the dipping and higher permeability layers of the Crater Flat Group and then upwards at faults. However, the tracer is more vertically dispersed in

comparison to the displacement-only faults case (Figure 6.5). This is due to the high permeability of the fault zones, through which water on the west side of a faults flows upwards within the fault and into the higher permeability layers on the east side. Water flowing within one layer on the western side can flow upwards and into multiple layers, for example, from the Prow Pass Tuff to the Prow Pass and Bullfrog Tuff. Figure 6.10 shows that water upwelling in the Dune Wash Fault flows into the Bullfrog Tuff, and to a lesser degree, into the Prow Pass Tuff, for example. This implies that compared to displacement-only faults, the vertical dispersion of a contaminant plume would be significantly greater if the faults are high permeability features.

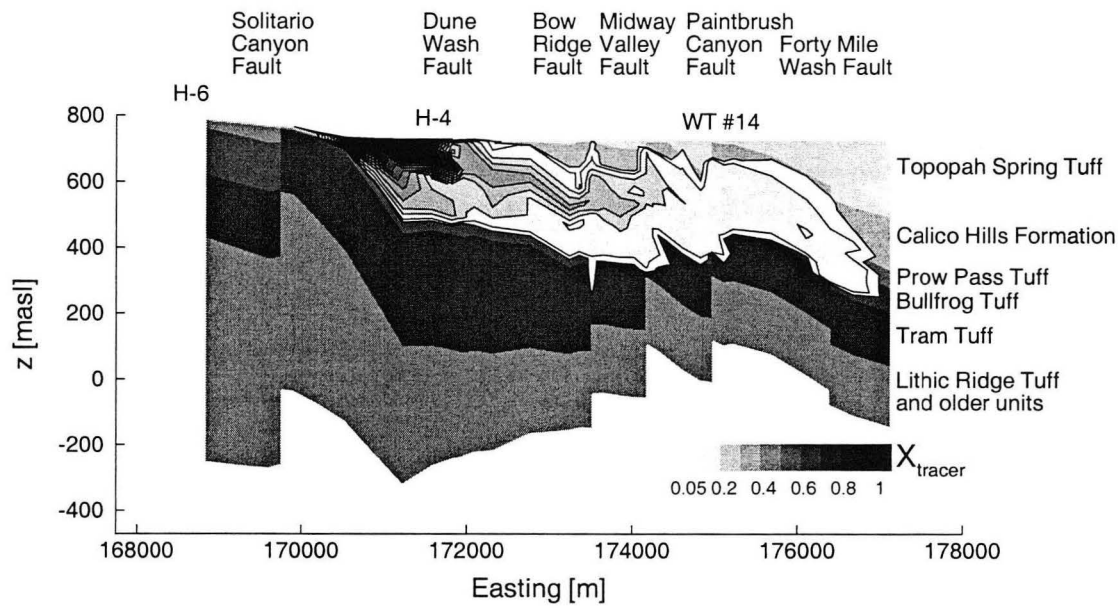


Figure 6.9. Flow visualization tracer at 50 years in the high permeability faults model with percolation to the water table beneath the repository. Vertical exaggeration = 4x.

Figure 6.10 shows that deep waters can upwell hundreds of meters through the faults. In this case, the tracer source is west of the Solitario Canyon Fault. Water from the west side of fault is channeled within the high permeability pre-Tram Tuff bedded tuff. Some of it then flows upwards within the Dune Wash Fault into the Crater Flat Group. Again, this illustrates that significant upwelling can occur through faults in the absence of any hydraulic connection to the Carbonate Aquifer.

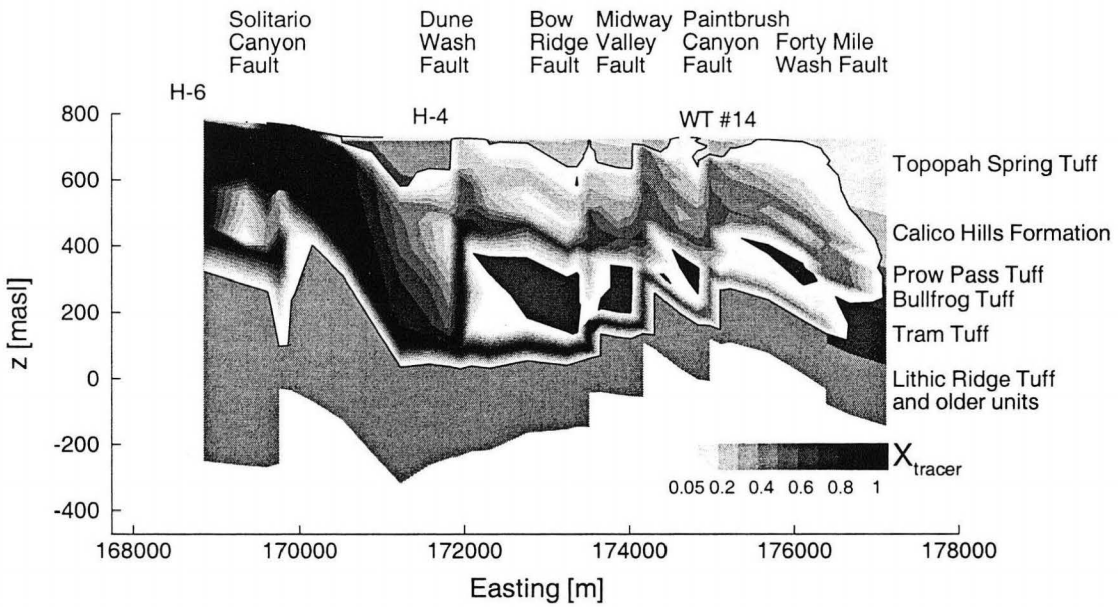


Figure 6.10. Flow visualization tracer at 50 years in the high permeability faults model with tracer source west of Solitario Canyon Fault. Vertical exaggeration = 4x.

### 6.6.2 Effects of Unsaturated Zone Flow Pathway

Figure 6.11 shows the tracer after 50 years when the source is at the Topopah Spring Tuff-water table contact. Initially, the presence of the nearby high permeability fault zone results only in a slight increase in vertical dispersion compared to the displacement-only faults case (Figure 6.6). Larger differences are apparent at later times, however. Figure 6.12 shows the tracer distribution at 667 years. The tracer shows that water flows upwards in the faults, transporting the tracer from dipping layers on the west side of the faults up towards the water table. Upward flow is present in the fault because of the high permeability layers in the Bullfrog and Prow Pass are displaced down-to-the-west. Downgradient, the high permeability Topopah Spring Tuff is present at the water table, so water upwells into this layer. The cumulative result is that the tracer is dispersed vertically near the source and is then channeled up towards the water table and horizontally downgradient. An analogous contaminant plume originating at the water table would remain close to the water table several kilometers downgradient. This implies that vertical dispersion of a contaminant plume would be inhibited if the source was at the Topopah Spring Tuff-water table contact. However, as shown above, vertical dispersion would be enhanced if water percolated into the Bullfrog Tuff beneath the potential repository. Hence, the influence of a particular type of fault cannot be generalized. For the case considered here, vertical dispersion may be further limited when the formation begins heating after emplacement of waste, and the water table temperatures become greater than those at depth. Thermo-hydrologic modeling of the saturated zone shows that repository heating will increase water table temperatures (Ho *et al.*, 1996). Thermal buoyancy could then restrict downward flow beneath the water table.

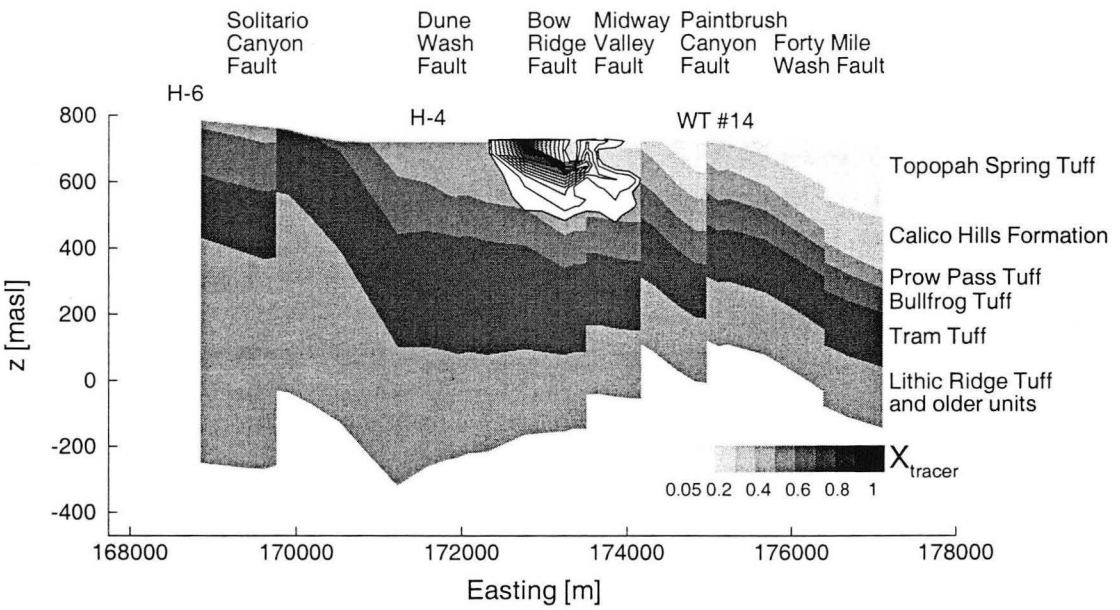


Figure 6.11. Flow visualization tracer at 50 years in the high permeability faults model with tracer source at the Topopah Spring Tuff-water table contact. Vertical exaggeration = 4x.

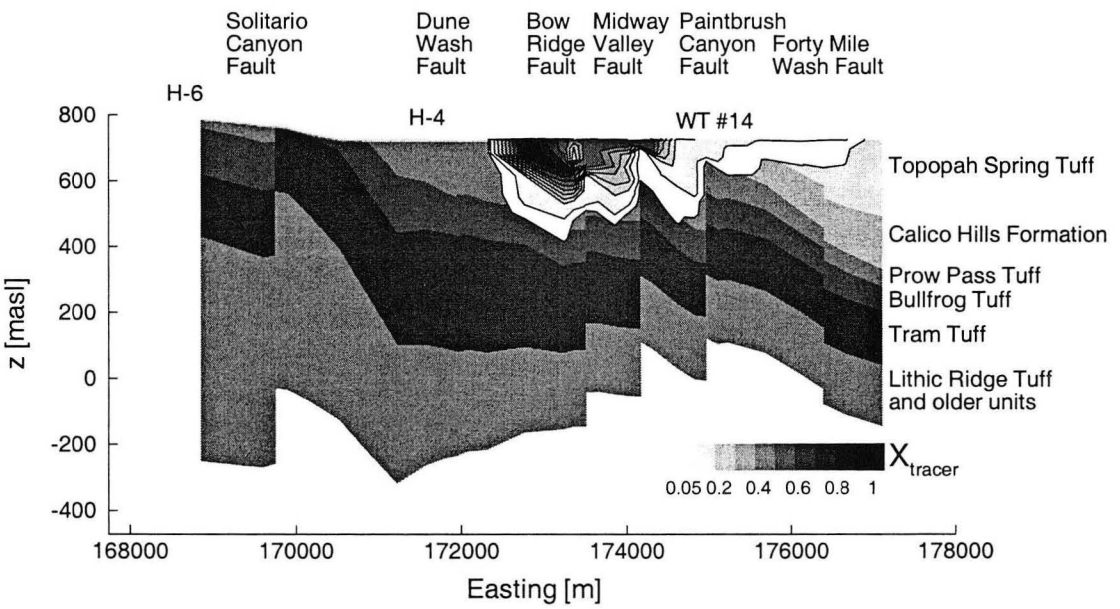


Figure 6.12. Flow visualization tracer at 667 years in the high permeability faults model with tracer source at the Topopah Spring Tuff-water table contact. Vertical exaggeration = 4x.

## 6.7 Case 3: Low Permeability Faults

### 6.7.1 Base Case

A significant effort was extended in an attempt to calibrate the model assuming low permeability fault zones. However, the model could not be calibrated using a constant low permeability for each fault zone. Low fault zone permeability were defined as ranging between $10^{-17}$ and $10^{-14}$ $m^2$. Figure 6.13 shows the steady-state head distribution for a fault zone permeability of $10^{-14}$ $m^2$. Modification of layer permeabilities did not significantly improve calibration. A large gradient (~0.004) across the Bow Ridge, Midway Valley, and Paintbrush Canyon Fault results from the close proximity of the low permeability zones. This gradient is approximately 20 times the observed small-gradient. Only constant fault properties were considered in the simulations described here, although it is possible that a model with spatially varying fault permeability could be calibrated. However, the inability to calibrate this simplified model indicates that faults cannot be considered low permeability features throughout the site.

Flow visualization was used to examine the effects of low permeability faults in general, although the model may not be applicable to Yucca Mountain. Figure 6.14 shows the flow visualization tracer at 50 yrs. Low permeability faults restrict flow within the higher permeability layers. The vertically continuous low permeability fault zone creates an barrier to flow in all of the higher permeability layers. As a result, water flowing within the higher permeability layers flows upwards and downwards at a fault, as shown at the Forty Mile Wash Fault, for example. However, in a full 3-D system, water would also flow along fault strike due to the impedance, so the flow pathway shown is exaggerated.

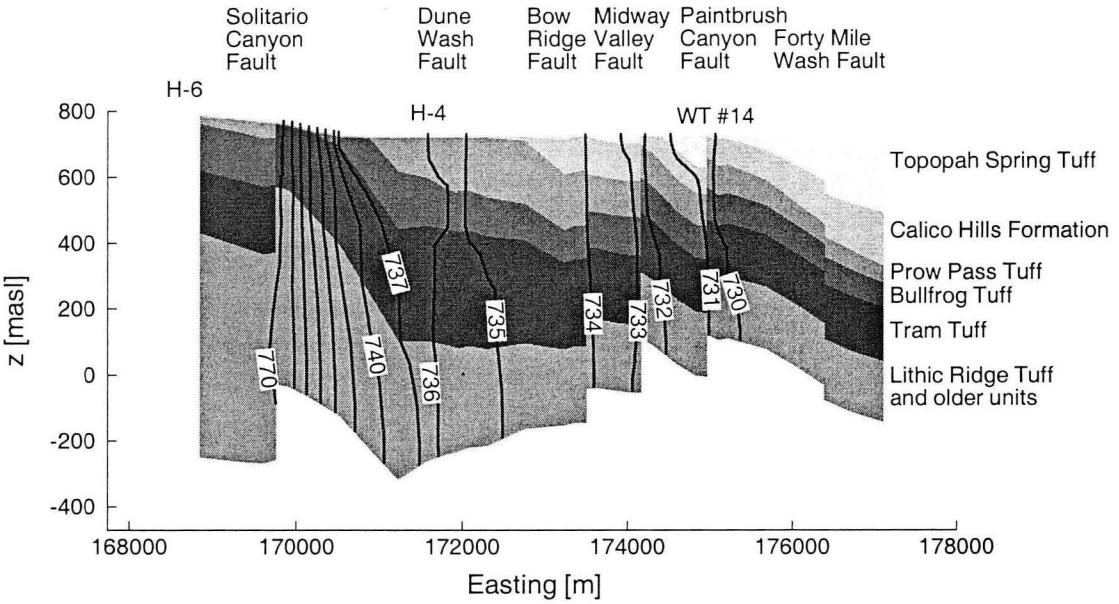


Figure 6.13. Steady-state head distribution in a low permeability faults model. Vertical exaggeration = 4x.

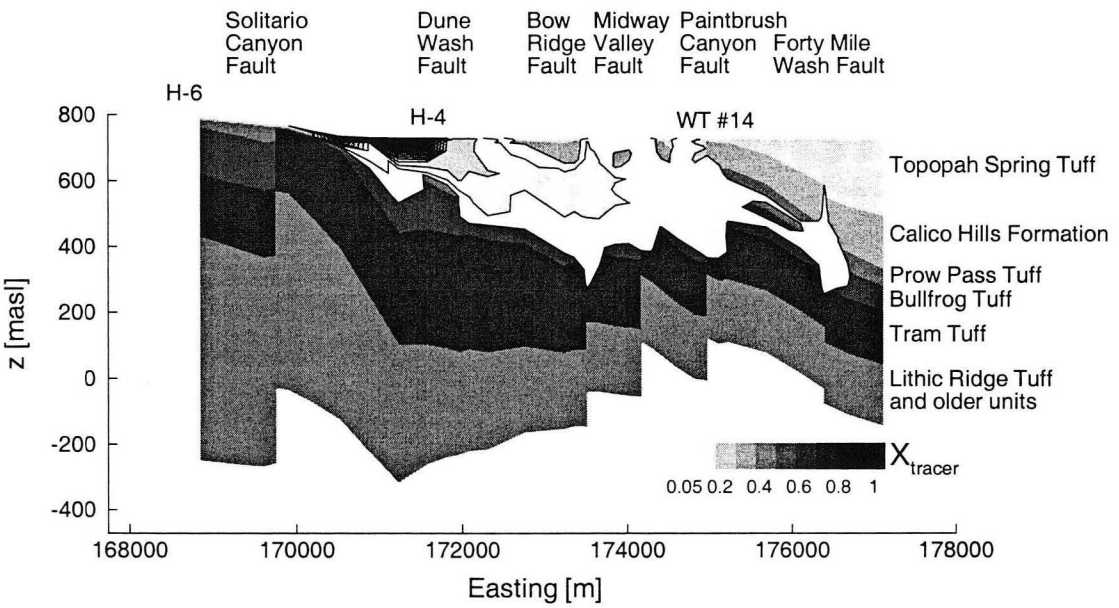


Figure 6.14. Flow visualization tracer at 50 years in a low permeability faults model with percolation below the repository. Vertical exaggeration = 4x.

## 6.8 Heat Flow

Water table temperature appears to be higher than average around the Solitario Canyon Fault and in the area around the Midway Valley Fault (Sass *et al.*, 1995) (Figure 2.4). These anomalies have been interpreted as evidence of upwelling of warmer fluid from the Carbonate Aquifer through faults (Fridrich *et al.*, 1991; Fridrich *et al.*, 1994). The following simulation shows how water table temperatures can be relatively higher near faults.

### 6.8.1 Boundary Conditions

A constant and uniform heat flux of 40 mW $m^{-2}$ was assigned to grid blocks at the water table. Estimated vertical heat flux along A-A' (Figure 4.16) ranges from 34 to 49 mW $m^{-2}$ between borehole H-6 and the Dune Wash Fault, and to as much as 62 mW $m^{-2}$ in the Midway Valley (Sass *et al.*, 1995). A constant temperature was applied to each grid block at the base of the model. Assigning the same temperature to each of these grid blocks would produce a variable water table temperature in a homogeneous model because the depth of the model is variable . In order to minimize the effect of the boundary geometry, the bottom grid blocks were assigned temperatures as a function of depth, such that the initial temperature gradient over the model is uniform. The corresponding temperature profile was defined assuming a constant thermal gradient of -30 °C $km^{-1}$ and water table temperature of 30 °C at 730 m. This approximation is based on the vertically averaged temperature gradients in boreholes J-13 and p#1, which are -10 and -40 °C $km^{-1}$, respectively. The temperatures assigned to the bottom grid blocks are

described by the equation

$T(z_{bottom})$ [m] = (-30 °C $km^{-1}$)x(z -730 m)x$10^{-3}$ km $m^{-1}$+ 30 °C.

The temperature was kept constant by assigning a large specific heat to these grid blocks.

### 6.8.2 Heat Conduction

The displacement-only faults model was used for this simulation. Each geologic unit was assigned a homogeneous thermal conductivity, as determined from core measurements (Table 5.1). All rock permeabilities were set to zero in order to simulate heat conduction only. The purpose of the simulation was to show how the thermal conductivity distribution influences the relative temperature variation at the water table. Calibration to actual temperatures was not performed. Figure 6.15 shows the simulated steady-state temperature profile. The simulated water table temperature is highest near the Solitario Canyon Fault. This is due to the underlying high thermal conductivity of the Composite Confining Unit and the Tram Tuff, which are very thick and close to the water table (Figures 4.6 and 4.7).

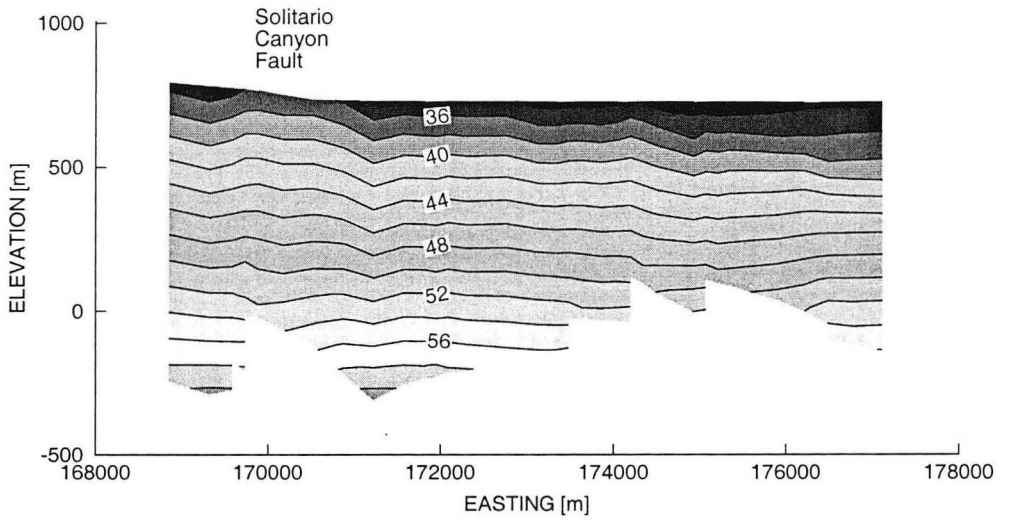


Figure 6.15. Steady-state temperature distribution due to heat conduction in the displacement-only faults model. Vertical exaggeration = 4x.

### 6.8.3 Analysis of Temperature Data

The water table temperature map of Sass *et al.* (1995) was constructed using borehole temperature logs. Analysis of these logs and of borehole flow logs reveals that some of the elevated water table temperatures are the result of fluid advection in the borehole, which is a local phenomena that does not indicate upwelling in the surrounding rock. Borehole H-5, located to the northeast of Solitario Canyon, has a water table temperature of 35.5 °C. Figure 6.16 is the temperature log for borehole H-5. Arrows mark the locations where the borehole intersects discrete, high permeability intervals where flow was produced during a borehole-flow survey. Water enters the borehole and advects upward, resulting in a reduced temperature gradient and therefore increased temperature at the water table. The temperature profile in H-5 is characteristic of upward fluid advection in a borehole (Plisga, 1987). Inspection of other borehole logs shows that relatively high water table temperatures and upwards borehole advection are also present

in boreholes H-4, H-5, H-6. In addition, the high water table temperatures in well WT #10 and WT #11, which do not intersect flowing intervals, are located in an area where the vertical heat-flux is 1.6 times the flux near H-5 and H-6.

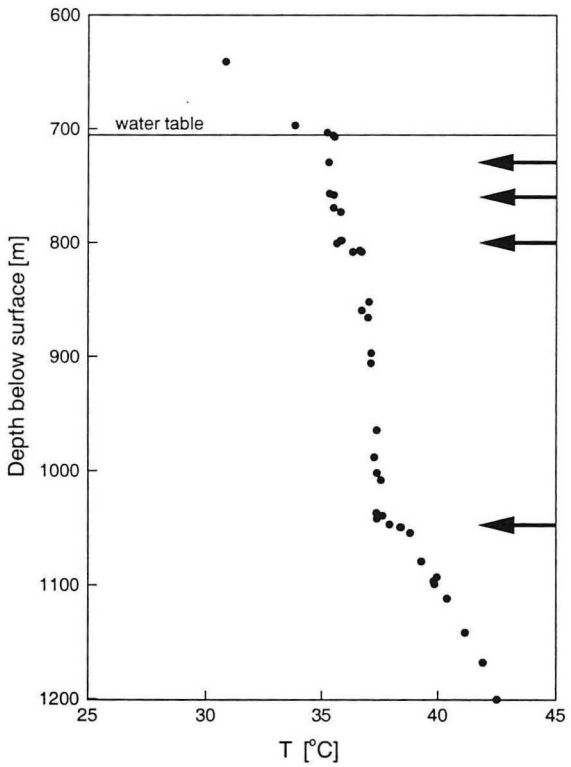


Figure 6.16. Temperature log for borehole H-5. Arrows mark discrete intervals where flow was produced during a borehole-flow survey.

# 7. 3-D Simulations

## 7.1 Introduction

The benefit of the 2-D model is that simulations illustrate some of the effects of the faulted structure on groundwater flow and the cross-sectional model could clearly be visualized. In contrast, visualization of vertical flow in a 3-D model is difficult because flow is not unidirectional. Therefore, the degree to which upwelling and vertical dispersion occur along the actual section represented by the 2-D model (section A-A', Figure 4.17a) may be exaggerated or underestimated because water must flow in the x-z plane, whereas the path of least resistance might be parallel to fault strike, for example. The following simulations show the 3-D flow fields that result from the combined effect of the variable thickness, dip, and orientation of hydrologic layers, and from the variation of displacement along fault strike (Figure 4.13).

## 7.2 3-D Sub-Model

The full 3-D model was not used for the following simulations because it includes the perched water area located northwest of the potential repository. Two-phase (air + water) flow simulations are required to simulate perched water, but only single-phase simulations are described in this work. For these reasons, a 3-D sub-model is used. Figure 7.1 shows the boundary grid blocks of the sub-model, which has 43,844 grid blocks and 152,680 connections. The upgradient boundary is the 730.85 m water table contour located at the eastern side of the potential repository. Therefore, the effects of the faulted structure on repository-source waters can be simulated. The distance between the east and west side is approximately 7 km.

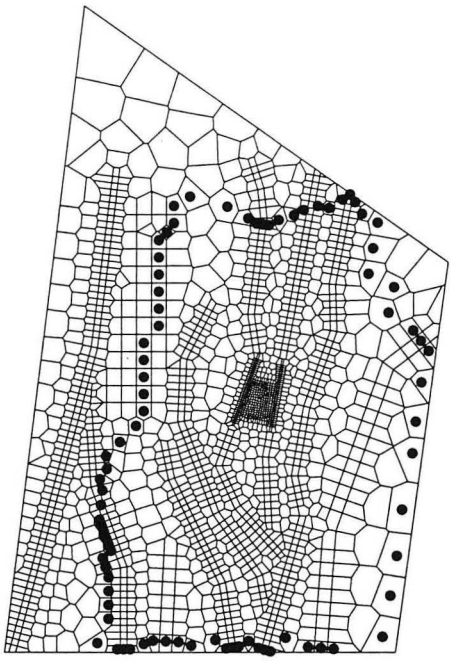

Figure 7.1. Boundary grid blocks of the 3-D sub-model.

### 7.3 Simulation Approach

Simulations were performed in the same manner as the 2-D simulations; a simulation was carried out to steady-state, and the resulting head distribution was used as the initial condition for the flow visualization tracer simulation. A constant tracer mass fraction of 1.0 was assigned to a 300 x 300 m grid block of the central layer of the Bullfrog Tuff that is located next to the upgradient boundary of the sub-model. The flow visualization tracer is representative of flow pathways of fluids that percolate into the Bullfrog Tuff located at the water table beneath the repository. The tracer simulation was carried out to 50 years, and the tracer distribution in different hydrogeologic layers is shown to illustrate the 3-D flow field. Because the tracer mass fraction at the boundary grid blocks is zero, the tracer will only extend to the model boundaries even if water from the source grid

block flows to the edges of the model. The tracer is not influenced by the boundary, however, because only advection is simulated.

## 7.4 Boundary Conditions

### 7.4.1 Hydraulic Head

A constant and uniform hydraulic head was assigned to each column of boundary grid blocks. The assigned heads correspond to the water table map of Tucci and Burkhardt (1995) (Figure 2.2).

### 7.4.2 Flux

The top and bottom of the model were no-flux boundaries. Zero percolation was assumed because infiltration is generally less than 10 mm $yr^{-1}$ in the small gradient zone (Figure 6.2), and the 2-D simulations showed that the head distribution is insensitive to the percolation rate.

## 7.5 Case 1: Displacement-Only Faults

As described earlier, calibration of the 2-D simulations served in part to constrain the range of properties needed for the 3-D simulations. Following this approach, the initial permeabilities used in the 3-D sub-model are the same as those in the calibrated 2-D displacement-only faults model. Fault properties are then adjusted to obtain a better fit to the water table surface. The initial permeabilities used are shown in Figure 6.4 and listed in Table 6.1.

Figure 7.2 shows the simulated steady-state water table. Contour lines have sharp bends because they are defined using linear interpolation of the heads at grid block nodes. A prominent feature is the relatively large gradient at the southern portion of the Paintbrush Canyon Fault. The gradient is 0.04 and more than ten times the observed gradient in the small gradient zone. It is due to the 200-290 m fault displacement in this area (Figure 4.13) and from the absence of high permeability layers. As shown in Figure 4.8 and Figure 4.9, only several meters of the Bullfrog Tuff is present beneath the water table on the eastern side of the Paintbrush Canyon Fault here, while the Prow Pass Tuff is completely absent. As a result, the Bullfrog and Prow Pass Tuff on the western side of the fault only have contact with the Tram Tuff and part of the Lower Volcanic Confining Unit. The contrast in permeability is as much as $10^5$, which effectively creates a barrier to flow. The simulation serves to illustrate how the variation of fault displacement along strike and the variable orientation and thicknesses of units results in a heterogeneous permeability distribution. In this case, the scale of a low permeability zone is several kilometers.

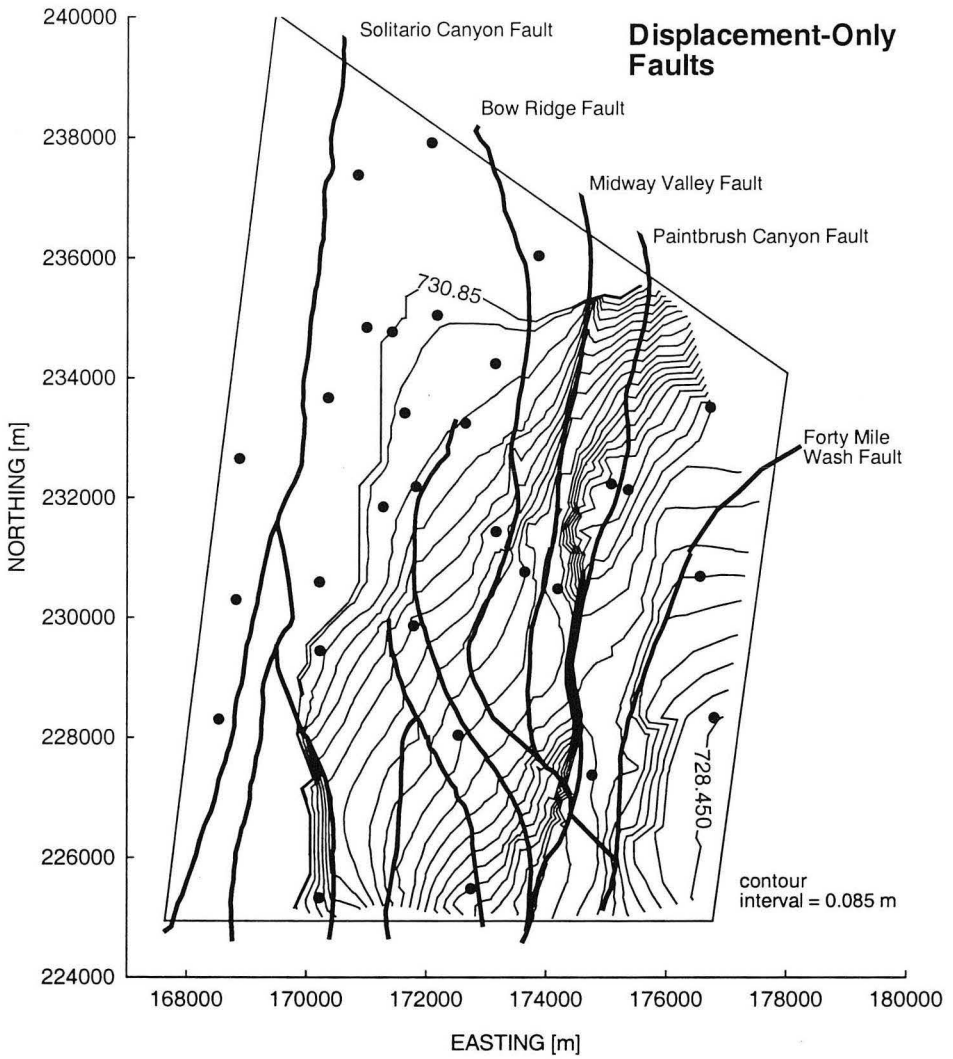


Figure 7.2. Steady-state water table in the displacement-only faults model.

Figure 7.3 shows the head distribution in the central layer of the Bullfrog Tuff. As indicated by the contour lines, water between the Bow Ridge and Midway Valley Fault flows to the south, whereas the water table gradients indicate eastwardly flow. The flow directions are significantly different, thereby illustrating that the water table gradient may not be a good indication of contaminant flow directions at depth. Note that the gradients

across faults in Figure 7.3 are not horizontal gradients. Rather, they are due to the difference in elevations across faults.

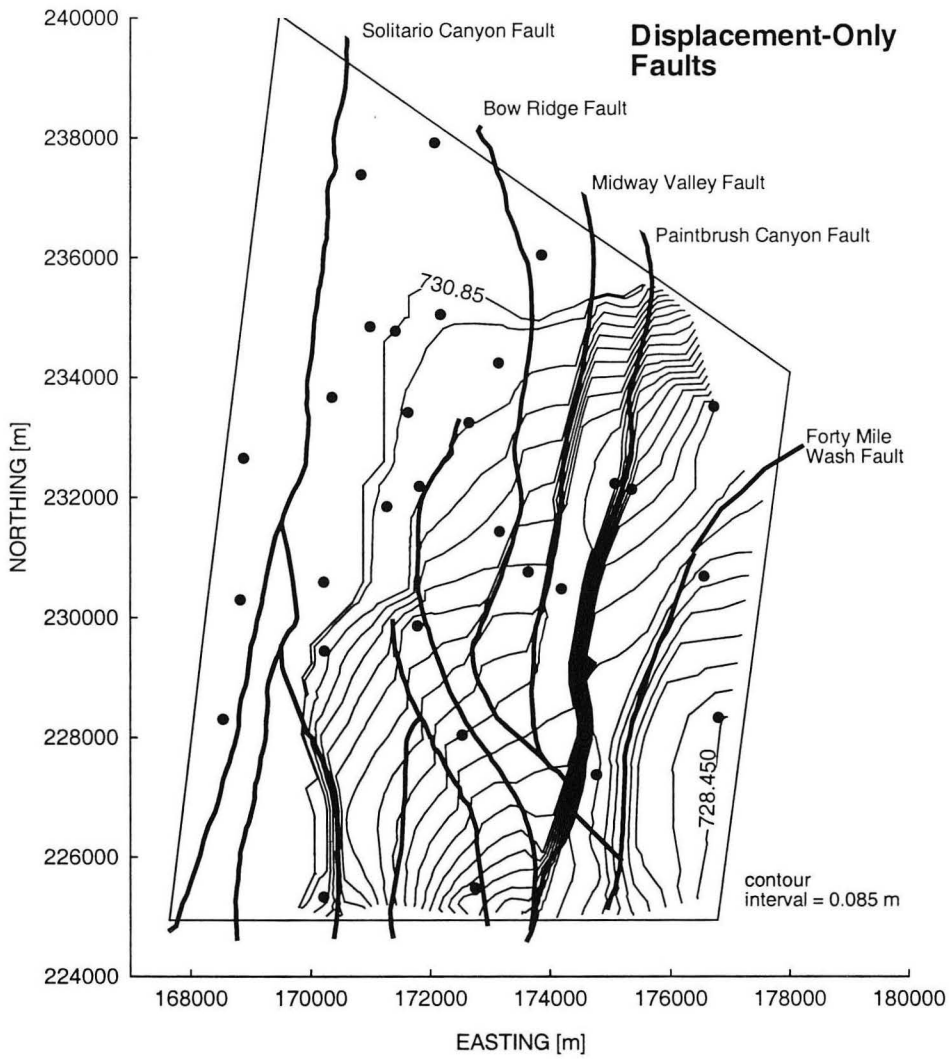


Figure 7.3. Steady-state head distribution in the central layer of the Bullfrog Tuff in the displacement-only faults model.

The heterogeneity introduced by the variation of fault displacement also results in large-scale flow channeling. Figure 7.4 shows the tracer in the central layer of the Bullfrog Tuff after 50 years. Water does not flow east of the Midway Valley Fault between 230,000 and 232,000 m latitude because of the nearby 200 meters of fault displacement and the subsequent contact between high and low permeability layers. Interestingly, Midway Valley Fault displacement decreases southward to less than 10 meters near the junction of the Midway Valley and Paintbrush Canyon Fault (Figure 4.13). As a result, flow is focused through this region because the high permeability Bullfrog Tuff is almost continuous across the fault. Further downgradient, the flow field bifurcates due to the presence of a flow barrier imparted by the large displacement at Paintbrush Canyon Fault. With regard to contaminant transport, this flow behavior indicates that the heterogeneity imparted by the faulted structure could produce large-scale channeling and macrodispersion of potential contaminants.

Another interesting phenomenon is the abrupt change from southward to northward flow across the Midway Valley Fault at approximately 230,000 m latitude. The head distribution in the Bullfrog Tuff indicates that there is a northward component of the gradient on the east side of the Midway Valley Fault at this location. Again, this reveals flow phenomena that can not be anticipated from 2-D models and water table contours. In this case, water flows in a direction nearly opposite the water table gradient.

The tracer distribution in the Prow Pass Tuff (Figure 7.5) indicates where upwelling occurs. For example, the locally high mass fraction near the junction of the Midway

Valley and Paintbrush Canyon Fault results from the upwelling due to the large displacement along these faults. No tracer is located between the Paintbrush Canyon and Forty Mile Wash Fault at approximately 228,000 m longitude because the Prow Pass Tuff is not present beneath the water table there.

Figure 7.6 shows the tracer distribution at the water table. Interestingly, upwelling due to displacement-only faults results in the presence of repository-source fluids at localized regions near the water table downgradient from the source. This flow pattern and the implied contaminant distribution is fundamentally different than a distribution predicted by analytic or numerical models of 2-D transport. The concentration distribution in a 2-D horizontal flow field with a continuous point source will have a continuously decreasing concentration with distance from the source (Bear *et al.*, 1993), and a similar distribution is predicted for 2-D flow in the vertical plane (Shan and Javandel, 1997). This simulation clearly demonstrates that the hydrogeologic structure is a dominant feature controlling the dispersion of potential contaminants on a regional scale. Consequently, simple analytic solutions cannot approximate the dispersion of contaminants at the water table, even if the source is also at the water table.

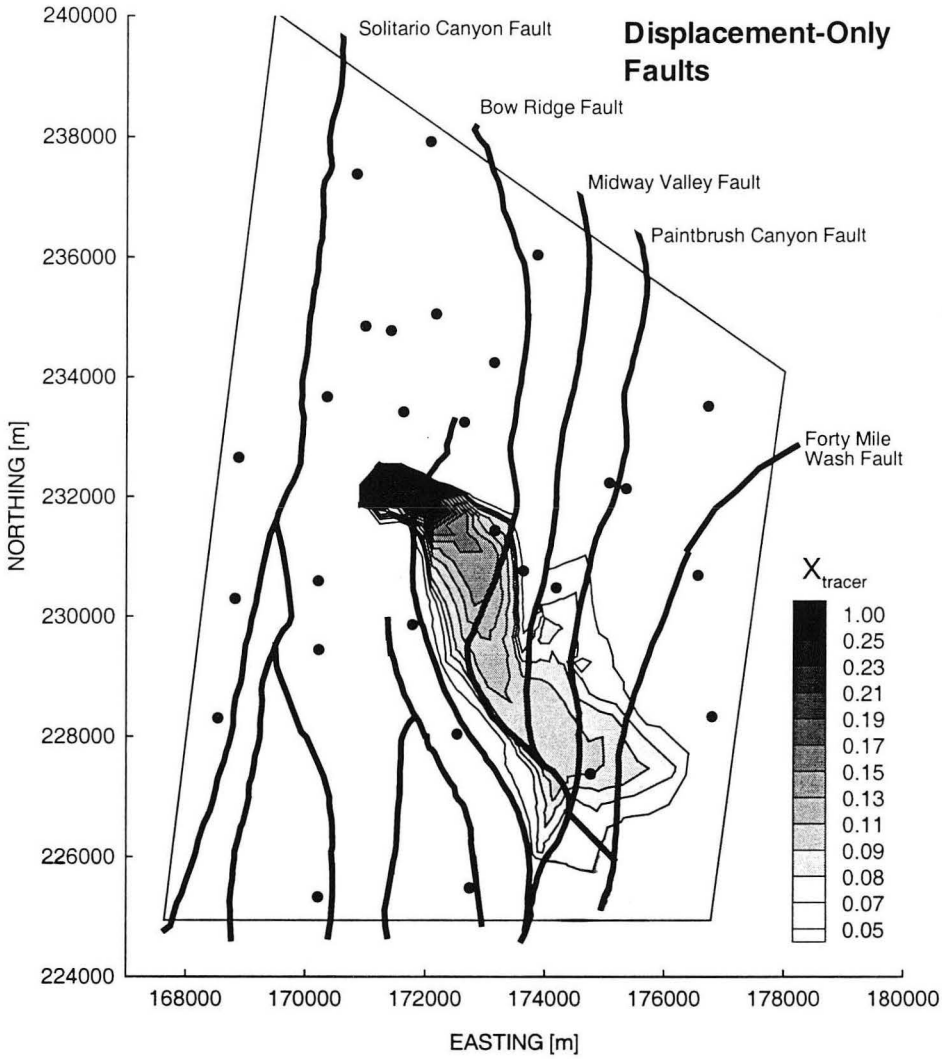


Figure 7.4. Flow visualization tracer in the central layer of the Bullfrog Tuff after 50 years in the displacement-only faults model.

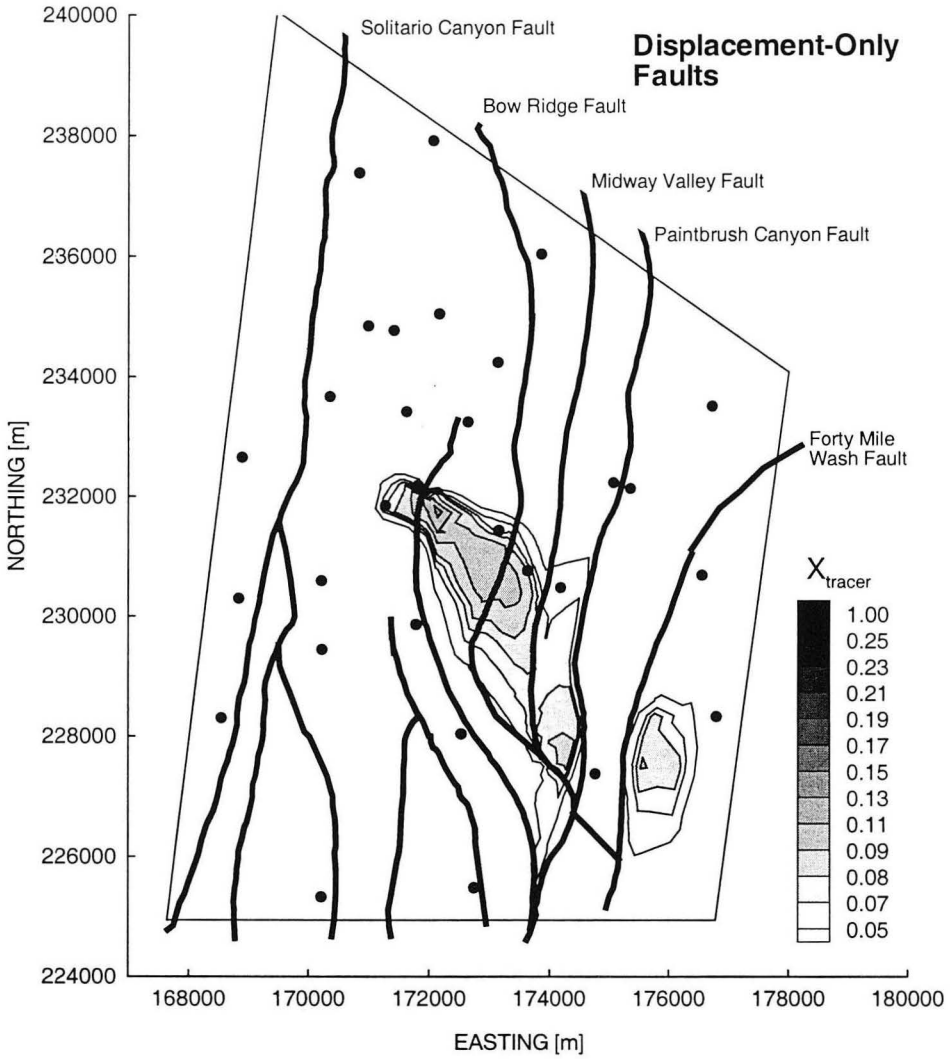


Figure 7.5. Flow visualization tracer in the central layer of the Prow Pass Tuff after 50 years in the displacement-only faults model.

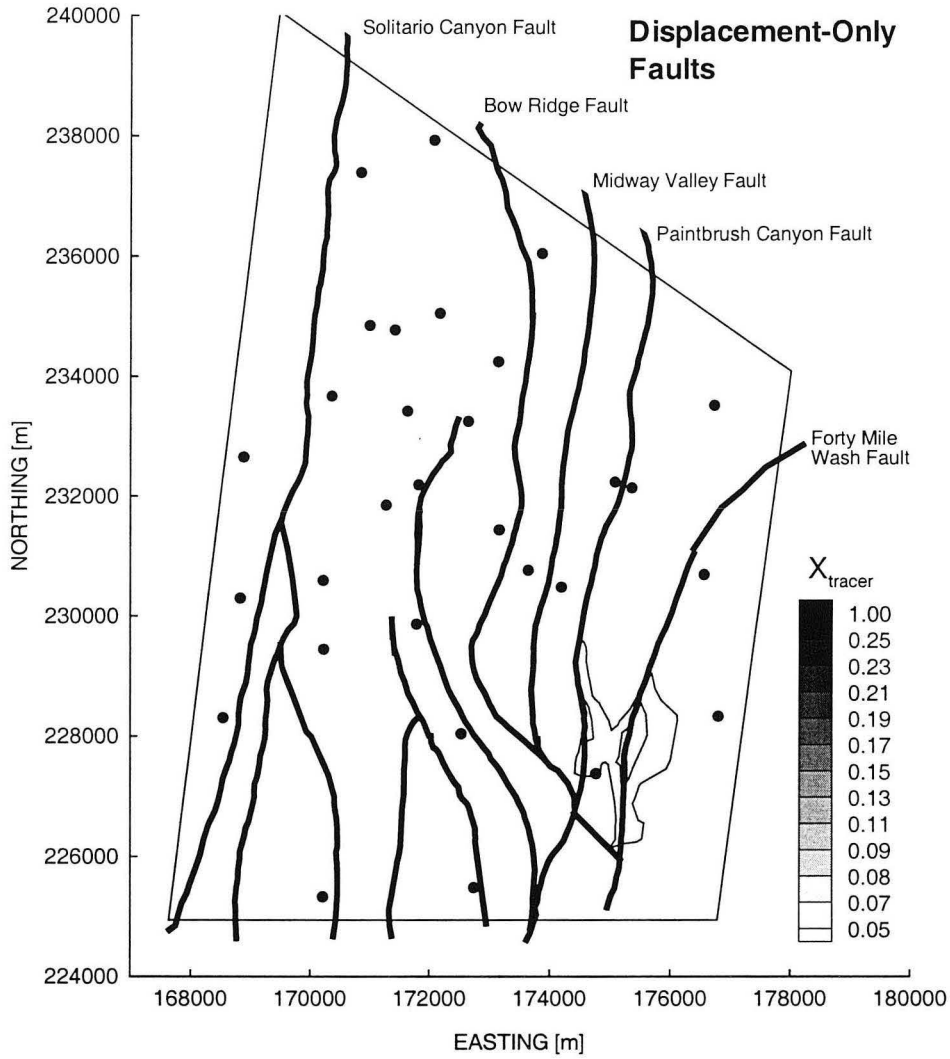


Figure 7.6. Flow visualization tracer at the water table after 50 years in the displacement-only faults model.

## 7.6 Case 2: High Permeability Faults

Figure 7.7 shows the simulated steady-state water table when all fault zones have a permeability of $10^{-12}$ $m^2$, and Figures 7.8 through 7.10 show the flow visualization tracer. In general, water table gradients at the faults are less than those in the displacement-only faults model because water can flow directly into high permeability layers on the adjacent fault side. As a result, water flows in the direction of the water table and is not laterally diverted at the abutment of layers, as illustrated in Figures 7.8 and 7.9. This implies that horizontal spreading of contaminants is less in a formation with high permeability faults, as compared to one with displacement-only faults. It also suggests that in this case a 2-D model may indeed be sufficient to examine the flow regime, since out-of-plane flow is not significant.

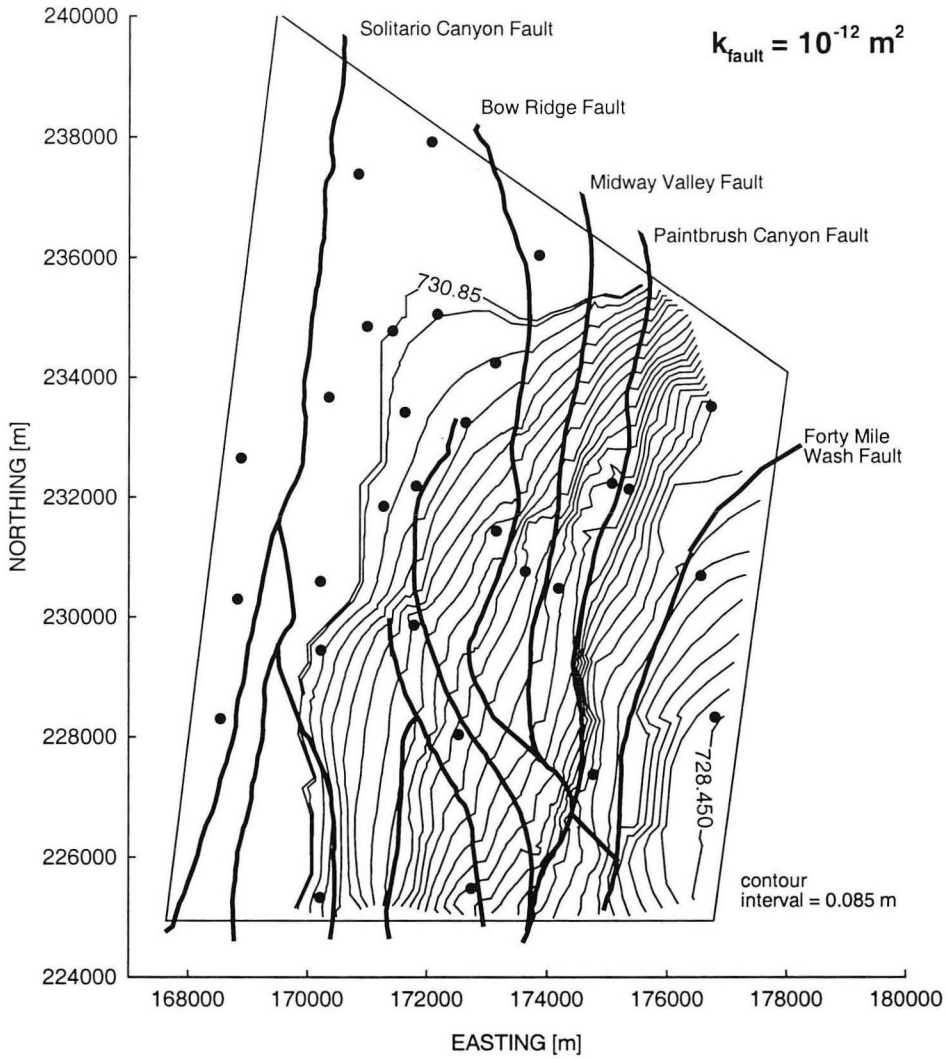


Figure 7.7. Steady-state water table in the high permeability faults model.

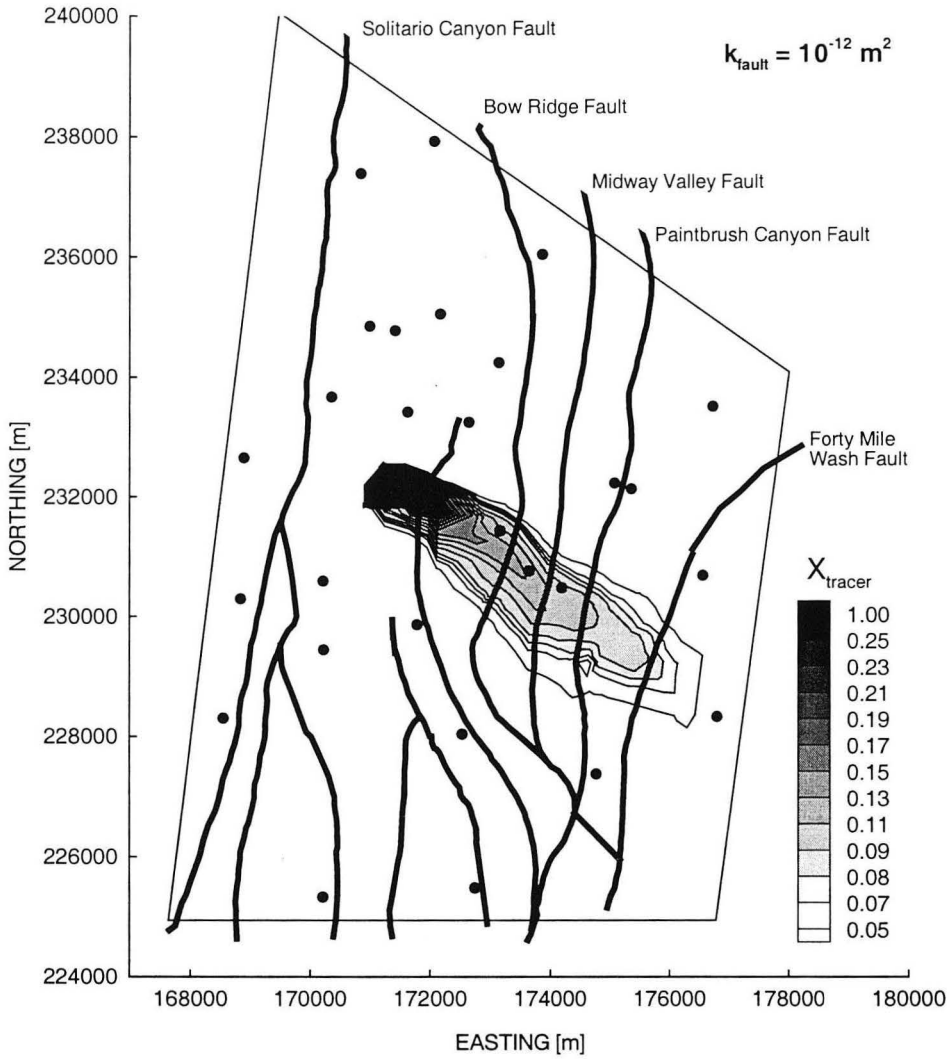


Figure 7.8. Flow visualization tracer in the central layer of the Bullfrog Tuff after 50 years in the high permeability faults model.

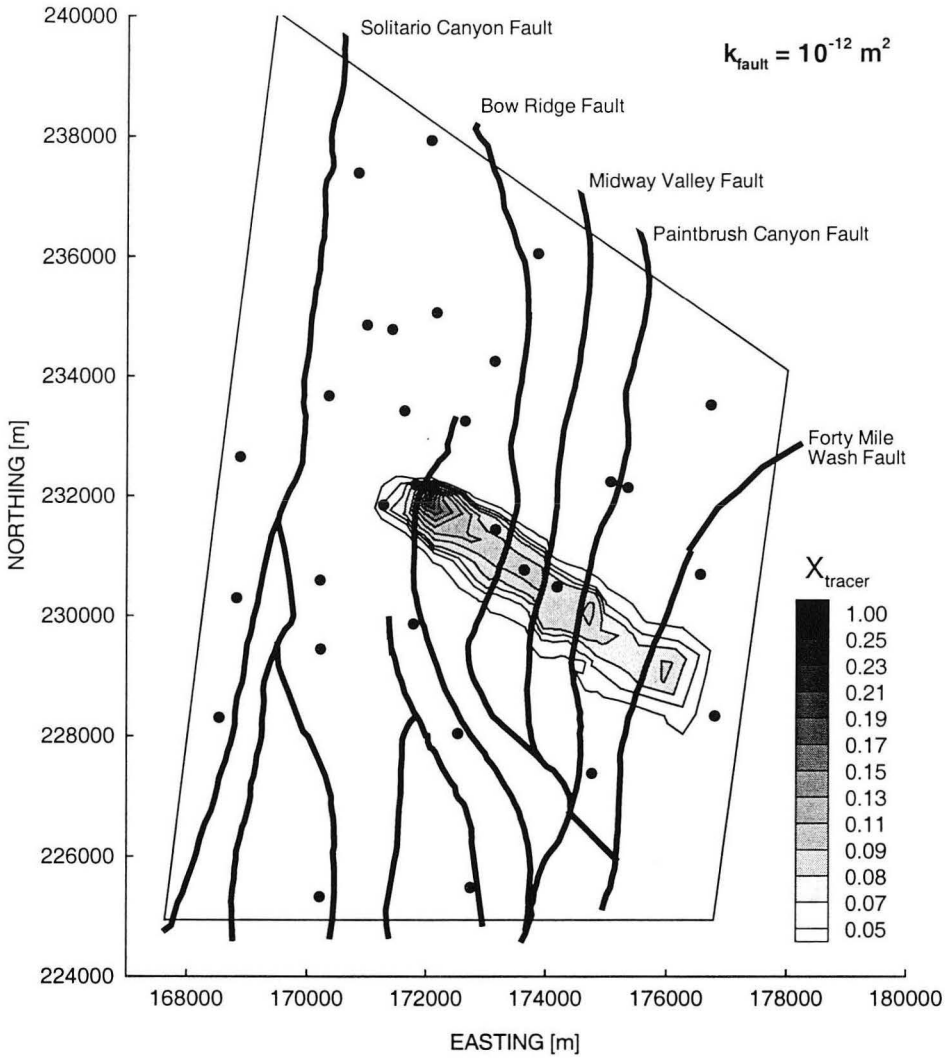


Figure 7.9. Flow visualization tracer in the central Prow Pass Tuff after 50 years in the high permeability faults model.

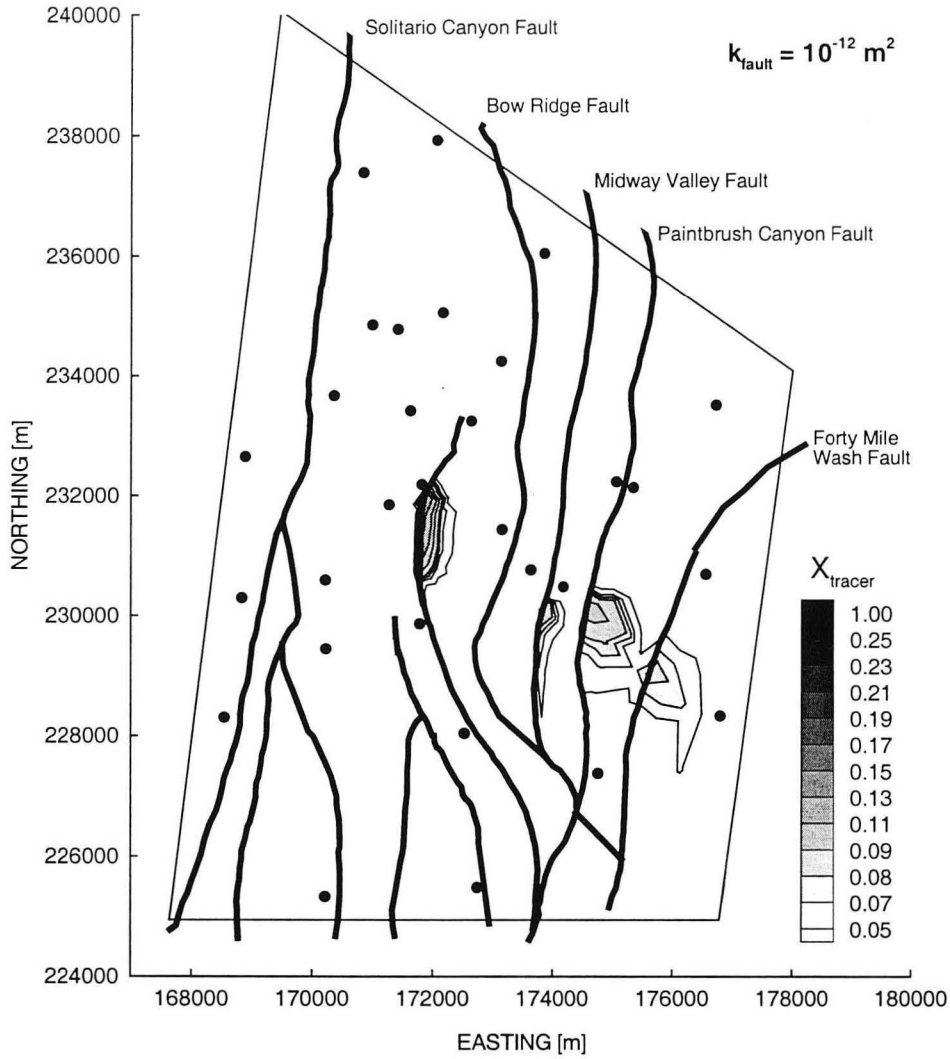


Figure 7.10. Flow visualization tracer at the water table after 50 years in the high permeability faults model.

## 7.7 Case 3: Low Permeability Faults

Figure 7.11 shows the simulated steady-state water table when all fault zones have a permeability of $10^{-14}$ m$^2$. The water table is very dissimilar to the observed water table; the direction of the water table gradient is towards the west in areas to the south, for example. Like the 2-D simulation, this simulation indicates that all faults cannot be low-permeability features.

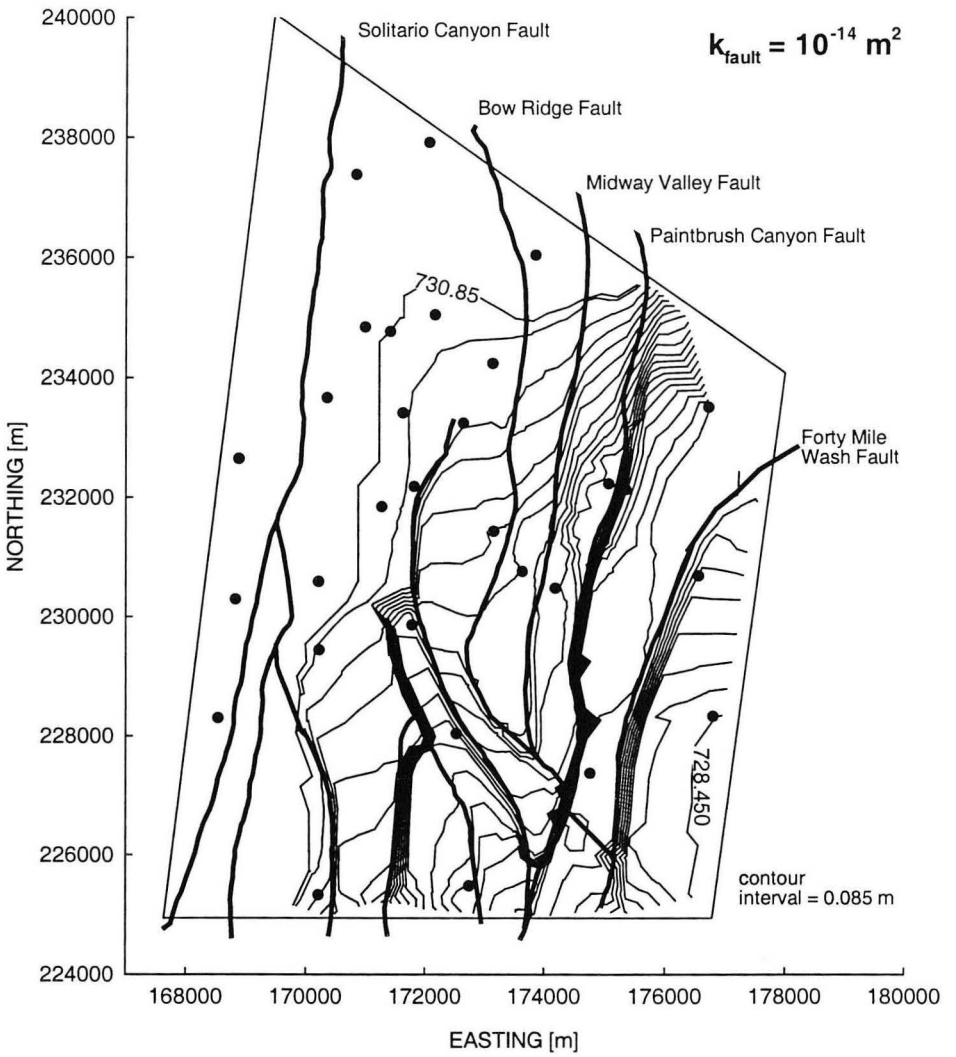


Figure 7.11. Steady-state water table in a low-permeability faults model with $k_{fault} = 10^{-14}$ m$^2$.

## 7.8 Sensitivity Analysis

A sensitivity analysis can help identify dominant hydrogeologic features and evaluate how calibration to head data is affected by the model boundaries, for example. Sensitivity can be measured using residual heads, where residual head is the measured minus the simulated head. The root mean squared error (RMS) is the best measure of error if residuals are normally distributed (Anderson and Woessner, 1992). RMS is defined as

$$\mathrm{RMS} = \left[ 1/n \sum_{i=1}^{n} (h_m - h_s)_i^2 \right]^{0.5},$$

where $h_m$ and $h_s$ are the measured and simulated head, respectively. Given the lack of data, the error distribution in the sub-model is assumed to be normally distributed.

### 7.8.1 Sensitivity to Model Boundaries

Calibration is sensitive to the model boundaries because the actual gradient is small, and because the gradient is orthogonal to the lateral boundaries and parallel to the northern and southern boundaries. Therefore, the simulated heads in a homogeneous model will match the observed heads well. Figure 7.12 shows the steady-state water table when a homogeneous permeability is considered. The corresponding RMS is 0.193. A particular model can be considered calibrated only if its RMS is less than 0.193, since only then can the simulated head field be attributed, at least in part, to the permeability distribution. Table 7.1 lists the residuals and the RMS for different models, which are described below. Other calibration criteria could include a definition of a maximum allowable residual, for example.

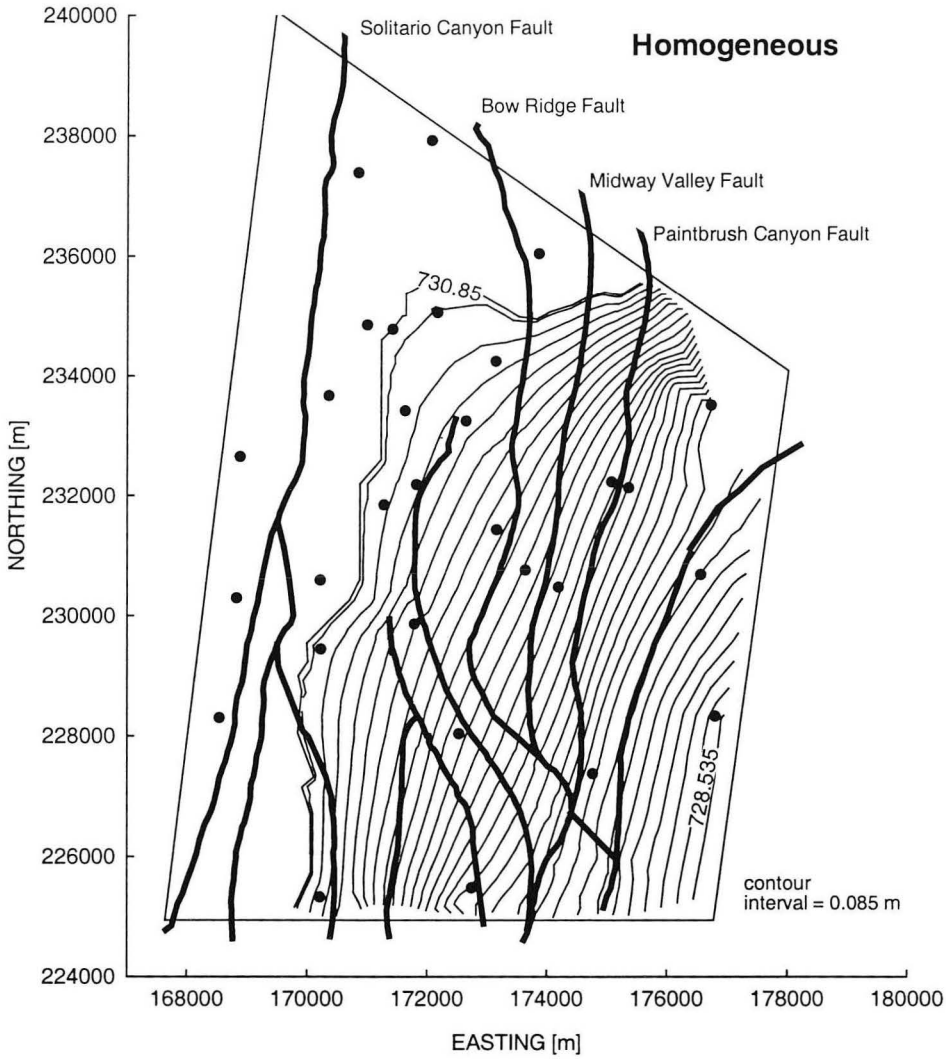


Figure 7.12. Steady-state water table in a homogeneous model.

Table 7.1. Residuals and calibration statistics for different 3-D sub-models. Asterisk indicates borehole is located at a boundary node and was not used in RMS calculation.

| | Homo- | Displace- | Permeable Fault Zone, $k$ [$m^2$] | | | | Hybrid 1 | Hybrid 2 |
|---|---|---|---|---|---|---|---|---|
| Borehole | geneous | ment-only | $10^{-14}$ | $10^{-13}$ | $10^{-12}$ | $10^{-11}$ | | |
| WT #1 | -0.058 | -0.047 | 0.177 | 0.027 | 0.052 | 0.201 | 0.083 | 0.065 |
| WT #2 | -0.121 | -0.149 | -0.193 | -0.170 | -0.129 | -0.092 | -0.132 | -0.124 |
| WT #3 | 0.495 | 0.592 | 0.442 | 0.639 | 0.575 | 0.390 | 0.226 | 0.275 |
| WT #4 | 0.094 | 0.000 | -0.030 | 0.001 | 0.051 | 0.028 | 0.021 | 0.003 |
| WT #11 | -0.029 | 0.061 | -0.078 | -0.036 | -0.010 | -0.007 | 0.064 | -0.008 |
| WT #12 | -0.074 | -0.087 | -0.076 | -0.070 | -0.072 | -0.061 | -0.055 | -0.089 |
| WT #13 | 0.073 | 0.234 | 0.263 | 0.237 | 0.166 | 0.080 | 0.224 | 0.221 |
| WT #14 | 0.052 | 0.264 | 0.120 | 0.069 | -0.019 | -0.222 | 0.125 | -0.136 |
| WT #15* | 0.000 | 0.000 | 0.000 | 0.000 | 0.000 | 0.000 | 0.000 | 0.000 |
| WT #17 | -0.304 | -0.373 | -0.144 | -0.246 | -0.244 | -0.200 | -0.195 | -0.364 |
| WT #18 | -0.076 | -0.086 | -0.094 | -0.090 | -0.083 | -0.083 | -0.087 | -0.088 |
| H-1* | 0.000 | 0.000 | 0.000 | 0.000 | 0.000 | 0.000 | 0.000 | 0.000 |
| H-4 | -0.274 | -0.337 | -0.425 | -0.370 | -0.304 | -0.233 | -0.299 | -0.281 |
| G-3 | -0.313 | -0.288 | -0.325 | -0.304 | -0.278 | -0.256 | -0.277 | -0.287 |
| b#1 | 0.038 | -0.086 | -0.106 | -0.069 | -0.018 | 0.001 | -0.049 | -0.041 |
| c-holes | -0.023 | -0.115 | -0.362 | -0.059 | 0.044 | 0.000 | 0.181 | -0.089 |
| J-13* | 0.000 | 0.000 | 0.000 | 0.000 | 0.000 | 0.000 | 0.000 | 0.000 |
| RMS | 0.193 | 0.241 | 0.234 | 0.233 | 0.204 | 0.169 | 0.162 | 0.179 |
| min \|r\| | 0.023 | 0.000 | 0.030 | 0.001 | 0.010 | 0.000 | 0.021 | 0.003 |
| max \|r\| | 0.495 | 0.592 | 0.442 | 0.639 | 0.575 | 0.390 | 0.299 | 0.364 |

The 3-D displacement-only and high permeability faults model simulated in the previous section have an RMS of 0.241 and 0.204, respectively. This does not suggest, however, that a similar flow field will not occur in a calibrated model. Indeed, large-scale channeling and upgradient-source waters at isolated regions downgradient are present in the calibrated models described below.

### 7.8.2 Sensitivity to Fault Permeability

Figure 7.13 shows the steady-state water table in a model where the permeability of all faults is $10^{-13}$ $m^2$. Again, the large gradient at the Paintbrush Canyon Fault is the prominent feature and the RMS is greater than 0.193. Therefore, all models with a fault

permeability ranging from $10^{-14}$ to $10^{-12}$ $m^2$ , as well as the displacement-only faults model, exhibit the large gradient at the Paintbrush Canyon Fault. As a result of this gradient, the average simulated heads in boreholes WT #3 and WT #13, located east of the Paintbrush Canyon Fault, are underestimated by 56 and 23 cm, on average. This indicates that the Paintbrush Canyon Fault zone permeability and/or of the permeability of the hydrologic layers there are the dominant features that influence flow patterns. These properties were therefore modified to obtain a better match to field data.

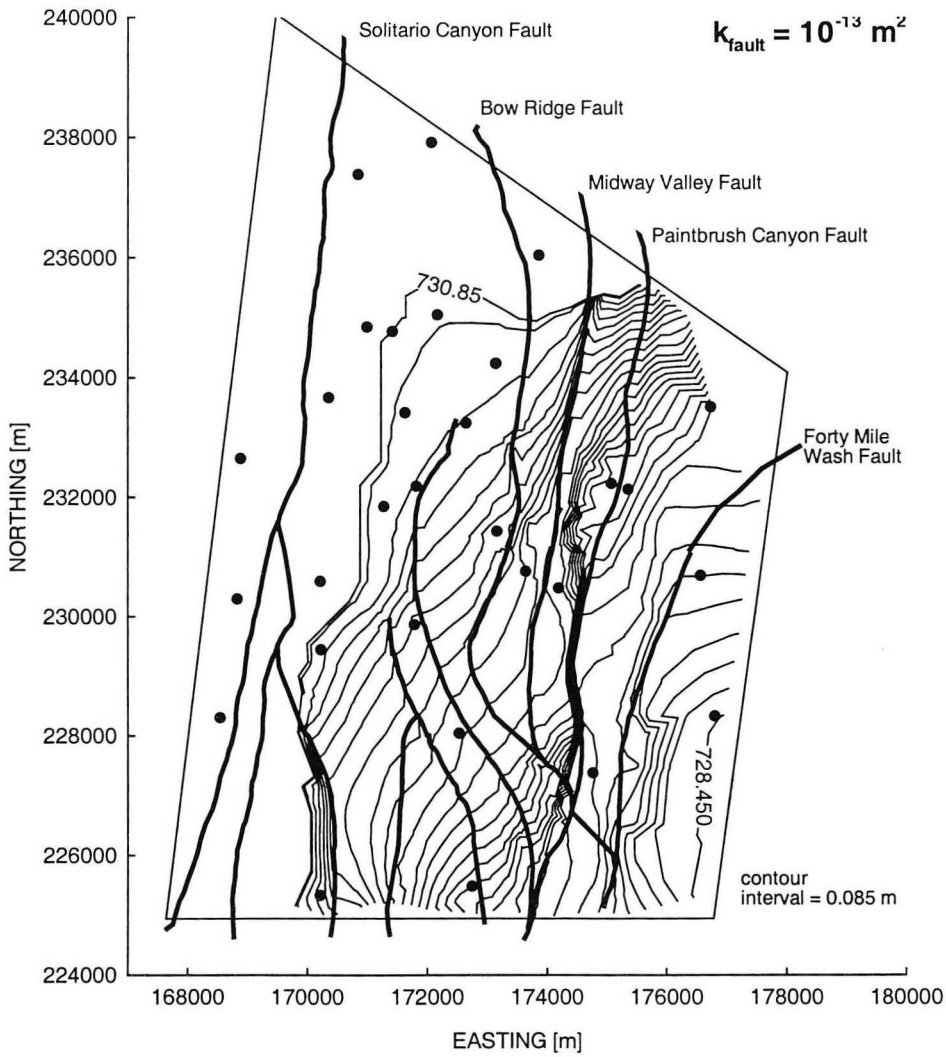


Figure 7.13. Steady-state water table in a model with fault permeability $k_{fault} = 10^{-13}$ $m^2$.

## 7.9 Alternative Models

Figure 7.14 shows the water table gradient in a model in which the permeability of all faults is $10^{-11}$ m$^2$. The RMS is 0.169 and therefore meets the RMS calibration criterion. However, it is unrealistic that all faults have a high permeability; a portion of the Paintbrush Canyon Fault is only 1 m wide and filled with cemented breccia, for example (R. Dickerson, U.S. Geological Survey, pers. comm., 1996).

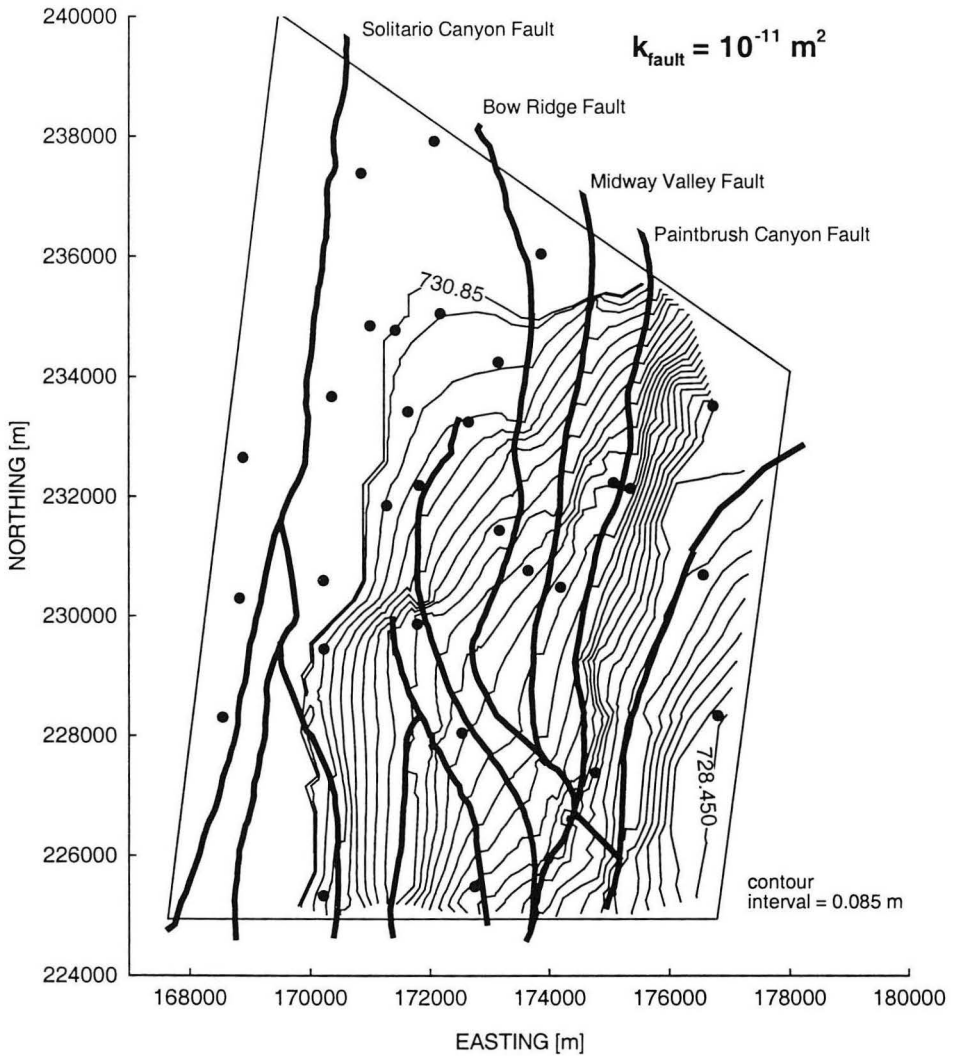


Figure 7.14. Steady-state water table in a model with fault permeability $k_{fault} = 10^{-11}$ m$^2$.

### 7.9.1 Hybrid 1

A modified displacement-only faults model also satisfies the calibration criterion. The first model, Hybrid 1, is the same as the displacement-only faults model, except that the Paintbrush Canyon Fault has a fault zone with permeability $k_{fault} = 10^{-11}$ m$^2$. There is some data suggesting that a high permeability zone exists. The exposure of the Paintbrush Canyon Fault west of Busted Butte in the southern model area has a 50 m wide brecciated zone (R. Dickerson, pers. comm., 1996). In addition, Geldon (1993) observed a flowing brecciated fault zone in the c-holes, which he interpreted to be the Paintbrush or Midway Valley Fault. Figure 7.15 shows the steady-state water table. A large gradient at the Paintbrush Canyon Fault is not present, and the RMS is 0.162.

The resulting flow field is different than the displacement-only faults model. Figures 7.16 through 7.18 show the tracer distribution in the Hybrid 1 model. The flow field is similar to the displacement-only faults model; water is diverted southward approximately 4 km due to the variable displacement of the Midway Valley Fault. It then flows eastward through the high permeability Paintbrush Canyon Fault, but the south-east bifurcation is not present. This implies that dispersion of a potential contaminant is less if the Paintbrush Canyon Fault has a high permeability. In addition, upgradient source water upwells near the water table farther north as compared to the displacement-only faults model.

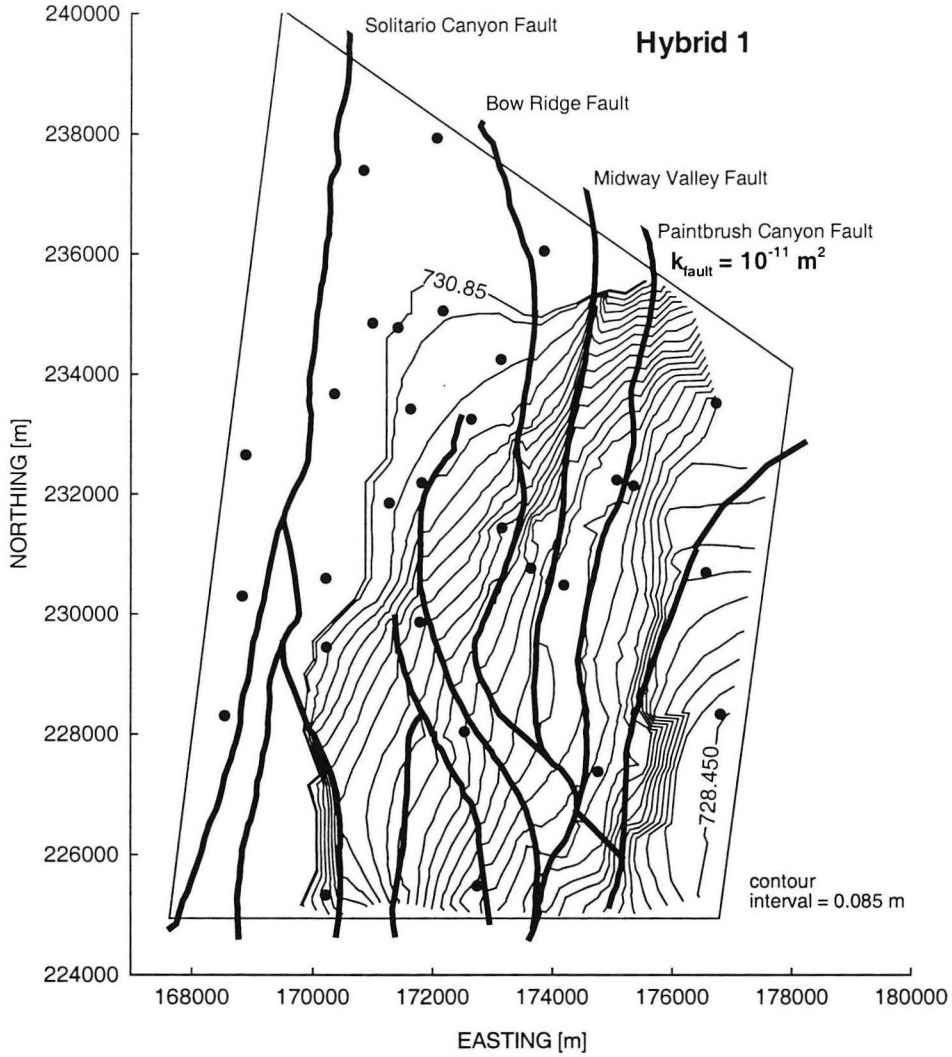


Figure 7.15. Steady-state water table in the Hybrid 1 model.

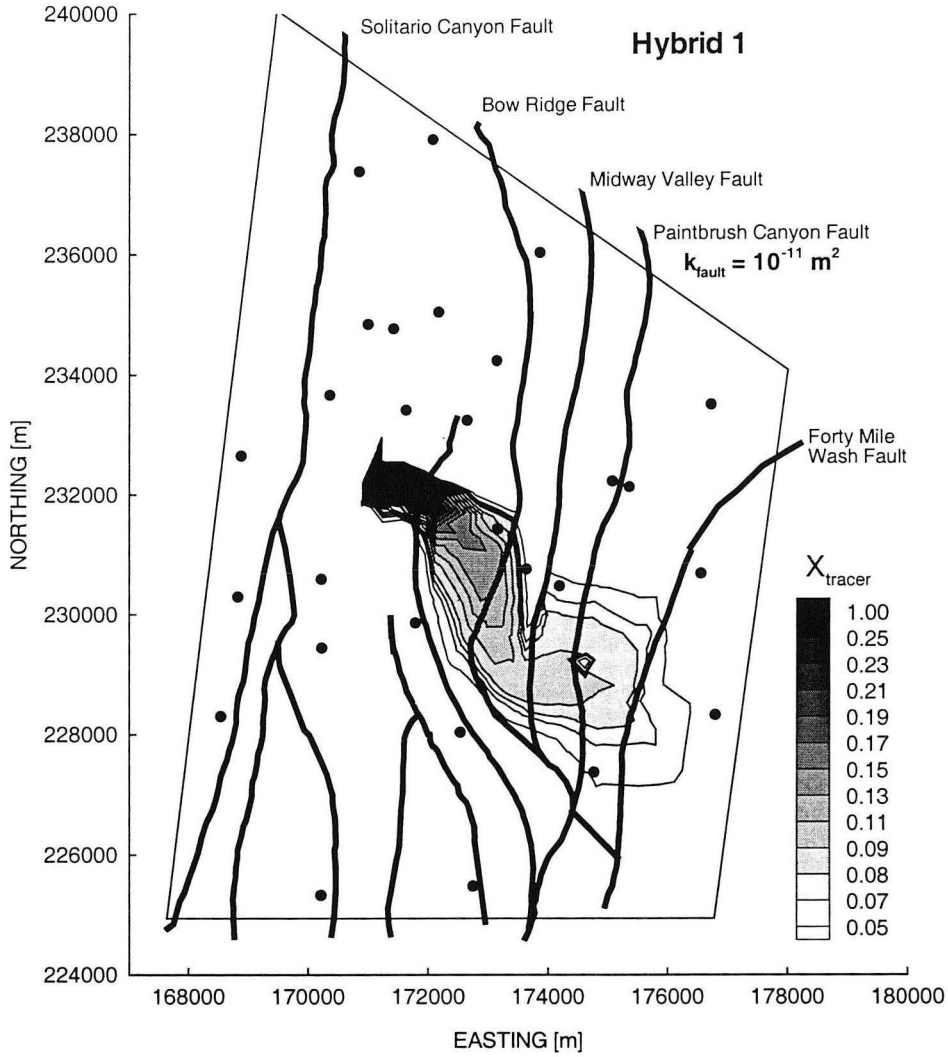


Figure 7.16. Flow visualization tracer in the central Bullfrog Tuff after 50 years in the Hybrid 1 model .

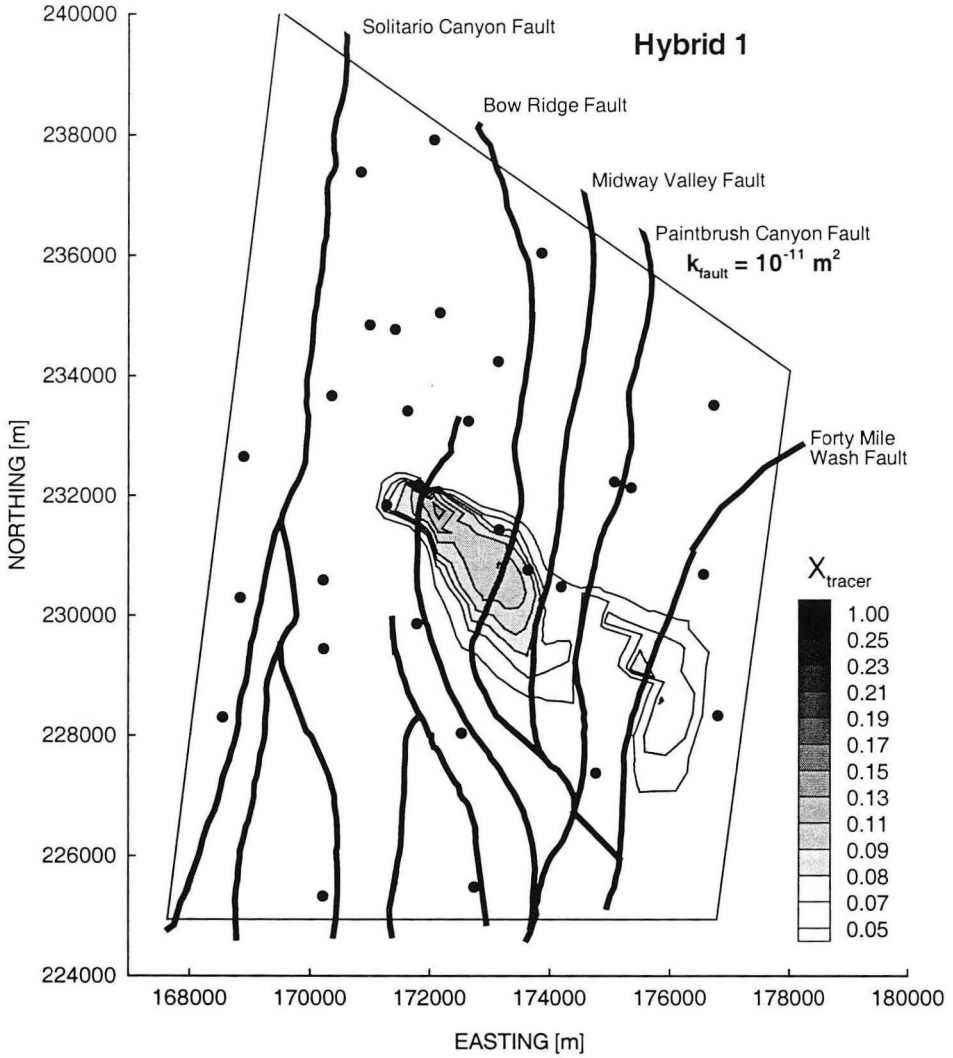


Figure 7.17. Flow visualization tracer in the central Prow Pass Tuff after 50 years in the Hybrid 1 model.

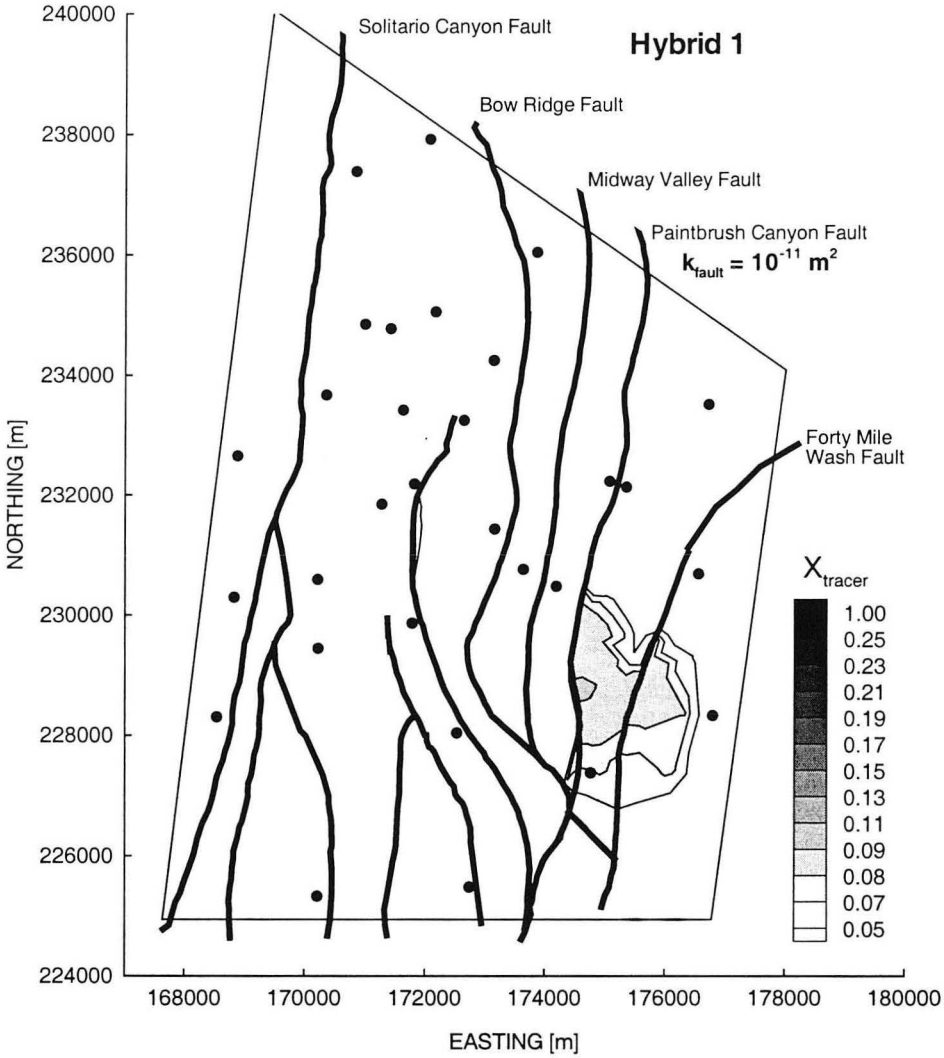


Figure 7.18. Flow visualization tracer at the water table after 50 years in the Hybrid 1 model.

### 7.9.2 Hybrid 2

In the Hybrid 2 model the Iron Ridge, Bow Ridge, Midway Valley and Paintbrush Canyon Fault are modeled as high permeability fault zones, while the remaining faults are displacement-only faults. Permeability of the Bow Ridge Fault is $1.2 \times 10^{-11}$ m$^2$, which is based on air injection tests in an unsaturated section of the Bow Ridge Fault (LeCain, 1998).

Figure 7.19 shows the steady-state water table for the Hybrid 2 model. The corresponding RMS is 0.179. Figures 7.20 through 7.22 show that the flow field is similar to the high permeability faults model. In addition, Figure 7.21 shows that both vertical and lateral flow occurs within the high permeability Bow Ridge Fault.

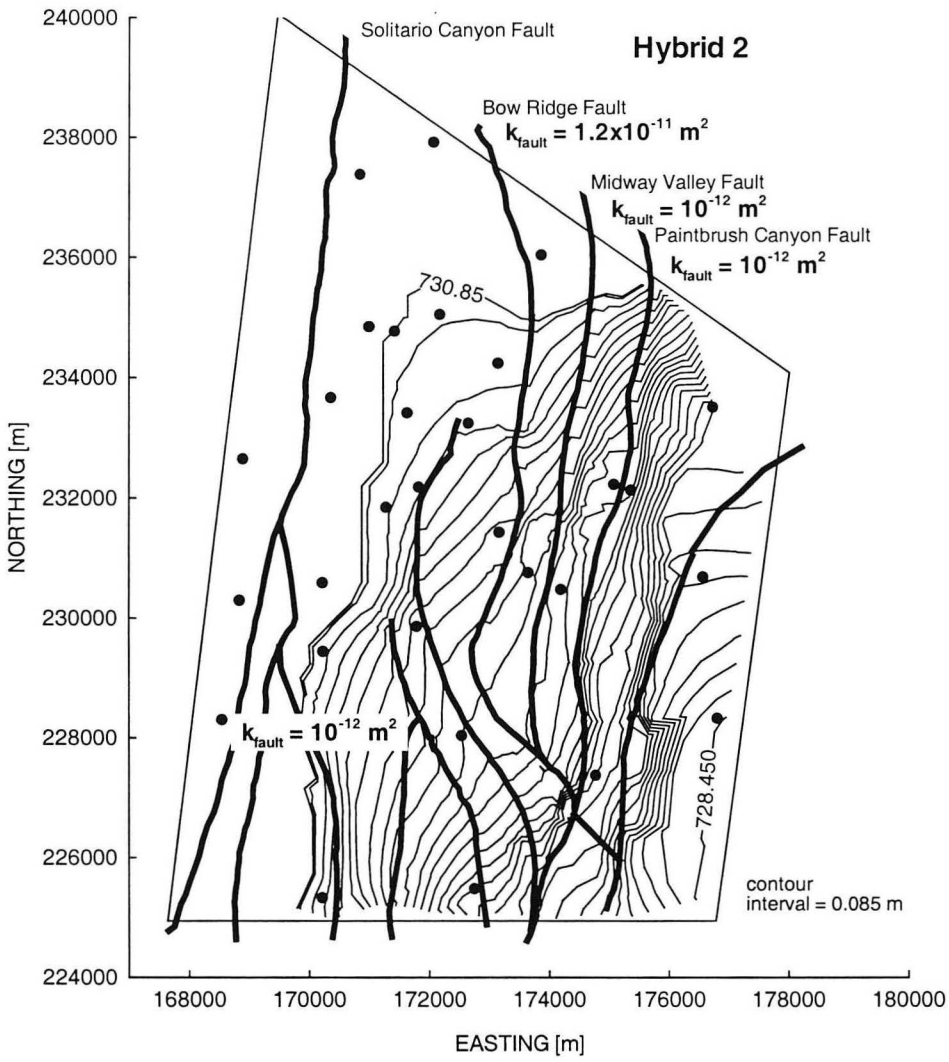


Figure 7.19. Steady-state water table in the Hybrid 2 model.

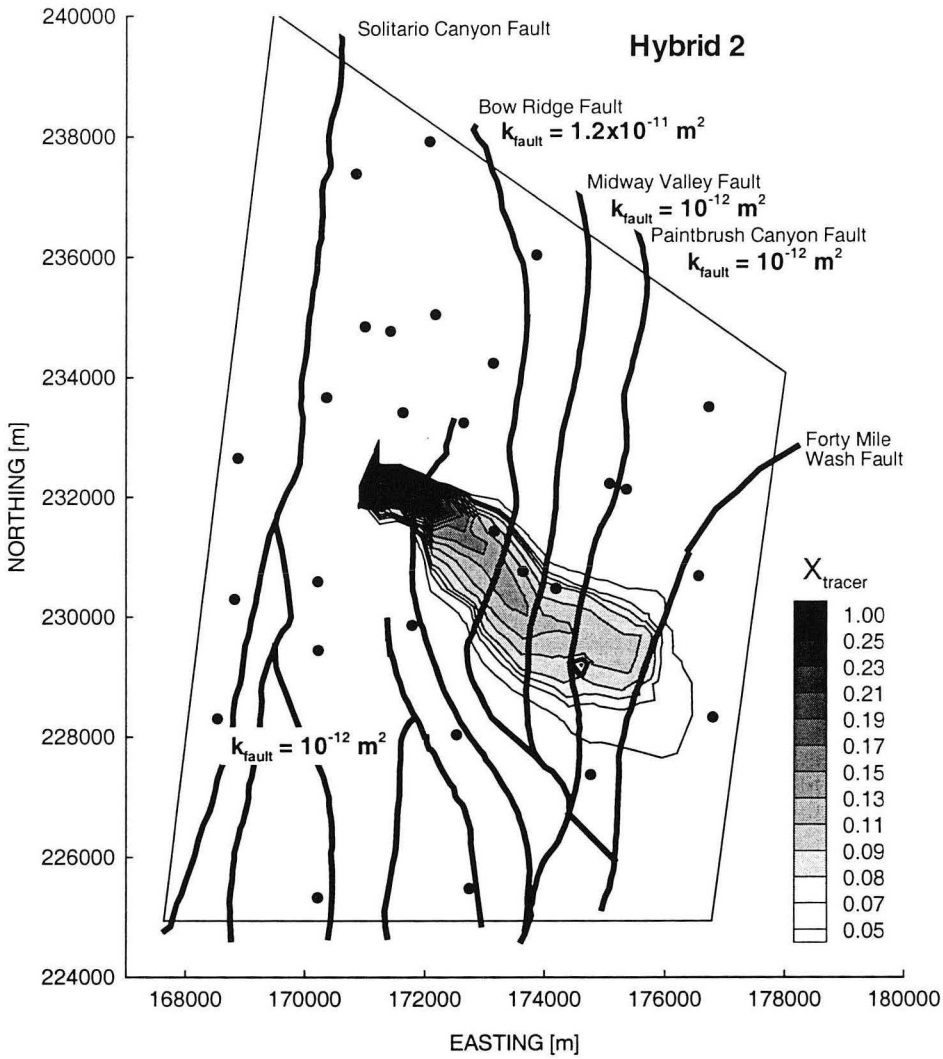


Figure 7.20. Flow visualization tracer in the central Bullfrog Tuff after 50 years in the Hybrid 2 model.

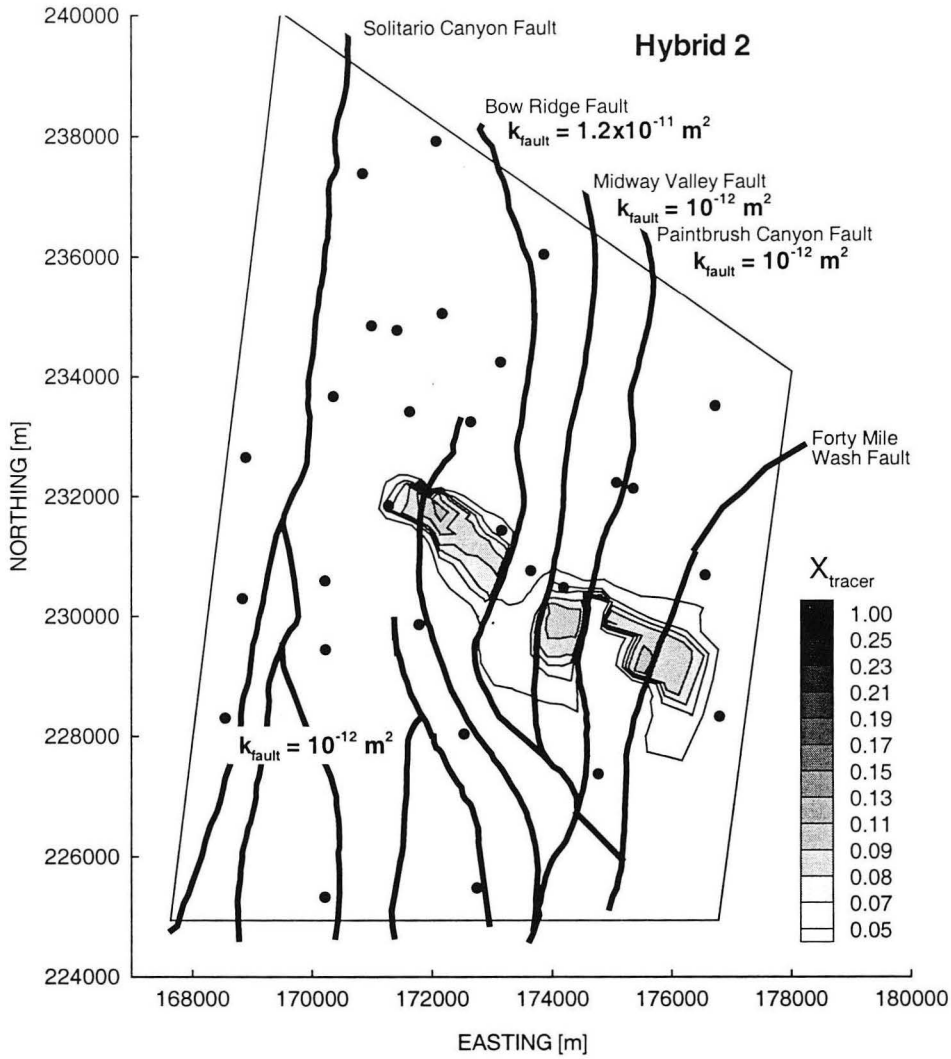


Figure 7.21. Flow visualization tracer in the central Prow Pass Tuff after 50 years in the Hybrid 2 model.

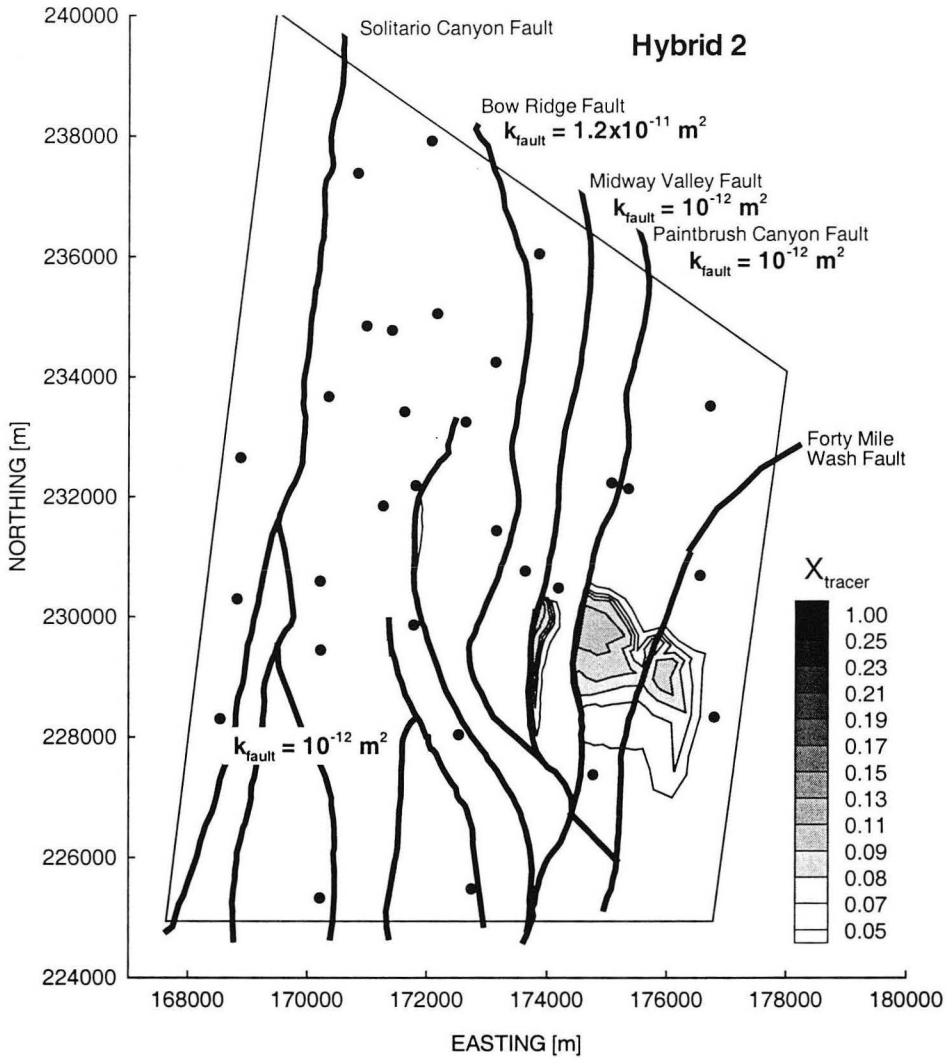


Figure 7.22. Flow visualization tracer at the water table after 50 years in the Hybrid 2 model.

# 8. Discussion and Recommendations

## 8.1 Purpose and Development of the 3-D Saturated Zone Flow Model

A three-dimensional numerical model of the saturated zone at Yucca Mountain, Nevada was developed to study the effects of the complex hydrogeologic structure on groundwater flow. The full 3-D flow model has 23 layers, and 11 faults are modeled explicitly. There are 57,153 grid blocks and 199,854 connections. The model is complex because it represents dipping geologic units which have variable thicknesses and orientations, and which have a layered permeability distribution due to differing rock welding characteristics. Also, the site is pervasively faulted, which results in large-scale heterogeneities due to the displacement of geologic units.

The model is used to test current hypotheses of fault effects on groundwater flow and transport at Yucca Mountain. Specifically, one hypothesis suggests that water from a deep carbonate aquifer upwells to the water table through high permeability fault zones. Such a process could restrict the vertical dispersion of contaminants beneath the water table. Another hypothesis is that relatively large lateral head gradients are due to low permeability faults.

More generally, the model is an investigative tool to gain understanding of groundwater flow and transport behavior in faulted formations like those at Yucca Mountain. With regards to Yucca Mountain, greater understanding serves to reduce the level of uncertainty of the degree to which the saturated zone will act as a natural barrier to contaminants. The model presented here is unique, both in the way it is discretized and in

the level of hydrogeologic detail that is represented. It is designed for use with the TOUGH2 simulation code (Pruess, 1987; Pruess, 1991a; Pruess *et al.*, 1996), which can simulate flow in a mesh composed of irregularly shaped grid blocks. These meshes facilitate realistic representation of geologic features, which are themselves irregular. Individual hydrogeologic layers and the displacement of these layers are modeled explicitly. That is, each dipping and variable thickness hydrogeologic layer is represented by a layer of dipping grid blocks. This discretization properly represents the lateral continuity of individual layers. Hydrogeologic layers on the opposite sides of a fault are connected by a fault grid block that has a thickness equal to the distance over which adjacent layers abut each other. The use of fault grid blocks enables representation of a fault with no internal zone (displacement-only fault), or one that also has a discrete width fault zone. Finally, fault displacement varies along strike from zero to more than 300 m.

Discretization of hydrogeologic model layers is based on all available saturated zone data. First, a detailed 3-D geologic model of Yucca Mountain (Clayton *et al.*, 1997) was used to discretize geologic units and faults. This geologic model was constructed using data from surface geologic mapping and measured sections at outcrops, lithologic logs, and seismic, gravity, and magnetic profiles. Because the flow model is based on this model, it implicitly incorporates this data. The 3-D geologic model has 35 geologic layers and 35 faults which have variable dip and offset along fault strike. It was the most comprehensive geologic model of the site when the flow model was constructed. Hydrologic data in the saturated zone is sparse. Lithologic, hydraulic, and geophysical data for the saturated zone was carefully reviewed to develop a conceptual model and

define the hydrogeologic properties of the formation. Some unsaturated zone data was also used. The conceptual model is the basis for model discretization; normal faults are represented because they have the greatest offset and are laterally continuous for tens of kilometers, and geologic units are subdivided to reflect the vertical permeability variation.

## 8.2 Summary of Findings

Fridrich *et al.* (1994) proposed the upwelling hypotheses, citing the presence of upward hydraulic gradients and the relatively high water table temperature along the Solitario Canyon Fault. A 2-D heat conduction simulation shows that relatively high water table temperatures along the Solitario Canyon Fault can result from variation of thermal conductivity and thicknesses of geologic units only. Furthermore, high water table temperatures were misinterpreted. A high water table temperature results from advection from discrete permeable layers that intersect the borehole. The moderate gradient across the Solitario Canyon Fault can be explained by a displacement-only or low permeability fault, not by a high permeability fault, which would enable such upwelling. These 2-D simulations therefore show that vertical gradients and upwelling from the Carbonate Aquifer through the Solitario Canyon Fault is unlikely.

In general, upward vertical flow will occur in the saturated zone in the absence of any hydraulic connection to the Carbonate Aquifer. The measured vertical gradients in the Lower Volcanic Aquifer and Lower Volcanic Confining Unit east of the repository are defined by vertical head differences that are less than 26 cm, except in borehole b#1, where it is approximately 1 m. The difference between water table elevation and heads at

depth in the calibrated displacement-only and high permeability faults model is on the order of tens of centimeters, and vertical gradients are present in the 3-D models as well. Yet, none of these models included flow from the Carbonate Aquifer. Instead, the models show that upwelling can occur in the presence of any one or a combination of the following features: spatial variability of permeability, fault displacements, and fault zones. For example, a 2-D simulation using the displacement-only faults model shows that upward flow occurs near the Dune Wash Fault because the high permeability Prow Pass and Bullfrog Tuff are present near the water table there. Similarly, upward flow occurs east of Paintbrush Canyon Fault because the high permeability Topopah Spring Tuff is present near the water table there.

Water is diverted upwards at down-to-the-west displacement-only faults because higher permeability units abut lower permeability units on the east side of a fault, groundwater flows to the east, and permeability is relatively low in deeper units. Thus, contaminants that percolate vertically from the repository can flow into the Bullfrog and Prow Pass Tuff and then beneath the water table within these high permeability layers which dip to the east. As a result, these contaminants could end up hundreds of meters beneath the water table downgradient.

Water flowing into a high permeability fault zone will be channeled vertically and will then flow into high permeability layers on the adjacent side of the fault. For example, water originating at the base of the Tram Tuff could be channeled several hundred meters upwards in the Dune Wash Fault zone and then into the Bullfrog Tuff. If this occurs at

other faults downgradient, it could enhance contaminant dilution because fresh water is introduced into the Lower Volcanic Aquifer. More significantly, high permeability fault zones act to hydraulically connect displaced and high permeability layers. As a result, water flows from one layer into several high permeability layers on the eastern side of a fault. If contaminants percolate vertically into the Bullfrog Tuff, this results in vertical dispersion downgradient which is greater than that in a displacement-only faults model. However, the effects of a particular fault type cannot be generalized; vertical dispersion may be relatively large or small depending on the location where the contaminant reaches the water table. Whereas high permeability faults cause significant vertical dispersion when the contaminants percolate into the Lower Volcanic Aquifer below the repository, vertical dispersion is inhibited if the contaminants are diverted eastward above the Upper Volcanic Confining Unit in the unsaturated zone. Under this condition, contaminants will enter the water table where the top of this unit intersects the water table. They will then flow near the water table if there are high permeability fault zones because of the combined effect of upwelling at faults and the presence of the high permeability Topopah Spring Tuff downgradient. A similar behavior is observed for displacement-only faults, although the vertical dispersion is slightly larger because no direct upwelling occurs within faults.

Both the 2-D and 3-D models cannot be calibrated when all faults are assigned a permeability of $10^{-14}$ $m^2$ or less. Some fault zones are likely to be low permeability features due to secondary mineralization, for example, but a general definition for faults as low permeability features is not warranted.

A large-scale permeability heterogeneity results from the superposition of dipping units and fault displacement, which is as much as 350 m. Large-scale channeling and dispersion is caused by this heterogeneity. For example, large-scale channeling can occur in the presence of displacement-only faults. Since displacement is less in some areas than in others, groundwater from a high permeability layer will flow sub-parallel to a fault where there is large displacement, and hence contact between higher to lower permeability layers. It will then cross the fault where the displacement is less and the higher permeability units are therefore continuous. The 3-D simulation of a displacement-only faults model showed that groundwater flowed for several kilometers southward and then eastward through a zone with small displacement. Large-scale dispersion can occur further downgradient due to flow around a low permeability zone.

The head gradient in hydrogeologic layers at depth can be significantly different than the direction of the water table gradient, indicating that the direction of contaminant flow can not be inferred from the water table gradient. In contrast, groundwater in a high permeability faults model flows in the direction of the water table gradient because of the effective continuity of high permeability layers. This suggests that a 2-D model is sufficient to simulate flow in a formation where the fault permeability is high relative to the formation permeability.

Analytic models cannot describe how contaminants spread on a scale equal to that of the saturated zone flow model. A particularly interesting phenomenon that is due to the complex structure is the presence of upgradient-source contaminants at isolated locations

near the water table downgradient, even when the source is at the water table. This is due to flow along dip, upwelling of waters at faults, and lateral flow due to variation of fault displacement along strike, as described above. This distribution is not predicted by analytic or 2-D numerical models.

## 8.3 Future Work

### 8.3.1 Stochastic Modeling

Although the flow model represents the hydrogeologic structure explicitly, it does have some idealized properties. In particular, the permeability and width of a fault is constant with depth and along strike, and each hydrogeologic layer has a homogeneous permeability. A variable permeability distribution within each layer and in the faults may result in a more direct flow downgradient because the contrasts in permeably at faults would not persist to distances of kilometers or more, for example. Stochastic simulations would be a systematic way to account for variations of these properties. However, the spatial variability of permeability would be a guess at best due to the lack of data in the saturated zone. Still, a range of estimates would provide a broader description of the effects of the faulted structure on flow and transport. A random permeability field would be best represented using a mesh with equal size grid blocks. The current model could be further discretized so that grid blocks are approximately the same size.

### 8.3.2 Calibration to Pumping Test Data

Calibration to hydraulic head data is non-unique. As for the 3-D model described in this work, multiple combinations of fault types and layer permeability distributions can be

used to calibrate the model. Therefore, additional calibration criteria are needed to constrain the range of probable formation properties. Calibration to pumping test data should be pursued because the model was discretized to enable simulation of pumping tests, and because reliable data is available from pumping tests at the c-holes. Tests in May, 1998 included measurement of drawdown transients in 4 boreholes that are as far as 3.5 km from the c-holes (Geldon *et al.*, 1997). Given the number of adjustable parameters, numerical inversion is the only viable method to calibrate the model to this data. ITOUGH2 (Finsterle, 1999) is based on the TOUGH2 code and is capable of parameter estimation (inversion), sensitivity analysis, and uncertainty propagation analysis.

Forward modeling should be performed prior to data inversion. Pumping test simulations of different fault types and layer permeability distributions will show the characteristic drawdown transients for different models in general. Comparison to data will therefore provide an initial conceptual model, thereby constraining the number and range of adjustable properties in the inversion. As an example, Figures 8.1 through 8.4 show different drawdown responses for different fault models. Pumping is at the c-holes and the drawdown transients are shown for a borehole 150 m north of the c-holes and in two boreholes to the east and west. These simulations were performed using a 2-D model, although the full model would be used for calibration.

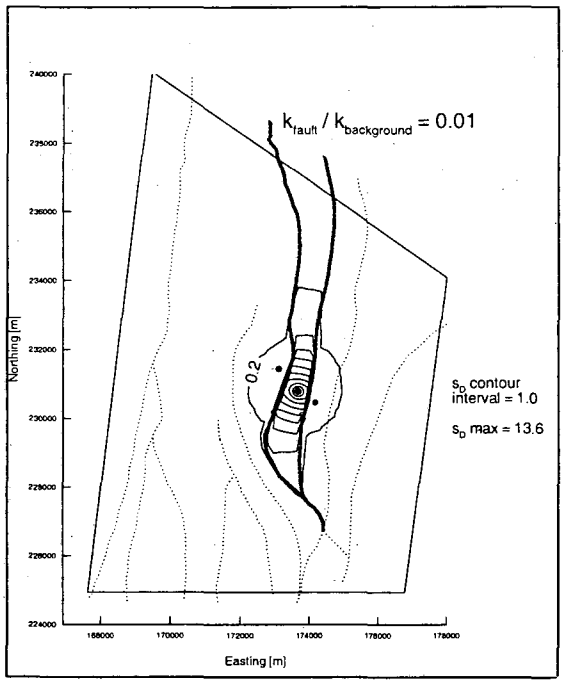


Figure 8.1. Dimensionless drawdown for $k_f/k_b = 0.01$.

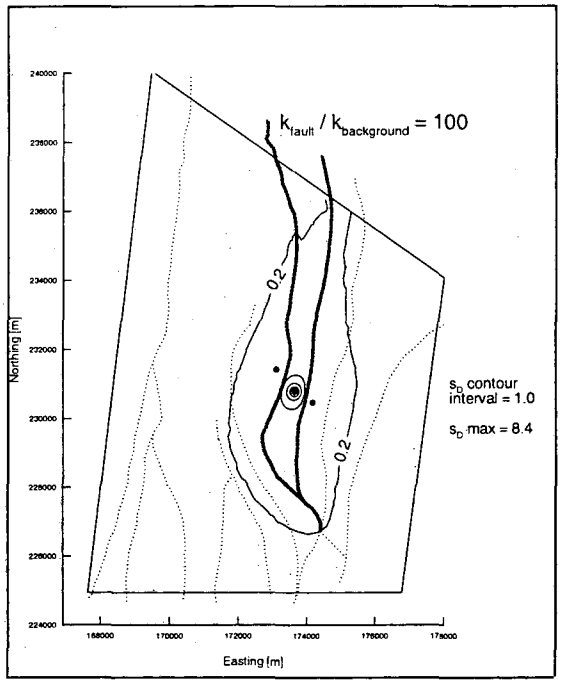


Figure 8.2. Dimensionless drawdown for $k_f/k_b = 10$.

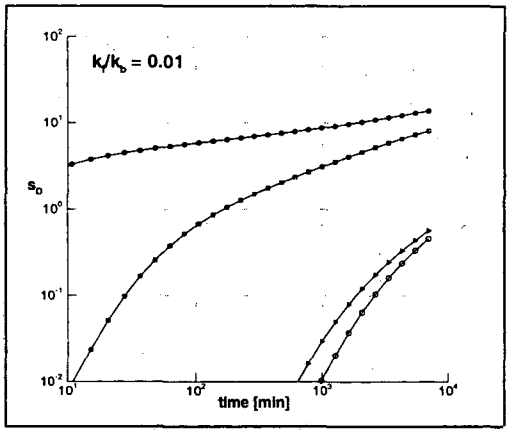


Figure 8.3. Dimensionless drawdown vs. time for $k_f/k_b = 0.01$. Explanation: dot=pump well; square=center well; triangle=eastern well; circle=western well.

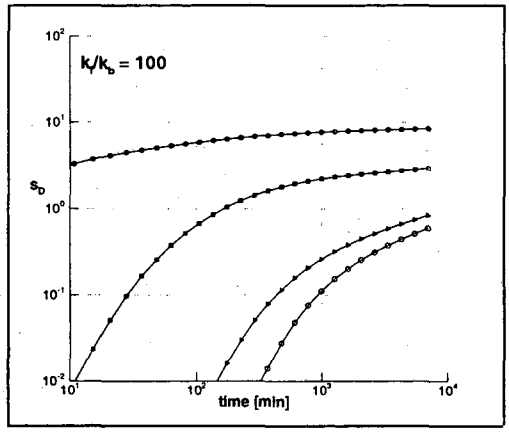


Figure 8.4. Dimensionless drawdown vs. time for $k_f/k_b = 10$. Explanation: dot=pump well; square=center well; triangle=eastern well; circle=western well.

### 8.3.3 Particle Tracking

The basis of a new technique to calculate flow paths in models with irregular meshes was developed during the course of this study (Appendix A). This new development is a significant contribution, since the technique can be used to define flow pathways precisely, whereas numerical dispersion contributes to spreading of tracers along their flow pathways. A preliminary algorithm to implement this technique was written and used for illustration, but the technique was not used in general because the algorithm it is not fully developed. Although the flow visualization tracer illustrated the flow patterns sufficiently for the purposes of this work, future work should use this new technique to investigate flow behavior.

## REFERENCES

Ahlers, C. F., C. Shan, C. Haukwa, A. J. B. Cohen, and G. S. Bodvarsson, Calibration and prediction of pneumatic response at Yucca Mountain, Nevada, using the LBNL/USGS Three-Dimensional, Site-Scale Model of the Unsaturated Zone, Yucca Mountain Project Level 4 Milestone OB12M, Lawrence Berkeley National Laboratory, Berkeley, CA, 1996.

Anderson, L. A., Results of rock property measurements made on core samples from Yucca Mountain boreholes, Nevada Test Site, Nevada. Part 1. Boreholes UE25A-4, -5, -6, and -7. Part 2. Borehole UE25P#1, Open-File Report 90-474, U.S. Geological Survey, Denver, CO, 1991.

Anderson, L. A., Water permeability and related rock properties measured on core samples from the Yucca Mountain USW GU-3/G-3 and USW G-4 boreholes, Nevada Test Site, Nevada, Open-File Report 92-201, U.S. Geological Survey, Denver, CO, 1994.

Anderson, M. P., and W. W. Woessner, *Applied Groundwater Modeling, Simulation of Flow and Advective Transport*, Academic Press, Inc., San Diego, CA, 1992.

Arnold, B. W., and S. A. McKenna, Influences of aquifer heterogeneity and channelization on saturated-zone flow and transport at Yucca Mountain: Sub-site-scale modeling results, in *High-Level Radioactive Waste Management Conference*, Las Vegas, NV, 1998.

Arnold, B. W., A. M. Parsons, and J. H. Gauthier, Saturated flow and transport: preliminary draft section 2.9 of TSPA-VA technical bases document (base case analyses), Yucca Mountain Site Characterization Project Milestone SLX03M3, TRW Environmental Safety Systems, Inc., Las Vegas, NV, 1998.

Aurenhammer, F., Voronoi Diagrams - A survey of a fundamental geometric data structure, *ACM Computing Surveys*, *23*(3), 335-404, 1991.

Bear, J., C. F. Tsang, and G. Marsily, de, *Flow and Contaminant Transport in Fractured Rock*, Academic Press, Inc., San Diego, 1993.

Benson, L. V., and P. W. McKinley, Chemical composition of ground water in the Yucca Mountain area, Nevada, 1971-84, Open-File Report 83-853, U.S. Geological Survey, Denver, CO, 1985.

Bentley, C. B., Geohydrologic data for test well USW G-4, Yucca Mountain area, Nye County, Nevada, Open-File Report 84-063, U.S. Geological Survey, Denver, CO, 1984.

Bodvarsson, G. S., T. M. Bandurraga, and Y. S. Wu, eds., The site-scale unsaturated zone model of Yucca Mountain, Nevada, for the viability assessment, LBNL-40376, Lawrence Berkeley National Laboratory, Berkeley, CA, 1997.

Brodsky, N. S., M. Riggins, J. Connolly, and P. Ricci, Thermal expansion, thermal conductivity, and heat capacity measurements for boreholes UE25 NRG-4, UE25 NRG-5, USW NRG-6, and USW NRG 7/7a, SAND 95-1955, Sandia National Laboratories, Albuquerque, NM, 1997.

Carr, W. J., F. M. Byers, Jr., and P. P. Orkild, Stratigraphic and volcano-tectonic relations of Crater Flat tuff and some older volcanic units, Nye County, Nevada, Professional Paper 1323, U.S. Geological Survey, Washington, D.C., 1986.

Clayton, R. W., W. P. Zelinski, and C. A. Rautman, ISM2.0: A 3D Geologic Framework and Integrated Site Model of Yucca Mountain, B00000000-01717-5700-00004, Civilian Radioactive Waste Management System Management & Operating Contractor, Las Vegas, NV, 1997.

Craig, R. W., Hydrogeology of Borehole USW G-2, transmittal of deliverable 3GRG103M-Letter Report to Susan Jones (DOE), MOL.19960415.0350, Sept 1995.

Craig, R. W., and R. L. Reed, Geohydrology of rocks penetrated by test well USW H-6, Yucca Mountain, Nye County, Nevada, Water-Resources Investigations Report 89-4025, U.S. Geological Survey, Denver, CO, 1991.

Craig, R. W., and J. H. Robison, Geohydrology of rocks penetrated by test well UE-25p#1, Yucca Mountain Area, Nye County, Nevada, Water-Resources Investigations Report 84-4248, U.S. Geological Survey, Denver, CO, 1984.

Czarnecki, J. B., G. M. O'Brien, P. H. Nelson, J. H. Sass, J. W. Bullard, and A. L. Flint, Is there perched water under Yucca Mountain in borehole USW G-2?, *Eos Trans. AGU*, *75*(44), 249-250, 1994.

Day, W. C., C. J. Potter, D. S. Sweetkind, R. P. Dickerson, and C. A. San Juan, Bedrock geologic map of the central block area, Yucca Mountain, Nye County, Nevada, Administrative Report, U.S. Geological Survey, Denver, CO, 1996.

Dickerson, R. P., and R. W. Spengler, Structural character of the northern segment of the Paintbrush Canyon fault, Yucca Mountain, Nevada, in *Fifth Annual International Conference on High Level Radioactive Waste Management*, pp. 2367-2372, American Nuclear Society and American Society of Civil Engineers, Las Vegas, NV, 1994.

Edwards, A. L., TRUMP: A Computer Program for Transient and Steady State Temperature Distributions in Multidimensional Systems, National Technical Information Service, National Bureau of Standards, Springfield, VA, 1972.

Erickson, J. R., and R. K. Waddell, Identification and characterization of hydrologic properties of fractured tuff using hydraulic and tracer tests - test well USW H-4, Yucca Mountain, Nye County, Nevada, Water-Resources Investigations Report 85-4066, U.S. Geological Survey, Denver, CO, 1985.

Ervin, E. M., R. R. Luckey, and D. J. Burkhardt, Revised potentiometric-surface map, Yucca Mountain and vicinity, Nevada, 93-4000, U.S. Geological Survey, Denver, Colorado, 1994.

Faunt, C. C., Effect of faulting on ground-water movement in the Death Valley Region, Nevada and California, Water-Resources Investigations Report 95-4132, U.S. Geological Survey, Denver, CO, 1997.

Finsterle, S., ITOUGH2 user's guide, LBNL-40400, Lawrence Berkeley National Laboratory, Berkeley, CA, 1999.

Flint, A. L., J. A. Hevesi, and L. E. Flint, Conceptual and numerical model of infiltration for the Yucca Mountain area, Nevada, Yucca Mountain Site Characterization Project Milestone 3GU1623M, submitted for publication as a Water-Resources Investigations Report, U.S. Geological Survey, Denver, CO, 1996 (unpublished).

Forster, C., and L. Smith, The influence of groundwater flow on thermal regimes in mountainous terrain: a model study, *J. Geophys. Res.*, *94*, 9439-9451, 1989.

Fridrich, C. J., D. C. Dobson, and W. W. Dudley, Jr., A geologic hypothesis for the large gradient under Yucca Mountain, Nevada, *Eos Trans. AGU*, *72*(17), 121, 1991.

Fridrich, C. J., W. W. Dudley, Jr., and J. S. Stuckless, Hydrogeologic analysis of the saturated-zone ground-water system under Yucca Mountain, Nevada, *J. Hydrol.*, *154*, 133-168, 1994.

Geldon, A. L., Preliminary hydrogeologic assessment of boreholes UE-25c #1, UE-25c #2, and UE-25c #3, Yucca Mountain, Nye County, Nevada, Water-Resources Investigations Report 92-4016, U.S. Geological Survey, Denver, CO, 1993.

Geldon, A. L., Results and interpretation of preliminary aquifer tests in boreholes UE-25c #1, UE-25c #2, and UE-25c #3, Yucca Mountain, Nye County, Nevada, Water-Resources Investigations Report 94-4177, U.S. Geological Survey, Denver, CO, 1996.

Geldon, A. L., A. M. A. Umari, M. F. Fahy, J. D. Earle, J. M. Gemmell, and J. Darnell, Results of hydraulic and conservative tracer tests in Miocene tuffaceous rocks at the C-Hole Complex, 1995 to 1997, Yucca Mountain, Nye County, Nevada, Yucca Mountain Site Characterization Milestone Report SP23PM3, U.S. Geological Survey, Denver, CO, 1997.

Geomatrix Consultants Incorporated, Saturated Zone Flow and Transport Expert Elicitation Project, prepared for U.S. Department of Energy, Yucca Mountain Site Characterization Office, WBW 1.2.5.7, San Francisco, CA, 1997.

Goode, D. J., Particle tracking interpolation in block-centered finite-difference groundwater flow models, *Water Resour. Res.*, *26*(5), 925-940, 1992.

Ho, C. K., N. D. Francis, B. W. Arnold, Y. Xiang, S. A. McKenna, S. Mishra, G. E. Barr, S. J. Altman, X. H. Yang, and R. R. Eaton, Thermo-hydrologic modeling of the potential repository at Yucca Mountain including the effects of heterogeneities and alternative conceptual models of fractured porous media, Yucca Mountain Site Characterization Level 3 Milestone T6536, Sandia National Laboratory, Albuquerque, NM, 1996.

Kwicklis, E. M., Radiocarbon data and analysis, presented at the Saturated Zone Flow and Transport Expert Elicitation Project, San Francisco, CA, Geomatrix Consultants Incorporated, prepared for U.S. Department of Energy, Yucca Mountain Site Characterization Office, WBW 1.2.5.7, San Francisco, CA, 1997.

Lahoud, R. G., D. H. Lobmeyer, and M. S. Whitfield, Jr., Geohydrology of volcanic tuff penetrated by test well UE-25b#1, Yucca Mountain, Nye County, Nevada, Water-Resources Investigations Report 84-4253, U.S. Geological Survey, Denver, CO, 1984.

LeCain, G. D., Air-injection testing in vertical boreholes in welded and nonwelded tuff, Yucca Mountain, Nevada, Water-Resources Investigations Report 96-4262, U.S. Geological Survey, Denver, CO, 1997.

LeCain, G. D., Results from air-injection and tracer testing in the upper Tiva Canyon, Bow Ridge Fault, and upper Paintbrush contact alcoves of the Exploratory Studies Facility, Water-Resources Investigations Report 98-4058, U.S. Geological Survey, Denver, CO, 1998.

Lobmeyer, D. H., Geohydrology of rocks penetrated by test well USW G-4, Yucca Mountain, Nye County, Nevada, Water-Resources Investigations Report 86-4015, U.S. Geological Survey, Lakewood, CO, 1986.

López, D. L., and L. Smith, Fluid flow in fault zones: analysis of the interplay of convective circulation and topographically driven groundwater flow, *Water Resour. Res.*, *31*(6), 1489-1503, 1995.

López, D. L., and L. Smith, Fluid flow in fault zones: influence of hydraulic anisotropy and heterogeneity on the fluid flow and heat transfer regime, *Water Resour. Res.*, *32*(10), 3227-3235, 1996.

Lu, N., A semianalytical method of path line computation for transient finite-difference groundwater flow models, *Water Resour. Res.*, *30*(8), 2449-2459, 1994.

Luckey, R., P. Tucci, C. Faunt, E. Ervin, W. Steinkampf, F. D'Agnese, and G. Patterson, Status of understanding of the saturated-zone ground-water flow system at Yucca Mountain, Nevada, as of 1995, Water-Resources Investigations Report 96-4077, U.S. Geological Survey, Denver, 1996.

MacDougall, H. R., Loss of drilling fluid, hole USW-G1, Yucca Mountain Nevada Test Site, NNA.900731.0192, Nuclear Waste Engineering Projects, Sandia National Laboratories, Albuquerque, NM, date unknown.

Maldonado, F., and S. L. Koether, Stratigraphy, structure, and some petrographic features of tertiary volcanic rocks at the USW G-2 drill hole, Yucca Mountain, Nye County, Nevada, Open-File Report 83-732, U.S. Geological Survey, Denver, CO, 1983.

Mattson, S. R., Yucca Mountain Project Draft Stratigraphic Compendium, Woodward Clyde Federal Services, Las Vegas, NV, 1994.

Matuska, N. A., The relationship of the Yucca Mountain repository block to the regional groundwater system-A geochemical model, Master's thesis, University of Nevada at Las Vegas, 1989.

Molz, F. J., R. H. Morin, A. E. Hess, J. G. Melville, and O. Guven, The impeller meter for measuring aquifer permeability variations: evaluation and comparison with other tests, *Water Resour. Res.*, *25*(7), 1677-1683, 1989.

Moyer, T. C., and J. K. Geslin, Lithostratigraphy of the Calico Hills Formation and Prow Pass Tuff (Crater Flat Group) at Yucca Mountain, Nevada, Open-File Report 94-460, U.S. Geological Survey, Denver, CO, 1995.

Narasimhan, T. N., and P. A. Witherspoon, An integrated finite difference method for analyzing fluid flow in porous media, *Water Resour. Res.*, *12*(1), 57-64, 1976.

O'Brien, G. M., Analysis of aquifer tests conducted in borehole USW G-2, 1996, Yucca Mountain, Nevada, Water-Resources Investigations Report 98-4063, U.S. Geological Survey, Denver, CO, 1998.

Palagi, C. L., Generation and application of Voronoi grid to model flow in heterogeneous reservoirs, Ph.D. thesis, Stanford University, Palo Alto, CA, 1992.

Plisga, G. J., Temperature in wells, in *Petroleum Engineering Handbook*, edited by H.B. Bradley, Society of Petroleum Engineers, Richardson, TX, 1987.

Pollock, D. W., Semianalytical computation of path lines for finite-difference models, *Ground Water*, *26*(6), 743-750, 1988.

Pruess, K., TOUGH User's Guide, LBL-20700, Lawrence Berkeley National Laboratory, Berkeley, CA, 1987.

Pruess, K., TOUGH2 - A general-purpose numerical simulator for multiphase fluid and heat flow, LBL-29400, Lawrence Berkeley National Laboratory, Berkeley, CA, 1991a.

Pruess, K., EOS7, An equation-of-state module for the TOUGH2 simulator for two-phase flow of saline water and air, LBL-31114, Lawrence Berkeley National Laboratory, Berkeley, CA, 1991b.

Pruess, K., and T. N. Narasimhan, A practical method for modeling fluid and heat flow in fractured porous media, *Soc. Petro. Eng. J.*, *25*, 14-26, 1985.

Pruess, K., A. Simmons, Y. S. Wu, and G. Moridis, TOUGH2 software qualification, LBNL-38383, Lawrence Berkeley National Laboratory, Berkeley, CA, 1996.

Ritcey, A. C., Y. S. Wu, and G. S. Bodvarsson, Flow patterns below the repository horizon, *in* G.S. Bodvarsson, T.M. Bandurraga, and Y.S. Wu, eds., The Site-Scale Unsaturated-Zone Model of Yucca Mountain, Nevada, for the Viability Assessment, Chapter 22, Yucca Mountain Project Level 4 Milestone SP24UFM4, LBNL-40376, Lawrence Berkeley National Laboratory, Berkeley, CA, 1997.

Robison, J. H., Ground-water level data and preliminary potentiometric-surface maps, Yucca Mountain and vicinity, Nye County, Nevada, Water-Resources Investigations Report 84-4197, U.S. Geological Survey, Lakewood, CO, 1984.

Robison, J. H., and R. W. Craig, Geohydrology of rocks penetrated by test well USW H-5, Yucca Mountain, Nye County, Nevada, Water-Resources Investigations Report 88-4168, U.S. Geological Survey, Denver, CO, 1991.

Rush, F. E., W. Thordarson, and D. G. Pyles, Geohydrology of test well USW H-1, Yucca Mountain, Nevada, Water-Resources Investigations Report 84-4032, U.S. Geological Survey, Denver, CO, 1984.

Sass, J., A. Lachenbruch, W. Dudley, S. Priest, and R. Munroe, Temperature, thermal conductivity, and heat flow near Yucca Mountain, Nevada: some tectonic and hydrologic implications, Open-File Report 87-649, U.S. Geological Survey, 1988.

Sass, J. H., W. W. Dudley, Jr., and A. H. Lachenbruch, Regional thermal setting, *in* Oliver, H. W., Ponce, D. A., Hunter, W. C., Major results of geophysical investigations at Yucca Mountain and vicinity, southern Nevada, Open-File Report 95-74, pp. 199-218, U.S. Geological Survey., 1995.

Shan, C., and I. Javandel, Analytical solutions for solute transport in a vertical aquifer section, *J. Contam. Hydrol.*, *27*, 63-82, 1997.

Snyder, D. B., and W. J. Carr, Preliminary results of gravity investigations at Yucca Mountain and vicinity, southern Nye County, Nevada, Open-File Report 82-701, U.S. Geological Survey, 1982.

Sonnenthal, E. L., C. F. Ahlers, and G. S. Bodvarsson, Fracture and fault properties for the UZ Site-Scale Flow Model, *in* G.S. Bodvarsson, T.M. Bandurraga, and Y.S. Wu, eds., The Site-Scale Unsaturated-Zone Model of Yucca Mountain, Nevada, for the Viability Assessment, Chapter 7, Yucca Mountain Project Level 4 Milestone SP24UFM4, LBNL-40376, Lawrence Berkeley National Laboratory, Berkeley, CA, 1997.

Stuckless, J. S., J. F. Whelan, and W. C. Steinkampf, Isotopic discontinuities in ground water beneath Yucca Mountain, Nevada, in *High Level Radioactive Waste Management, Proceedings of the Second Annual International Conference*, pp. 1410-1415, American Nuclear Society, Las Vegas, NV, 1991.

Szymanski, J. S., Conceptual considerations of the Yucca Mountain groundwater system with emphasis on the adequacy of this system to accommodate a high-level nuclear waste repository, unpublished report available from the Department of Energy, Yucca Mountain Project Office, Las Vegas, NV, 1989.

Thordarson, W., Geohydrologic data and test results from well J-13, Nevada Test Site, Nye County, Nevada, Water-Resources Investigations Report 83-4171, U.S. Geological Survey, Denver, CO, 1983.

Thordarson, W., F. E. Rush, and S. J. Waddell, Geohydrology of test well USW H-3, Yucca Mountain, Nye County, Nevada, Water-Resources Investigations Report 84-4272, U.S. Geological Survey, Lakewood, CO, 1985.

TRW Environmental Safety Systems Incorporated, Total System Performance Assessment (TSPA) Peer Review Panel, peer review of the Total System Performance Assessment-Viability Assessment, third interim report, Las Vegas, NV, 1998.

Tucci, P., and D. J. Burkhardt, Potentiometric-surface map, 1993, Yucca Mountain and vicinity, Nevada, Water-Resources Investigations Report 95-4149, U.S. Geological Survey, Denver, CO, 1995.

U.S. Department of Energy, Site characterization plan, Yucca Mountain site, Nevada Research and Development Area, Nevada, U.S. Department of Energy Report DOE/RW-0199, 1988.

Voronoi, G., Nouvelles applications des parametres continus a la theorie des formes quadratiques, *J. Reine Angew. Math.*, *134*, 198-287, 1908.

Wilson, M. L., J. H. Gauthier, R. W. Barnard, G. E. Barr, H. A. Dockery, E. Dunn, R. R. Eaton, D. C. Guerin, N. Lu, M. J. Martinez, R. Nilson, C. A. Rautman, T. H. Robey, B. Ross, E. E. Ryder, A. R. Schenker, S. A. Shannon, L. H. Skinner, W. G. Halsey, J. Gansemer, L. C. Lewis, A. D. Lamont, I. R. Triay, A. Meijer, and D. E. Morris, Total-system performance assessment for Yucca Mountain-SNL second interation (TSPA-1993), SAND93-2675, Sandia National Laboratories, Albuquerque, NM, 1994.

Winograd, I. J., and W. Thordarson, Hydrogeologic and hydrochemical framework, south-central Great Basin, Nevada-California, with special reference to the Nevada Test Site, Professional Paper 712-C, U.S. Geological Survey, Denver, CO, 1975.

Wu, Y. S., A. Ritcey, E. L. Sonnenthal, T. M. Bandurraga, C. Haukwa, J. Fairley, G. Chen, J. H. Li, and G. S. Bodvarsson, Incorporation of perched water data into the UZ Site-Scale Model, Yucca Mountain Project Level 4 Milestone Report SP24UCM4, Lawrence Berkeley National Laboratory, Berkeley, CA, 1996.

Zyvoloski, G. A., B. A. Robinson, K. H. Birdsell, C. W. Gable, J. Czarnecki, K. M. Bower, and C. Faunt, Saturated zone radionuclide transport model, Yucca Mountain Site Characterizaton Project Milestone SP25CM3A, Los Alamos National Laboratory, Albuquerque, NM, 1997.

# APPENDIX A: 2-D Particle Tracking for Irregular Meshes

## A.1 Introduction

Numerical dispersion creates an artificial and enhanced spreading of a simulated solute plume. As a result, the true mechanical dispersion due to the system heterogeneity is exaggerated or masked and the pathways of source fluids are difficult to define. Particle tracking is a better method to define flow paths and travel times because it is not subject to numerical dispersion. Particle tracking requires the computation of streamlines that define the 2-D pathways of infinitesimally small fluid particles. Streamlines are commonly used to define the pathways of simulated contaminants in ground water systems (Anderson and Woessner, 1992). Tracer simulations were used to examine flow pathways in this study because current particle tracking schemes for finite-difference models are applicable to meshes with regular (rectilinear) grid blocks only. This section describes a new technique to properly calculate flow vectors in meshes with irregular grid blocks. Particle tracking can then be easily implemented using the calculated vector field. The new scheme can be used for future modeling of the saturated zone at Yucca Mountain and for other 2-D models with irregular grid blocks in general.

## A.2 Velocity Vector Calculation for Irregular Grid Blocks

Particle tracking algorithms calculate a flow vector using the simulated velocities at each grid block interface. The spatial distribution of velocity is defined via interpolation of the resultant velocity vector field. Linear interpolation is commonly used. This method solves for the pathlines by analytic means only and is not subject to numerical dispersion (e.g., Pollock, 1988). Other interpolation techniques are used less frequently (e.g.,

Goode, 1992; Lu, 1994). However, each method requires the grid block interface velocities as input. For regular grid blocks, a velocity vector is easily calculated because the grid block sides are orthogonal. Due to orthogonality, the $v_x$ or $v_y$ component of the resultant true vector is the summation of the $v_x$ and $v_y$ components from two orthogonal interfaces. Figure A.1a illustrates this relationship for an analogous case using fluid flux, $q$.

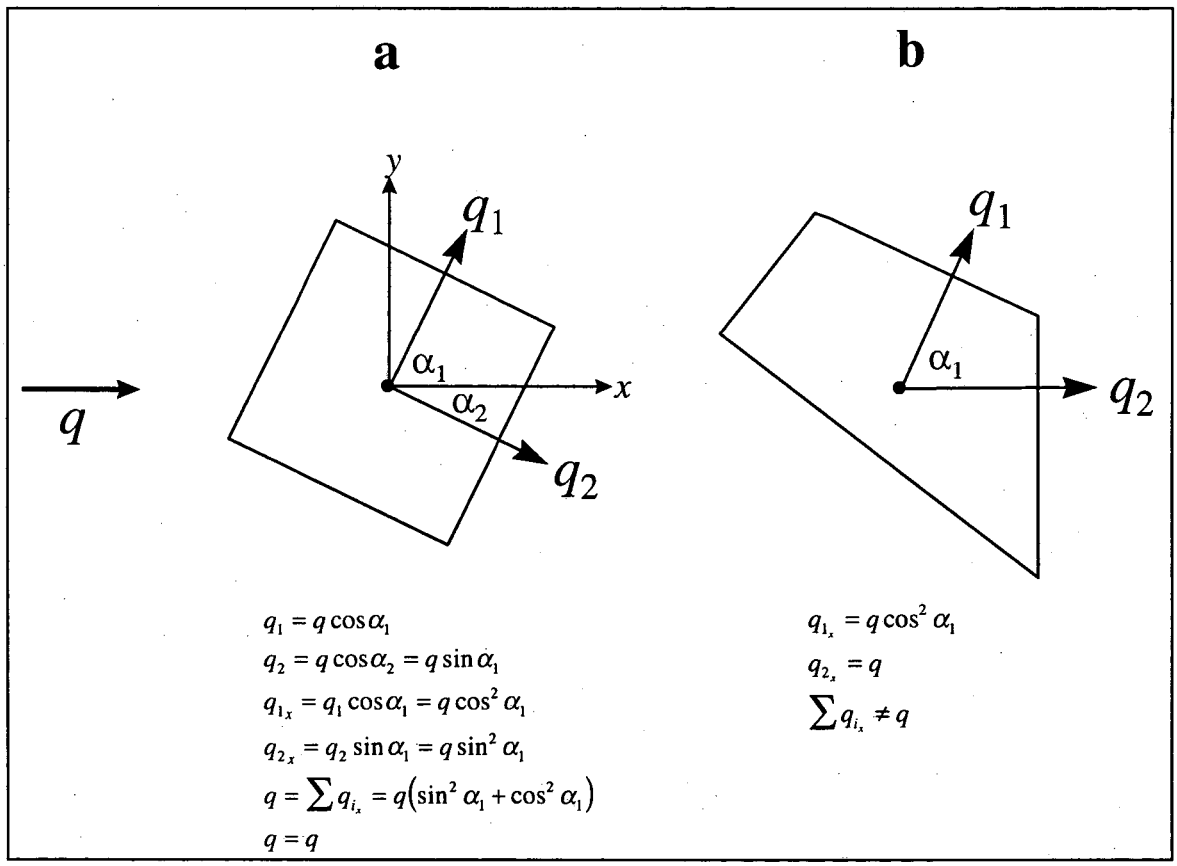


Figure A.1. Flux vector relationships for a) regular grid block; b) irregular grid block.

The interface areas of irregular grid blocks may not be orthogonal and the respective velocities do not sum to the true velocity vector. As shown in Figure A.1b, fluid moves out of the block through the two faces on the right side and the $q_x$ component of each

vector cannot be summed to equal the true flow vector. In addition, irregular grid blocks can have any number of sides greater than two. For these reasons, particle tracking schemes for finite-difference models have been limited to regular meshes.

As shown in this work, irregular grid blocks are more versatile and better suited to model complex hydrogeologic systems. For example, irregular grid blocks can be oriented such that a variable thickness and dipping stratigraphic layer is represented with a single layer of grid blocks. Meshes with regular grid blocks, however, would require a finer grid block discretization and therefore more grid blocks. Irregular grid blocks also enable sub-scaling within the model without requiring that the smaller discretization extends to the boundaries of the model.

### A.3 Mass Flux Identity for Irregular Grid Blocks

Consider the irregular grid block in Figure A.2 as part of a larger horizontal model. The sides of the grid block are defined by the polygon. The direction and magnitude of the true steady-state flux vector, $q$, for an irregular grid block can be calculated using (1) the simulated mass fluxes through each side; (2) the interface areas of the grid block sides and (3) the corresponding orientations of the nodal connections; (4) the grid block porosity and fluid density, and (5) an identity that relates the mass fluxes to the grid block interface areas.

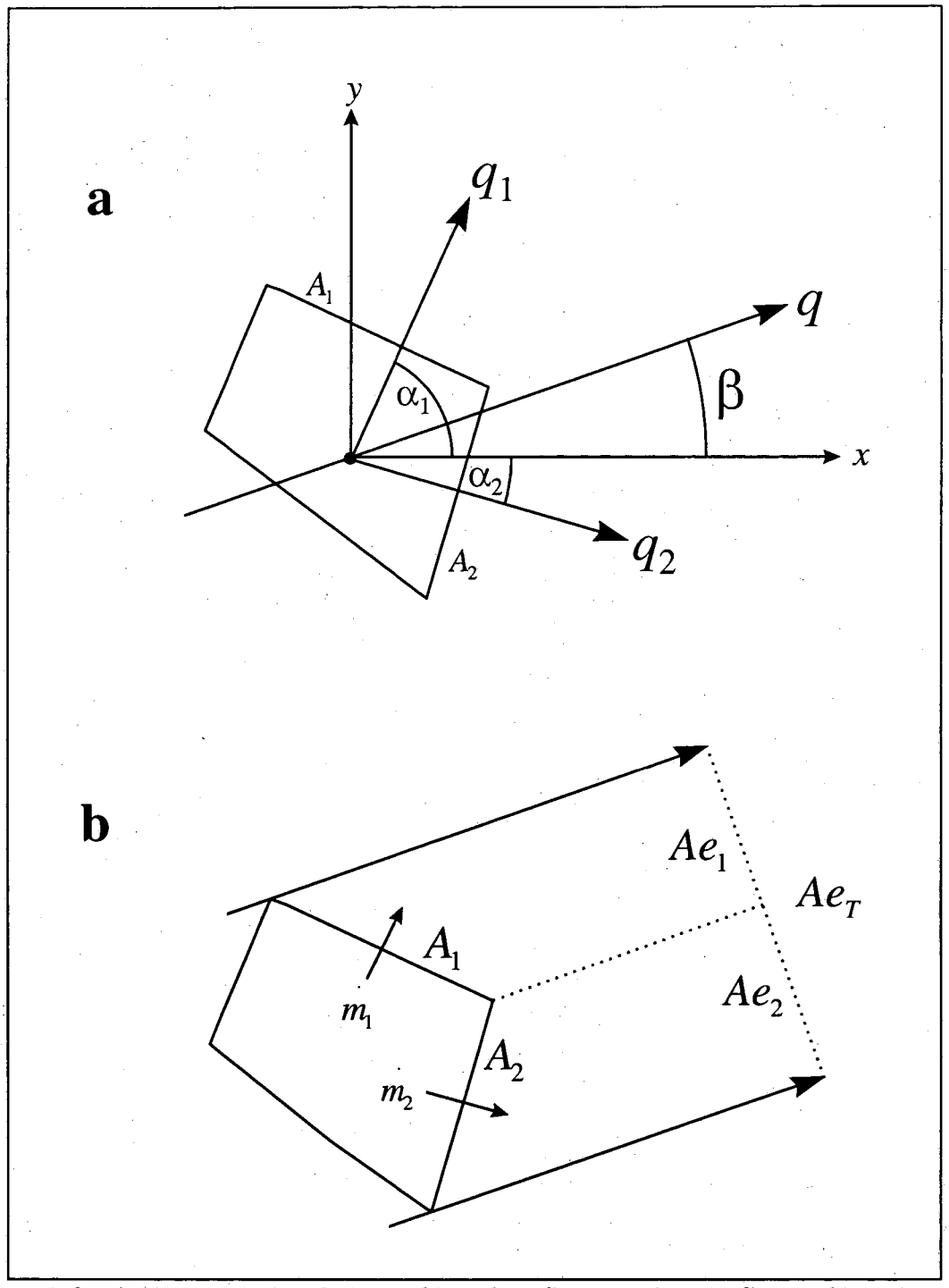


Figure A.2. a) trigonometric relations of interface fluxes to the true flux, $q$; b) projected areas of grid block interfaces.

Flow through the grid block in Figure A.2 is steady-state. Under this condition, the total mass flux, $m_T$, into the grid block is equal to the total mass flux out of the grid block. The following relationships are written for the outflow interfaces, although they can be written for the inflow interfaces as well.

The mass flux out of interface 1 is

$$m_1 = q_1 A_1 = q\cos(\alpha_1 - \beta)A_1, \tag{A.1}$$

where $A_1$ is the area of interface 1. Similarly,

$$m_2 = q_2 A_2 = q\cos(\beta - \alpha_2)A_2 \tag{A.2}$$

and

$$m_T = m_1 + m_2 = q\left[\cos(\alpha_1 - \beta)A_1 + \cos(\beta - \alpha_2)A_2\right]. \tag{A.3}$$

The fractional mass flux for side 1 is, for example

$$\frac{m_1}{m_T} = \frac{\cos(\alpha_1 - \beta)A_1}{\cos(\alpha_1 - \beta)A_1 + \cos(\beta - \alpha_2)A_2} \tag{A.4}$$

By definition, the mass flux per unit area, $q$ [kg m$^{-2}$ s$^{-1}$], through the region occupied by the grid block must equal the total mass flux, $m_T$ [kg s$^{-1}$], through the grid block divided by an effective area of the grid block, $Ae_T$ [m$^2$]:

$$q = \frac{m_T}{Ae_T} \tag{A.5}$$

Therefore,

$$Ae_T = \frac{m_T}{q} \tag{A.6}$$

Equation (A.6) also holds for each interface, *i*:

$$Ae_i = \frac{m_i}{q} \tag{A.7}$$

The effective area is a projection of the grid block in the direction of flow times the thickness of the grid block (Figure A.1):

$$Ae_1 = \cos(\alpha_1 - \beta)A_1 \tag{A.8}$$

and

$$Ae_2 = \cos(\beta - \alpha_2)A_2 \tag{A.9}$$

The total effective area is

$$Ae_T = \cos(\alpha_1 - \beta)A_1 + \cos(\beta - \alpha_2)A_2 \tag{A.10}$$

The relative effective area for interface 1 is, for example,

$$\frac{Ae_1}{Ae_T} = \frac{\cos(\alpha_1 - \beta)A_1}{\cos(\alpha_1 - \beta)A_1 + \cos(\beta - \alpha_2)A_2} \tag{A.11}$$

Equation (A.5) and (A.11) reveal the identity that relates mass flux and effective area. The identity applies for each outflow interface:

$$\frac{m_i}{m_T} = \frac{Ae_i}{Ae_T} \tag{A.12}$$

Using the reported mass fluxes between grid blocks, the interface areas and the grid block coordinates, (A.12) can be used to determine $\beta$ and $Ae_T$, and therefore the true flux

vector. Note that the cosine terms in (A.4) and (A.11) vary depending on the relative positions of $\beta$ and $\alpha$.

Equation (A.12) applies to 2-D polygons with any number of sides, provided that the interfaces between grid blocks are orthogonal to the grid block connections, *i.e.*, Voronoi grid blocks. This includes the common rectilinear grid block. For a given simulation, the flow field may be such that the true flow direction on the inflow side is different than that at the outflow side. The projected area of the inflow and outflow sides will therefore be different. An average flow vector for the grid block could be defined as the average of the calculated vectors for the inflow and outflow sides.

### A.4 Example Application

An algorithm was written to calculate flux vectors for TOUGH2 simulation results using the relationship described above. Velocity vectors are equal to the calculated flux vector, $q$ [kg $m^{-2}$ $s^{-1}$], divided by a constant porosity and fluid density. The current version of the code uses only one flow side to calculate the velocity vector. Further code development will consider variations in porosity and fluid density, and enable calculation of an average grid block vector. Particle tracking is performed using TECPLOT®, which performs linear interpolation on the calculated vector field. Figure A.3 shows the streamlines for a steady-state horizontal flow in an irregular mesh. The mesh is discretized to model dipping strata offset by a vertical fault at x = 500 m and a dipping fault at x = 1250 m. The maximum relative error between the calculated and true velocity is 0.2%.

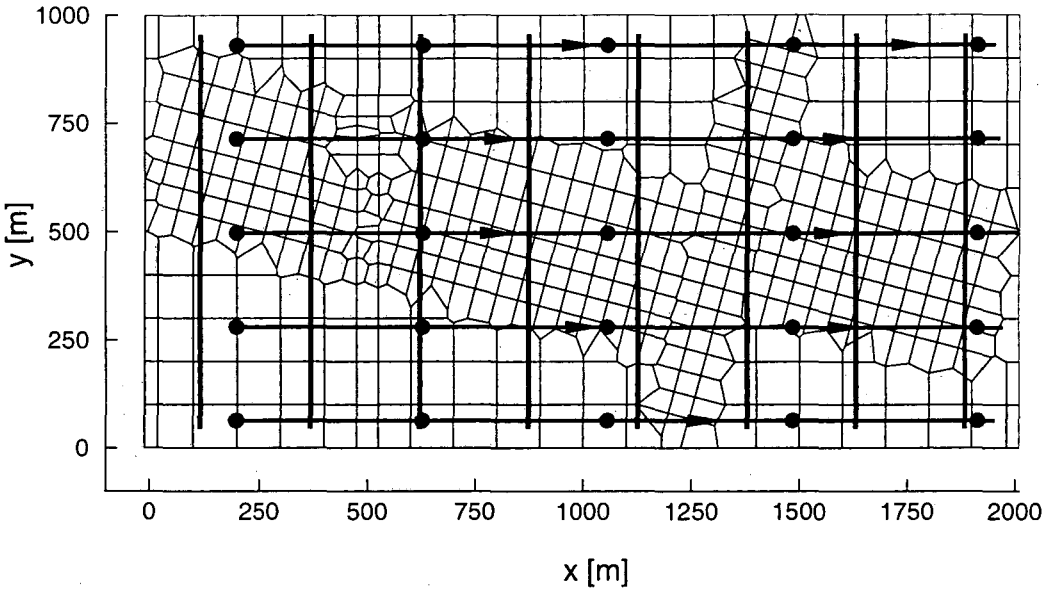


Figure A.3. Streamlines of steady-state flow in an irregular mesh. Vertical lines are pressure isolines and dots are constant time interval markers on the streamlines.

Ernest Orlando Lawrence Berkeley National Laboratory
One Cyclotron Road | Berkeley, California 94720

This work was supported in part by the Director, Office of Civilian Radioactive Waste Management, U.S. Department of Energy under Contract No. DE-AC03-76SF00098